

STIMULI-RESPONSIVE POLYMER ARCHITECTURES: FROM THIN FILMS TO
HYDROGELS

by

EVAN MICHAEL WHITE

(Under the Direction of Jason Locklin)

ABSTRACT

Light-responsive polymers systems, in both the dry state and hydrogel state were prepared to investigate nano-scale light-induced transitions. Pendant spirocyan (meth)acrylated block copolymers were fabricated via atom transfer radical polymerization (ATRP) and the nano-scale phase separation of thin films of spin coated films were investigated with tapping-mode atomic force microscopy (TM-AFM). Nano-scale phase separated films of spirocyan methacrylate copolymers were observed to exhibit changes in the phase separation profile when exposed to UV-light. The molecular weights, volume fraction, and phase separation were determined by NMR spectroscopy, GC and GPC, and AFM. Hansen solubility parameters were determined for mixed block copolymer poly(meth)acrylates by the group contribution method.

Hydrogel systems that responded to UV-light stimulus were also prepared as switchable adhesives. The polyacrylamide hydrogel contains a biomimetic 3,4-dihydroxyphenethylamide (DOPA) linkage group sensitive to pH. When the hydrogel is doped with a photoacid generator, diphenyliodonium chloride, and exposed to UV-light, the acidification induces an *in situ* titration of the DOPA groups, degrading the gel network. The mechanism of network degradation was investigated by UV-vis spectroscopy, rheometry, and lap-shear adhesion studies. Irradiation of

these hydrogels with UV light affords a viscous liquid solution, demonstrating a gel-sol transition with a subsequent decrease in the adhesive strength of the material. These gels may be prepared in high throughput and require few synthetic steps with commercially available precursors. These advantages of high throughput and biomimicry are important for preliminary investigations into biocompatibility of the gel, showing an antimicrobial zone of inhibition to *Staphylococcus aureus* when loaded with $5.1 \text{ mg}\cdot\text{mL}^{-1}$ neomycin sulfate.

INDEX WORDS: stimuli-responsive, block copolymer, spiropyran, hydrogel, biomimetic, catechol

STIMULI-RESPONSIVE POLYMER ARCHITECTURES: FROM THIN FILMS TO
HYDROGELS

by

EVAN M. WHITE

BS , Georgia College and State University, 2009

A Dissertation Submitted to the Graduate Faculty of The University of Georgia in Partial
Fulfillment of the Requirements for the Degree

DOCTOR OF PHILOSOPHY

ATHENS, GEORGIA

2014

© 2014

Evan M. White

All Rights Reserved

STIMULI-RESPONSIVE POLYMER ARCHITECTURES: FROM THIN FILMS TO
HYDROGELS

by

EVAN M. WHITE

Major Professor: Jason Locklin

Committee: Vladimir Popik
Richard Dluhy

Electronic Version Approved:

Julie Coffield
Interim Dean of the Graduate School
The University of Georgia
December 2014

DEDICATION

There are many aspects of my life that has contributed to making the works outlined in this document possible. Teachers, coaches, and role models and mentors too numerous to mention here all had little parts to play in molding my aptitude for learning and instilling a sense of wonder and curiosity in me. Family, of course, has always been supportive of the academic pursuit and the story of my journey thus far. For all those opportunities, I am grateful; specifically I owe thanks for all of the support from my parents and my newlywed wife, Lauren.

ACKNOWLEDGEMENTS

In a broader scope, I represent the quintessential Georgian academic student raised from lower grade school through undergraduate and graduate work through public school systems, and I would like to thank the University System of Georgia for years of public schooling I received at all levels. I would also like to acknowledge financial support from the National Science Foundation (CAREER Award, DMR 0953112).

TABLE OF CONTENTS

	Page
ACKNOWLEDGEMENTS	v
LIST OF TABLES	ix
LIST OF FIGURES	x
CHAPTER	
1 INTRODUCTION TO STIMULI-RESPONSIVE MATERIALS IN OUR WORLD	
TODAY AND LITERATURE REVIEW OF RECENT WORKS.....	1
Introduction.....	1
Spiropyran Copolymers	3
The Solubility Parameter, δ	5
Manipulating δ and χ_{12}	10
Block Copolymer Nano-Phase Separation.....	13
Atomic Force Microscopy of Thin Films	16
References.....	17
2 UV-SENSITIZED BLOCK COPOLYMER THIN FILMS	21
Abstract.....	22
Introduction.....	22
Results.....	25
TM-AFM of Spin Coated Block Copolymer Films.....	31
UV-vis Kinetic Study of Spiropyran-Merocyanine Isomerization	35

Conclusions.....	44
Experimental Details.....	45
References.....	55
3 ADVANCES IN SMART MATERIALS: STIMULI-RESPONSIVE HYDROGEL THIN FILMS	56
Abstract.....	57
Introduction.....	57
Theory of Swelling	58
Equilibrium Swelling Theory	59
Polymer Volume Fraction.....	60
Dynamic Swelling of Hydrogels.....	62
Calculation of the Mesh Size	63
Light Stimulus.....	66
Future Outlook for Hydrogels.....	69
References.....	70
4 SWITCHING THE ADHESIVE STATE OF POLYMERIC HYDROGELS USING PHOTOTITRATION.....	76
Abstract.....	77
Introduction.....	77
Experimental Details.....	80
Results.....	82
Preparation and Characterization of Hydrogels at 1.6% (w/v).....	83

Characterization of Iron (III) Complexation by UV-vis Spectroscopy	84
Mechanical Analysis of Hydrogels	88
Conclusions.....	90
References.....	91
5 HYDROGELS IN MEDICINE AND CONCLUDING REMARKS	95
Introduction and Problem	95
Design Constraints and Consideration.....	97
Dissolution Studies	99
Shelf Life	101
The pH Balance.....	103
Anti-microbial Studies	105
Stability Studies – pH and mechanical properties	106
Mesh Size Calculations for Particle Delivery.....	108
Next generation Shear Thinning Gels.....	108
Concluding Remarks on Stimuli-Responsive Polymer Architectures	110
References.....	112
 APPENDICES	
A NMR of Polymers 1 – 13.....	114
B Calculations for the Hansen solubility parameter by group contribution	121
C Supporting Information for pDMA Hydrogels	133

LIST OF TABLES

	Page
Table 2.1 SPA influence on polymerization conversion	27
Table 2.2 Calculations for χ_{12N} for SPA-containing polymers	30
Table 2.3 Calculations for χ_{12N} for mixed block copolymers	34
Table 2.4: Comparison of MC-SP ring-closure isomerization rates.....	37
Table 2.5 Physical parameters for the spiropyran block copolymers	39
Table B.1 The Hansen partial and total solubility parameters of p(nBA).	121
Table B.2 The Hansen partial and total solubility parameters of p(MMA).	121
Table B.3 The Hansen partial and total solubility parameters of p(SPA).	122
Table B.4 The Hansen partial and total solubility parameters of p(QA).	123
Table B.5 The Hansen partial and total solubility parameters of p(MCA).	124
Table B.6 The Hansen partial and total solubility parameters of p(SPMA).	124
Table B.7 The Hansen partial and total solubility parameters of p(QMA).	125
Table B.8 The Hansen partial and total solubility parameters of p(MCMA).	126
Table B.9 Solubility parameters of the mixed block of Polymer 11.	127
Table B.10 First-order group contributions for δ_D , δ_P , and δ_H	128
Table B.11 Second-order group contributions for δ_D , δ_P , and δ_H	130
Table B.12 First-order group contributions for δ_D , δ_P , and δ_H .- low δ_P	131
Table B.13 Second-order group contributions for δ_D , δ_P , and δ_H .- low δ_P	132

LIST OF FIGURES

	Page
Figure 1.1 Representation of diverse types of natural stimuli and responses	2
Figure 1.2 UV-induced p(SPA) isomerization.....	5
Figure 1.3 Comparison of entropy of mixing between small and large molecules	6
Figure 1.4 Micro-scale phase separation of pMMA and PP.....	7
Figure 1.5 The idealized nano-phase separation plot.....	12
Figure 1.6 Representation of UV-induced nano-phase separation domain reorganization	14
Figure 1.7 ATRP reaction equilibrium	17
Figure 1.8 Experimental set up for TM-AFM phase imaging	16
Figure 2.1 Depiction of the various tack and elastic properties of copolymers.....	23
Figure 2.2: Target values of $\chi_{12}N$ and Φ_A	24
Figure 2.3 GPC reaction kinetic profile of p(nBA-Br).....	26
Figure 2.4 Chain extension of pMMA-Br/Cl with p(nBA).....	28
Figure 2.5 Spin coated film on silicon of p(nBA-b-MMA-co-nBA), Polymer 7	31
Figure 2.6 TM-AFM annealing study, Polymer 8	32
Figure 2.7 TM-AFM images of A-B-A type block copolymers.....	34
Figure 2.8 Kinetic plots of SP to MC isomerization.....	36
Figure 2.9 Normalized isomerization reaction profiles	37
Figure 2.10 Experimental in situ UV AFM set-up.	38
Figure 2.11 TM-AFM height and phase images of photochromic block copolymer 11	40

Figure 2.12 TM-AFM height and phase images of photochromic block copolymer 10	41
Figure 2.13 In situ observation of discrete phase changes of Polymer 10.....	42
Figure 2.14 Nano-phase separation plot of block copolymers	43
Figure 2.15 Schematic synthesis of spiropyran(meth)acrylate chromophore monomer.	46
Figure 2.16 General approach for synthesis of block copolymers by ATRP	46
Figure 3.1 Schematic representation of a polymeric hydrogel	60
Figure 3.2 The first-order volumetric swelling response of hydrogels with respect to time	65
Figure 3.3 Spiropyran hydrogel micro-relief patterning.....	67
Figure 4.1 Switching the adhesive state of catecholic hydrogels using phototitration.....	77
Figure 4.2 Formation of switchable hydrogels and photodegradation	79
Figure 4.3 Photograph of bulk hydrogels prepared at 1.6 % (w/v) in water.....	83
Figure 4.4 UV-vis <i>in situ</i> titration and formation of bis-complexed pDMA	85
Figure 4.5 UV-vis <i>in situ</i> phototitration and dismantling of the bis-complex	87
Figure 4.6 Isothermal strain sweeps of 1.6 wt. % hydrogels	88
Figure 4.7 Lap shear adhesive strength testing of a 1.6 wt. % hydrogels.....	90
Figure 5.1 Schematic representation of the application and healing model	98
Figure 5.2 Dissolution study of air-stable 6 wt% pDMA	100
Figure 5.3 Schematic representation of ligand and metal exchange.....	102
Figure 5.4 Speciation plot of pDMA hydrogels from pH 5.2 to 11.5.....	103
Figure 5.5 Possible oxidation pathways for DOPA compounds.....	104
Figure 5.6 Incubation of a 6 wt% pDMA hydrogel with <i>S. aureus</i>	106
Figure 5.7 Storage modulus (G') and loss modulus (G'') varying iron content.....	107
Figure 5.8 TM-AFM topography images of micro- and nano-sized particles.....	109

Figure A.1 NMR of p(MMA ₇₇ -Br/Cl) macroinitiator, Polymer 1	114
Figure A.2 NMR of p(MMA ₇₇ -b-nBA ₁₄₂), Polymer 2.....	115
Figure A.3 NMR of p(MMA ₇₇ -b-nBA ₃₈ -co-SPA ₄) using dNbpy, Polymer 3	115
Figure A.4 NMR of p(MMA ₇₇ -b-nBA ₅₂ -co-SPA ₆) using PMDETA, Polymer 4.....	116
Figure A.5 NMR of p(Br-MMA ₇₅ -Br) macroinitiator, Polymer 5.....	116
Figure A.6 NMR of p(Br-nBA ₂₆₁ -Br) macroinitiator, Polymer 6.....	117
Figure A.7 NMR of p(nBA ₃₈₀ -b-MMA ₁₃₇ -co-nBA ₁₄), Polymer 7.....	117
Figure A.8 NMR of p(MMA ₅₀ -co-nBA ₄ -b-nBA ₃₁₀ -b- MMA ₅₀ -co-nBA ₄) , Polymer 8.....	118
Figure A.9 NMR of p(MMA ₂₂ -b-nBA ₂₆₁ -b-MMA ₂₂), Polymer 9	118
Figure A.10 NMR of p(MMA ₃₀ -co-SPMA ₁₅ -b-nBA ₂₆₁ -b-MMA ₃₀ -co-SPMA ₁₅).....	119
Figure A.11 NMR of p(nBA ₆₈ -co-SPA ₃ -b-MMA ₇₅ -b-nBA ₆₈ -co-SPA ₃), Polymer 11.....	119
Figure A.12 NMR of p(nBA-co-SPA), Polymer 12	120
Figure A.13 NMR of p(MMA-co-SPMA), Polymer 13	120
Figure B.1 Group assignments for p(nBA) and p(MMA).	121
Figure B.2 Group assignments for p(SPA) – low δ_h , p(MCA) – low δ_h , and p(QA) – low δ_h	122
Figure C.1 Catechol preservation in pDMA determined by ¹ H NMR.....	137
Figure C.2 Dynamic light scattering Debye plot for molecular weight determination	138
Figure C.3 UV-vis absorbance spectra for p(DMA-co-NIPAM-co-AcAm) in H ₂ O	138
Figure C.4 Extinction coefficients for diphenyliodonium chloride and the bis-complex.....	139
Figure C.5 NaHCO ₃ titration plot of p(DMA-co-NIPAM-co-AcAm)	139
Figure C.6 Lap-shear analysis before and after irradiation.....	140
Figure C.7 Kinetic plot of UV-induced conversion of diphenyliodonium chloride	140
Figure C.8 Varying the Fe ³⁺ concentration relative to catechol	141

Figure C.9 GATR-FTIR of dry native p(DMA-co-NIPAM-co-AcAm).....	141
Figure C.10 Control study on a $2 \text{ mg} \cdot \text{mL}^{-1}$ solution of p(DMA-co-NIPAM-co-AcAm).....	142
Figure C.11 Titrations for pDMA gels varying PAG content	142
Figure C.12 In situ UV-vis titration of pDMA gels varying PAG content.....	143
Figure C.13 Titration of p(DMA-co-NIPAM-co-AcAm) with excess base	144

CHAPTER 1
INTRODUCTION TO STIMULI-RESPONSIVE MATERIALS IN OUR WORLD TODAY
AND LITERATURE REVIEW OF RECENT WORKS

Introduction

Soft materials are ubiquitous in the thin biosphere of earth we call home. These materials, often called *plastics* in the vernacular, are traditionally described in the context of big commodity players like polystyrene, polyesters, polyethers, polyethylene, and polyacrylates to name a few. Clearly, synthetic polymers have enveloped and molded the modern world due to their utility, abundance, and diversity. Today, researchers aim to impart stimuli-responsive character into these materials in order to better understand the relationship between nano-scale and macro-scale properties, and to explore phenomena on very small scales. Remarkably, almost all of the world's organic polymers are found in life systems, and these materials are responsive to a variety of stimuli at the nano-scale.

Recent work from the Max Planck Institute shows how flowering plants like *Arabidopsis thaliana* among others produce and regulate SWEET9, a nectar-specific sugar transporter, to recruit selective reward pollinators according to environmental stimuli.¹ Similarly, the *Petunia* flower contains proteins capable of producing volatile compounds in complex floral blends that function as defense-response against insect florivores by secreting terpenes like linalool, which attracts predators to feed on the attacking insect.² Phytochrome proteins have been shown to alter plant color, shape, and growth via phototropism,³ where a chromophore bonded to proteins like Cph1 are capable of a light-induced isomerization of a tetrapyrrole, inducing macro-scale

movement of the organism.^{4, 5} Finds involved with plant movement by growth towards light suggesting protein macromolecules and chromophores have been center stage in stimuli-responsive polymers for some time in nature. Work from the De Moraes group showed how the dodder vine, *Cuscuta pentagona*, senses the surrounding environment by volatile chemical cues to guide the parasitic plant to proper host tomato plants by a locomotive response.⁶ Broadly reorganized by proteins, the polymers that constitute the structures of biology are perhaps the world's most specific smart materials. The polymeric architecture and order of these structures is paramount for their function to the environmental stimulus, be it photonic, chemical, electrical, thermal, or some other influence. Alas, biological locomotion is an orchestrated cooperation of a stupendous number of stimulus and response events of such polymers, and applying the principles biomimicry, a better understanding of the limits and opportunities of synthetic or semi-synthetic analogues may guide design challenges of future materials.

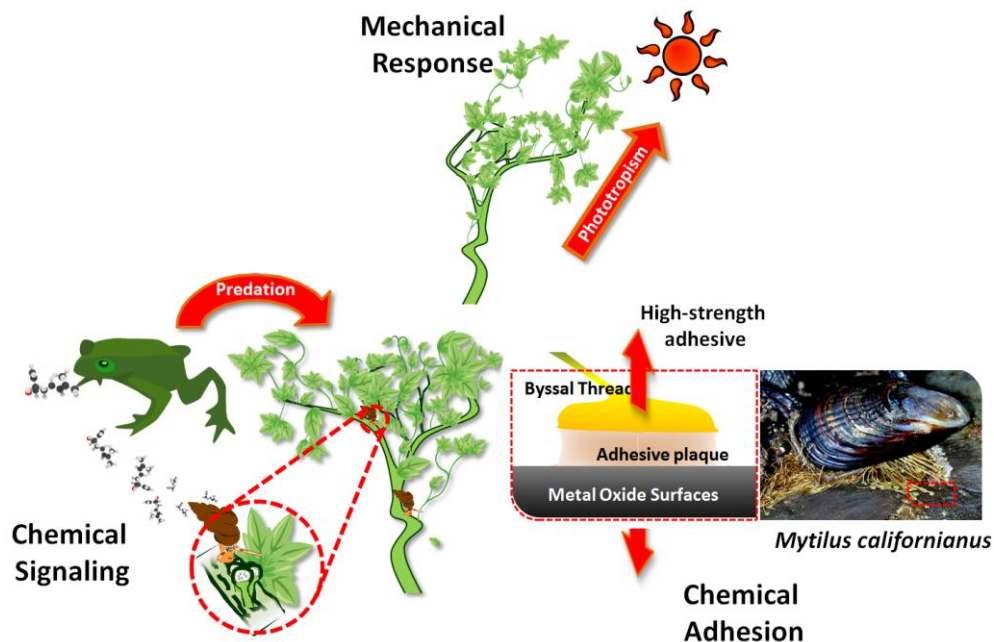


Figure 1.1. Representation of diverse types of natural stimuli and responses. Polymers are responsible for both mechanical responses and enzymatic chemical signaling.

Life has built an impressive library of dynamic materials, yet most commodity polymers are rather static in their nature, aside from examples like biodegradable poly(lactic acid) and other pH and enzyme responsive polymers, which are growing in niche markets.^{7, 8} Incorporating stimuli-responsive chemistry into synthetic polymers can provide insight into the potential and limitations of polymer architecture reorganization on the nano-scale. The purpose of the work outlined in this thesis is to incorporate light-responsive probes that may influence nano-scale architecture reorganization upon light exposure. I posit here a few inquiries about these materials. How do stimuli-responsive probes behave in media such as elastic polymers or viscous polymer solutions? Can light-triggered restructuring of the polymer at the molecular scale induce changes in the macroscopic properties such as modulus, surface energy, adhesion or tack? Could physical property changes like these influence nano-scale movement? Some conclusions to these queries are addressed herein, and two design types are considered, polymer thin films and hydrogels.

Spiropyran Copolymers

A diverse group of UV-active and reversible photochromic probes have been well characterized including azobenzenes, fulgides, diarylethenes, spirolactones, spirobenzopyrans, spiropyrans,⁹ o-naphthoquinone methides,¹⁰ cinnamates, coumarins, and photoacid generators to name a handful. Clearly a large variety of systems are available in the literature, and these systems may operate on UV-induced unimolecular ring scission and closure equilibria, bimolecular combinations reactions, and decomposition reactions.

Notably, photoswitchable spiro- and azo-derivatives have previously shown applications in surface patterning,¹¹ optical transduction,¹² surface wetting,¹³ chemical sensors,¹⁴⁻¹⁶ and

movement associated isomerization via mechanophores.¹⁷⁻¹⁹ In the context of thin films, previous work on the spiropyrans is among the most informative and well-studied experimentally and computationally.²⁰⁻²³ Work by Bell and coworkers demonstrated UV-induced nano-particle aggregation and precipitation from a stable colloid based on the spiropyran isomerization.²⁴ Later work by the Locklin group demonstrated how polymer thin films containing spiropyrans are capable of large changes in wettability when irradiated with UV light.^{25, 26} The large dipole moment shift from 10 to 23.8 Debye in H₂O is responsible for the dramatic changes in solubility and surface free energy.²⁷ Could these probes also induce changes in the nano-structure of thin films in the dry state? To address this, copolymers containing UV-switchable probes, spiropyrans, were constructed as block copolymer thin films. The use of photoacid generators in hydrogels will be addressed later in Chapter 4.

Like other photosensitive isomerizations, spiropyran chromophores exist in equilibrium between a thermally stable ring-closed and UV-induced ring-open form. Fulgides, diarylethenes, and spiropyrans alike absorb in the range of 300 – 400 nm, and the chromophore undergoes a ring cleavage upon irradiation.²¹ This cleavage generates ring-open isomers with absorption maxima in the visible spectrum, which may be reverted to the ring closed form by exposure to visible light or heat. However, spiropyrans (SP) differ from fulgides and diarylethene in that their ring-open merocyanine (MC) isomer is resonance stabilized between a neutrally charged quinodal form and a highly polarized zwitterionic form (Figure 1.2).

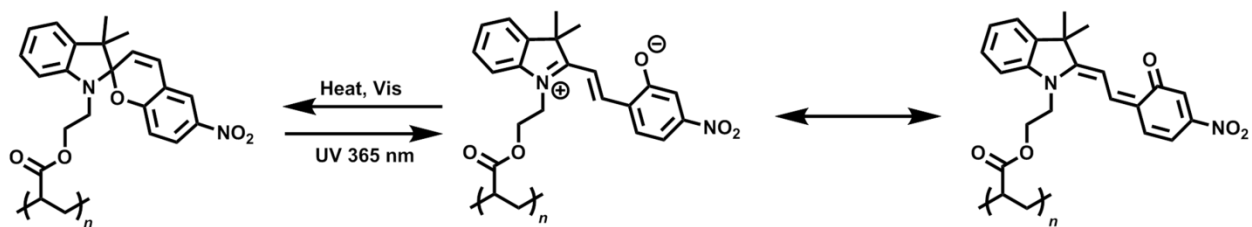


Figure 1.2. UV-induced p(SPA) isomerization. The zwitterionic merocyanine p(MCA) and neutral quinone p(QA) equilibrium is shown between B and C.

The MC-zwitterion has a high dipole moment in comparison to the ring closed SP form.²⁷ This change in polarity and the collective intermolecular forces between the isomers influences the solubility parameter, δ , a characteristic descriptor of small molecules and polymers alike. In short, the solubility parameter describes the compatibility of solvents by considering the cohesive forces that bind the liquid state. This principle can be applied to polymers by considering the repeat unit, and the values of δ for solvent and polymer influences solutions of polymers^{24, 28} and solvent swollen thin films.¹⁴ Can changes in δ drive molecular mobility of semi-solid polymers? Hereafter is a brief review on the theory of polymer mixing from the early work of Flory to Hildebrand and Hansen and later additions to the solubility parameter models.

The Solubility Parameter, δ

The solubility of polymers is chiefly dictated by the repeat unit chemistry, size, and connectivity of the polymer. Much work by Flory and Huggins determined that dissolution of polymers in ideal solvents is largely dictated by the entropy of mixing, which is given by the number of possible configurations of a solvated polymer.^{29, 30} For favorable mixing, the basic principle of “like dissolves like” is often observed. As molecular weight of polymers increase, entropy of mixing in an ideal solvent is reduced because the polymer chain has fewer degrees of

freedom due to the connectivity of the backbone. Similarly, when dissimilar polymers are dissolved into one another in the absence of solvent, mixing is often highly unfavorable, as depicted in Figure 1.3.

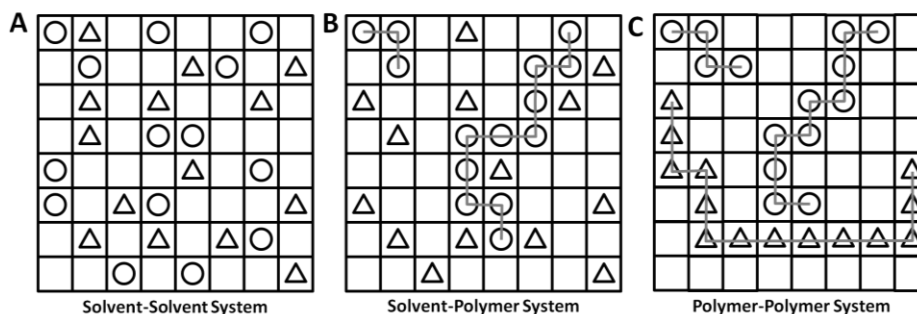


Figure 1.3. Comparison of entropy of mixing between small and large molecules. A. System of two miscible solvents. B. A polymer-solvent system. C. A polymer-polymer system. The entropy of mixing is reduced because the units of the chains are restricted to the architectures defined by covalent bonds of monomers.²⁸

In polymer-polymer mixing, the statistically possible number of arrangements is considerably smaller than it is for a polymer-solvent system. Additionally, the molar volume also plays an important role in mixing of macromolecules. Through statistical mechanics, Flory and Huggins have shown that the entropy gain in large molecule mixing, ΔS^M , is relatively small when compared to liquids.²⁹ This entropic barrier to mixing is responsible for the challenges associated with the solubility of a number of macromolecules, especially biological polymers like polysaccharides and their derivatives. A similar trend of immiscibility is observed when two only slightly dissimilar polymers are mixed from the melt or from solution.

For instance, a blend of polyethylene poly(methyl methacrylate) (pMMA) and polypropylene (PP), will phase segregate on the micro-scale over a large enough time scales and has been well studied since the 1980s.³¹ The micro phase separation is still a subject of study

today as shown by TEM imaging of a spin coated film of pMMA and PP polymer blend from solution.³²

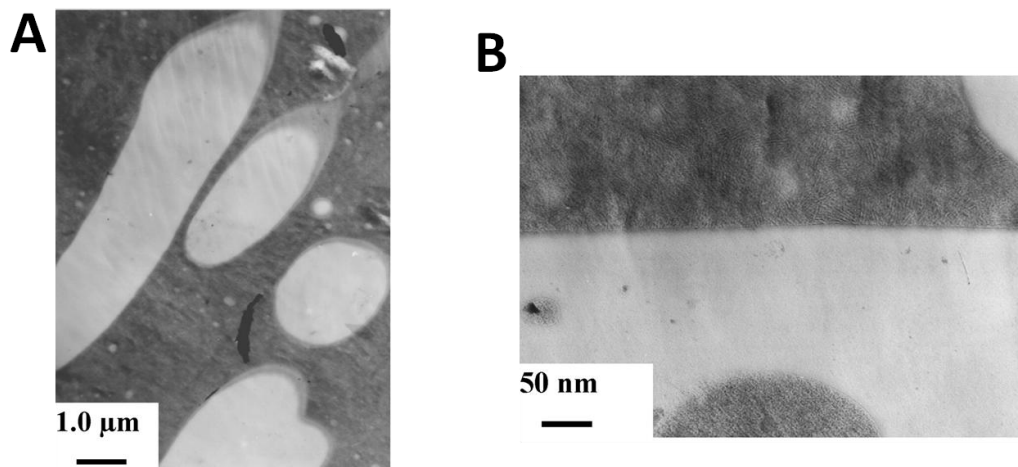


Figure 1.4. Micro-scale phase separation of pMMA and PP. Imaged by TEM, the dark portions are the PP domains while the lighter sections represent pMMA.³² Reprinted with permission from *Macromolecules* **2011**, 44, 6103-6112. Copyright 2011 American Chemical Society.

The spontaneous phase separation may be explained by the thermodynamics for mixing, which requires that the free energy of mixing must be zero or negative for solution formation to occur spontaneously given by the relationship:

$$\Delta G^M = \Delta H^M - T\Delta S^M \quad (\text{Equation 1.1})$$

where ΔG^M is the free energy of mixing, ΔH^M is the measurable enthalpy of mixing, ΔS^M is entropy change of the mixing process, and T is the temperature. It can be seen from this equation that entropy change is beneficial to mixing, and an increase in temperature promotes mixing as ΔG^M becomes more negative. However, examples of insolubility of polymers above some lower critical solution temperature (LCST) are common in the literature where an increase in temperature promotes insolubility. For instance, pNIPAM exhibits an LCST around 32 °C in

water. To account for both positive and negative heats of mixing, Patterson and Delmas modified ΔG^M to the noncombinatorial free energy of solution, $\Delta G^M_{\text{noncomb}}$, which includes all free energy effects other than the combinatorial entropy of solution, ΔS^M_{comb} , due to simply mixing polymer in solution.²⁸ The maximum difference in solubility parameters between polymer and solvent to allow a solution is found by setting these terms equal to one another as in Equation 1.2. The solubility parameter for the solvent and polymer, δ_1 and δ_2 respectively, play an important role in determining the noncombinatorial free energy of solution by the relationship

$$T\Delta S^M_{\text{comb}} = \Delta G^M_{\text{noncomb}} = \varphi_1\varphi_2V_M(\delta_1 - \delta_2)^2 \quad (\text{Equation 1.2})$$

In this case, the values of φ represent the volume fractions of solvent and polymer and V_M corresponds to the total volume of the mixture. The solubility of a polymer in a given solvent typically increases as the value of δ_1 approaches that of δ_2 . Notably, polymer solubility parameters do not change much with temperature, but those of a liquid often decrease with temperature.²⁸ And of particular importance, the entropy changes associated with polymer solutions will be smaller than those of liquid-liquid miscibility.

To address such solvent-polymer and polymer-polymer interactions, Hildebrand and Scott first described a quantitative term to predict mixing of polymer blends and solutions with the total Hansen solubility parameter, δ_t .^{33, 34} This parameter is defined as the square root of the cohesive energy density, in other words, the sum of all molecular interactions responsible for evaporating from liquid to gas:

$$\delta_t = \left(\frac{E}{V_{\text{mol}}} \right)^{1/2} \quad (\text{Equation 1.3})$$

Here, V_{mol} is the molar volume of a pure liquid and E is the energy of vaporization. The cohesive energy is given by:

$$E = \Delta H_v - RT \quad (\text{Equation 1.4})$$

where ΔH_v is the standard enthalpy of vaporization at 298K, R is the universal gas constant, and T is the absolute temperature.

The total solubility parameter describes well the mixing of rather nonpolar compounds, but is not sufficient in describing solubility behaviors of polar compounds. This occurs due to three distinguishable kinds of intermolecular forces that influence E : dispersion, polar, and hydrogen-bonding forces. The dispersion forces are universal to all molecules and are responsible for the colligative properties of species like short-chain alkanes. Asymmetry in the molecule gives rise to dipole moments which interact with polar forces of varying strength, and hydrogen-bonding forces arise from classic examples of proton donor-acceptor groups present in the molecule.³⁵

Later work by Hansen improved on the predictive capacity of solubility parameters by the introduction of partial solubility parameters, δ_d , δ_p , and δ_h .³⁶

$$\delta_t = (\delta_d^2 + \delta_p^2 + \delta_h^2)^{1/2} \quad (\text{Equation 1.5})$$

Where δ_d is the dispersion Hansen solubility parameter, δ_p is the polar Hansen solubility parameter, and δ_h is the hydrogen-bonding Hansen solubility parameter. Notably, the unit of the Hansen solubility parameter, expressed as $\text{MPa}^{1/2}$ is 2.0455 times larger than that of the Hildebrand solubility parameter, expressed in cal/cm^3 . The Hildebrand and Hansen solubility parameters describe the same phenomenon of mixing of two species, but direct comparison of the terms presents discrepancies and gives more qualitative relationships.

The Hansen solubility parameter may be estimated by the group-contribution method. A number of methods have been used to calculate group contribution effects including Hoy,³⁷ Hoftyzer and van Krevelen,³⁸ and later work by Stefanis and Panayiotou.³⁵ The later work by

Stefanis and Panayiotou is the most informative in describing the functional groups of relatively complex molecules like spiropyran and will be described later in Chapter 2. It is important to note that the work presented in this thesis is not a comprehensive review of the calculations to describe δ_d , δ_p , and δ_h . The computational treatment of these parameters can be found in the literature.³⁸ In practical use, the partial solubility parameters of a polymer may be considered as the sum of the group contributions by Equations 1.6 – 1.8.

$$\delta_D = \left(\sum_i N_i C_i + \sum_j M_j D_j + 17.3231 \right) \quad \text{(Equation 1.6)}$$

$$\delta_P = \left(\sum_i N_i C_i + \sum_j M_j D_j + 7.3548 \right) \quad \text{(Equation 1.7)}$$

$$\delta_H = \left(\sum_i N_i C_i + \sum_j M_j D_j + 7.9793 \right) \quad \text{(Equation 1.8)}$$

C_i is the contribution of the first-order group of type i that appears N_i times in the compound, and D_j is the contribution of the second-order group of type j that appears M_j times in the compound. The constants of 17.3231, 7.3548 and 7.9793 are in $\text{MPa}^{1/2}$ and were determined by Stefanis and Panayiotou.³⁵ The solubility parameters help describe the nano-scale phase separation of copolymers and are required to predict the dimensionless Flory interactions parameter for polymer-polymer mixing, χ_{12} .

Manipulating δ and χ_{12}

An approximation of the solubility parameter, δ , and the dimensionless Flory interaction parameter, χ_{12} , can help us gain insight about polymer solvency and predict changes that may occur in these systems when mixed. On these two fundamental principles, work from Bell and

coworkers manipulated a colloidal system's solubility remotely by photochemical changes in spiropyran-containing poly(methyl methacrylate), p(MMA), brushes grown from silica particles.²⁴ The Locklin group demonstrated changes in the surface free energy via contact angle spiropyran-containing p(MMA) spin coated films and polymer brushes.^{14, 25} Later work by Szilágyi and coworkers demonstrated how spiropyran-containing hydrogels may be manipulated for lithographic relief formation in dilute polymer solutions.¹⁹ However, no group had investigated nano- or micro-scale mobility in semi-solid polymeric media, such as dry-state thin films. The work of the spiropyran copolymers presented hereafter manipulates δ and χ_{12} with spiropyran probes to influence phase changes in thin films of nano-phase separated mixed block copolymers under similar principles of light-induced changes in solubility. There is, however, an entropic penalty for polymer-polymer mixing, given that the degree of polymerization, N , is sufficiently large. When molecular weight grows, a boundary condition exists where mixed polymers spontaneously phase separate into immiscible ordered domains (Figure 1.5).

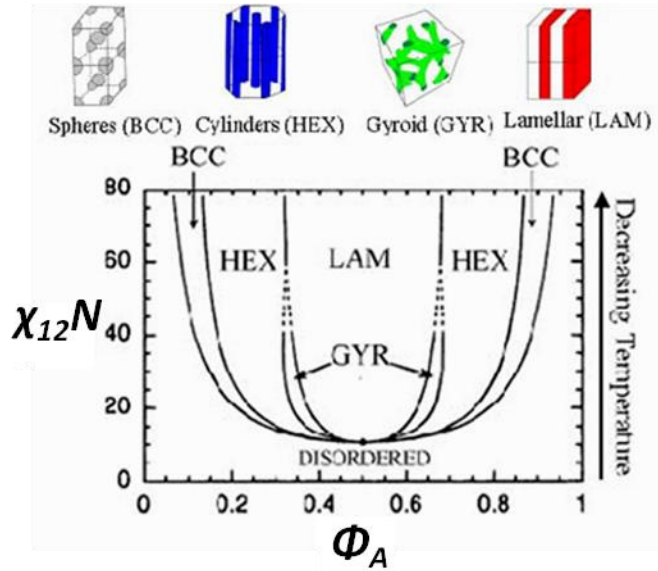


Figure 1.5. The idealized nano-phase separation plot. Governed by χ_{12} and Φ_A , four distinct orders of architectures exist above sufficient values of $\chi_{12}N$, and when $\sim 0.05 < \Phi_A < \sim 0.95$. Very low molecular weight polymers and oligomers are often miscible and fall in the disordered domain when mixed. Reprinted with permission from *Chemical Communications* **2005**, 4143-4148. 2014 Copyright Clearance Center, Inc.

The geometric order of these domains also depends on the polymer volume fraction, Φ_A , and the Flory interaction parameter, χ_{12} , between each polymer. This term can be approximated from the HSP of each domain, and helps govern the conditions of nano-phase separation according to the relationship

$$\chi_{1,2} = \frac{V_{mol}[(\delta_{D1} - \delta_{D2})^2 + 0.25(\delta_{P1} - \delta_{P2})^2 + 0.25(\delta_{H2} - \delta_{H1})^2]}{RT}$$

(Equation 1.9)

Where V_{mol} represents the weighted molar volume of the repeat unit, and δ_{D1} , δ_{P1} , δ_{H1} , δ_{D2} , δ_{P2} , and δ_{H2} represent the dispersive, polar, and hydrogen-bonding Hansen partial solubility

parameters for the major and minor phases, respectively. The term T represents the temperature in Kelvin and R is the universal gas constant in $\text{cm}^3 \cdot \text{MPa} \cdot \text{K}^{-1} \cdot \text{mol}^{-1}$.

$$\frac{V_A}{V_A + V_B} = \Phi_A = \left(\frac{\rho_A n_B MW_B}{\rho_B n_A MW_A} + 1 \right)^{-1} \quad (\text{Equation 1.10})$$

The volume fractions of the major and minor block, V_A and V_B , are determined by the molecular weight of each block, MW_A and MW_B , the density, ρ_A and ρ_B , and the molar ratio of monomers in the blocks, n_A and n_B , of each polymer. Volume fraction calculations are described in more detail in Chapter 2.

Block Copolymer Nano-Phase Separation

Spherical, cylindrical and lamellae domains among others may form depending on the volume fraction, Φ_A , degree of polymerization, N , and the Flory interaction parameter between the two blocks, χ_{12} , as shown in Figure 1.5. The volume fraction domain boundaries of particular interest are between the disordered domain and spherical domain, and the boundary between spherical and hexagonal domain. By approximation of the HSP for two dissimilar blocks of a block copolymer, polymers of target domain phase separation may be built by manipulation of Equations 1.9 and 1.10.

Manipulation of the Flory interaction parameter with UV-active probes, and therefore the polymer-polymer solubility of each block, may give rise to changes in nano-scale morphology. If the solubility parameters of the first block, δ_{D1} , δ_{P1} , and δ_{H1} , are kept constant and values of δ for the second block, δ_{D2} , δ_{P2} , and δ_{H2} , are varied *in situ*, can changes in χ_{12} of this system reorganize to some other nano-phase separation domain? I hypothesized that by using the spirocyan-merocyanine probe as discussed earlier, changes in δ could influence transitions about these domain barriers using UV light as the stimulus. If the magnitude of the interaction

parameter change is large and the volume fraction of the block copolymers is tuned about the boundary of these domains, such changes may arise as depicted in Figure 1.6.

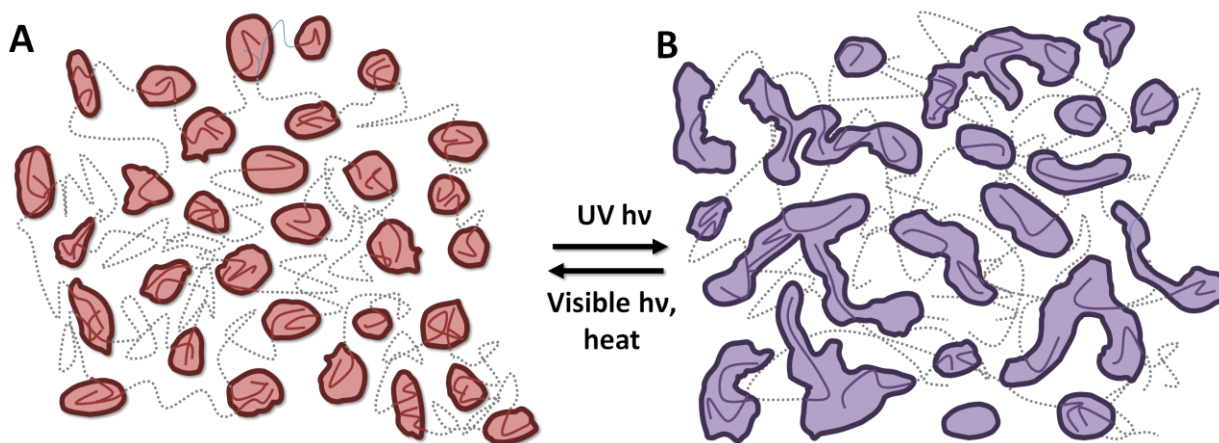


Figure 1.6. Representation of UV-induced nano-phase separation domain reorganization. Depicted here is a near-spherical domain minor phase in red, **A**, and subsequent treatment with UV-light to a near cylinder domain shown in purple, **B**. The dashed gray lines represent the low T_g , major domain.

The approach, synthesis and characterization of these UV-active block copolymers are outlined in Chapter 2. In order to build polymeric architectures of appropriate volume fraction and polymer-polymer solubility, a few criterion must be satisfied:

1. Polymers must be linear in type in order to use Equations 1.9 and 1.10 for estimating nano-phase separation
2. Polymers should be low in molecular weight and dispersity to maximize ΔS_{comb} , yet sufficiently high in molecular weight to allow domain formation.
3. At least one block of the polymer must be below the glass transition temperature, T_g

Certainly the molecular weight is an important parameter to address. A number of examples of polymerization techniques exist in the literature for making polymers of controlled, low

molecular weight, each with their benefits and pitfalls. Ring opening metathesis polymerization (ROMP) and reversible addition-fragmentation chain transfer (RAFT) allows control of predictably small molecular weight but with limitations in backbone flexibility and initiator choice, respectively. Anionic and cationic polymerization can also afford narrow molecular weight distributions, but offers limited functional group tolerance. As shown in previous work by Fries²⁶ and Lee,³⁹ spiropyran pendant molecules may be attached to acrylic backbones using atom transfer radical polymerization (ATRP). The advantage of ATRP comes with functional group tolerance, controlled polymerization rates, and thoroughly studied acrylic, styrenic, and vinylic monomer choices.

ATRP operates on a one-electron redox equilibrium between an oxidized and reduced form of a ligated transition metal, Mt^D/L , as shown in Figure 1.7.

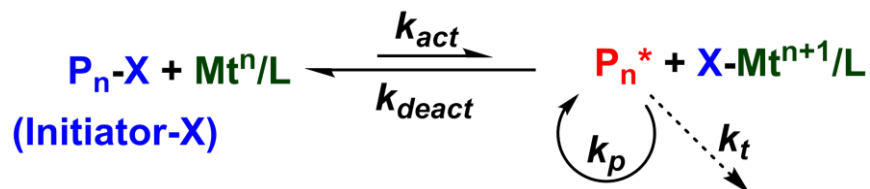


Figure 1.7. ATRP reaction equilibrium. The activation rate, k_{act} , and deactivation rate, k_{deact} , determine the overall rate of the reaction K_{ATRP} . Monomer may add at the rate, k_p , or the growing polymer chain, P_n^* may terminate at some rate, k_t .⁴⁰

Briefly, the initiator and polymer, P_n , are alkyl halides which may undergo homolytic cleavage of the carbon halide bond to form P_n^* and the oxidized metal complex $X-Mt^{n+1}/L$. This equilibrium process lies heavily to the left as $k_{deact} \gg k_{act}$ in controlled polymerizations, and the equilibrium rate can be manipulated by ligand choice, L . Once P_n^* is formed, the newly formed metal-halide can be reduced back to the Mt^n/L complex by reforming the carbon halide bond.

Monomer can add to form polymer at rate k_p , or termination events nascent to radical polymerizations may terminate growing chains at rate k_t .

As with other techniques, there are a couple pitfalls of ATRP with spiropyrans. Chiefly, this chromophore has been shown to chelate strongly to transition metals,²⁶ especially cuprous ions, which is the most common redox catalyst for ATRP via the Cu^{1+} to Cu^{2+} redox reaction. Some kinetic studies on spiropyran catalyst competition will be described in Chapter 2.

Atomic Force Microscopy of Thin Films

When building block copolymers for the purpose of investigating this nano-phase architecture, TM-AFM phase imaging offers a robust method for characterizing topological phenomenon on these scales. The principle of the technique and setup are outlined in Figure 1.8.

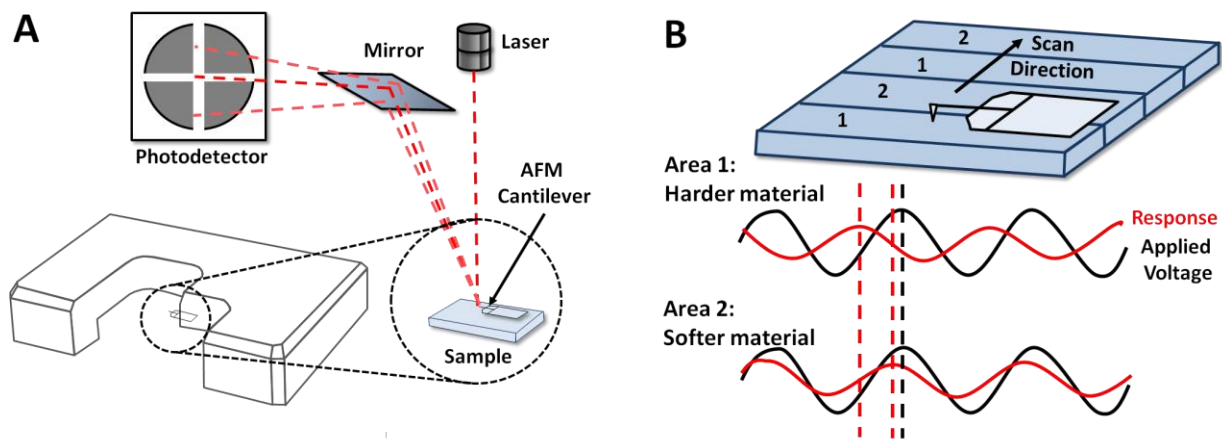


Figure 1.8. Experimental set up for TM-AFM phase imaging. **A**, and depiction of phase imaging of a heterogeneous surface, **B**. The change in the phase response in the tapping cantilever generates then phase image in TM-AFM.

As the stylus of a record player scans concentrically a record's micro-scale morphology, the tip of an AFM probe in tapping mode sinusoidally oscillates while tapping the nano-scale

surface features with low force. The AFM tip raster scans about the fast axis, the x-axis, and shifts along the slow axis, y-axis, for the next line of imaging. This produces voltage-response differences detected by the 4-quadrant photodiode mounted in the AFM head. The distance between the substrate and AFM tip are precisely modulated by the z-axis piezoelectric positioning which corresponds to z-data. Moreover, when the sinusoidal oscillation is disturbed by tip contact with the surface, a phase change is observed that is proportional to the substrates resistance to deformation, or modulus. Phase channel imaging in tapping mode AFM (TM-AFM) is often most informative of nano-scale architectures of these small polymers.

This thesis is notably broken into two major classes of polymeric architecture, as stimuli-responsive synthetic materials. Much of the inspiration for the design and synthetic approach comes from previous work and examples of stimuli-responsive polymers found in biology. It is important to realize that the calculations for solubility parameters are used as guides to the experimental design, and predictions of polymer-polymer volume fractions and approximations of the Flory interaction parameters between solvents and polymers. These fundamental principles of solubility also play an important role in hydrogels, which will be discussed in Chapters 3 and 4. The physics of hydrogel swelling and solubility and work in the field will be introduced in Chapter 3.

References

1. Lin, I. W.; Sosso, D.; Chen, L.-Q.; Gase, K.; Kim, S.-G.; Kessler, D.; Klinkenberg, P. M.; Gorder, M. K.; Hou, B.-H.; Qu, X.-Q.; Carter, C. J.; Baldwin, I. T.; Frommer, W. B. *Nature* **2014**, 508, 546-549.
2. Kessler, D.; Diezel, C.; Clark, D. G.; Colquhoun, T. A.; Baldwin, I. T. *Ecology Letters* **2013**, 16, 299-306.

3. Rockwell, N. C.; Su, Y.-S.; Lagarias, J. C. *Annual Review of Plant Biology* **2006**, *57*, 837-858.
4. Song, C.; Psakis, G.; Lang, C.; Mailliet, J.; Zaanen, J.; Gärtner, W.; Hughes, J.; Matysik, J. *Biochemistry* **2011**, *50*, 10987-10989.
5. Britz, S. J.; Galston, A. W. *Plant Physiology* **1983**, *71*, 313-318.
6. Runyon, J. B.; Mescher, M. C.; De Moraes, C. M. *Science* **2006**, *313*, 1964-1967.
7. Mäki-Arvela, P.; Simakova, I. L.; Salmi, T.; Murzin, D. Y. *Chem. Rev.* **2013**, *114*, 1909-1971.
8. Jamshidian, M.; Tehrany, E. A.; Imran, M.; Jacquot, M.; Desobry, S. *Comprehensive Reviews in Food Science and Food Safety* **2010**, *9*, 552-571.
9. Phillips, J. P.; Mueller, A.; Przystal, F. *J. Am. Chem. Soc.* **1965**, *87*, 4020-4020.
10. Arumugam, S.; Popik, V. V. *J. Am. Chem. Soc.* **2009**, *131*, 11892-11899.
11. Willner, I.; Blonder, R. *Thin Solid Films* **1995**, *266*, 254-257.
12. Willner, I. *Accounts of Chemical Research* **1997**, *30*, 347-356.
13. Samanta, S.; Locklin, J. *Langmuir* **2008**, *24*, 9558-9565.
14. Fries, K. H.; Driskell, J. D.; Sheppard, G. R.; Locklin, J. *Langmuir* **2011**, *27*, 12253-12260.
15. Shiraishi, Y.; Sumiya, S.; Manabe, K.; Hirai, T. *ACS Appl. Mater. Interfaces* **2011**, *3*, 4649-4656.
16. Mistlberger, G.; Crespo, G. A.; Xie, X.; Bakker, E. *Chemical Communications* **2012**, *48*, 5662-5664.
17. Lee, C. K.; Diesendruck, C. E.; Lu, E.; Pickett, A. N.; May, P. A.; Moore, J. S.; Braun, P. V. *Macromolecules* **2014**, *47*, 2690-2694.

18. Zhang, H.; Chen, Y.; Lin, Y.; Fang, X.; Xu, Y.; Ruan, Y.; Weng, W. *Macromolecules* **2014**, *47*, 6783-6790.
19. Szilágyi, A.; Sumaru, K.; Sugiura, S.; Takagi, T.; Shinbo, T.; Zrínyi, M.; Kanamori, T. *Chem. Mater.* **2007**, *19*, 2730-2732.
20. Dvornikov, A. S.; Malkin, J.; Rentzepis, P. M. *The Journal of Physical Chemistry* **1994**, *98*, 6746-6752.
21. Hirshberg, Y. *J. Am. Chem. Soc.* **1956**, *78*, 2304-2312.
22. Sheng, Y.; Leszczynski, J.; Garcia, A. A.; Rosario, R.; Gust, D.; Springer, J. *J. Phys. Chem. B* **2004**, *108*, 16233-16243.
23. Rosario, R.; Gust, D.; Hayes, M.; Springer, J.; Garcia, A. A. *Langmuir* **2003**, *19*, 8801-8806.
24. Bell, N. S.; Piech, M. *Langmuir* **2006**, *22*, 1420-1427.
25. Fries, K.; Samanta, S.; Orski, S.; Locklin, J. *Chemical Communications* **2008**, 6288-6290.
26. Fries, K. H.; Driskell, J. D.; Samanta, S.; Locklin, J. *Anal. Chem.* **2010**, *82*, 3306-3314.
27. Murugan, N. A.; Chakrabarti, S.; Ågren, H. *J. Phys. Chem. B* **2011**, *115*, 4025-4032.
28. Hansen, C., M., *Hansen Solubility Parameters: A User's Handbook*. CRC Press LLC: Boca Raton, London, New York, Washington D.C., 2000.
29. Flory, P. J. *J. Chem. Phys.* **1942**, *10*, 51-61.
30. Huggins, M. L. *The Journal of Physical Chemistry* **1942**, *46*, 151-158.
31. Wenig, W.; Schöller, T., Phase separation in incompatible polymer blends: polypropylene-polyethylene system. In *Frontiers in Polymer Science*, Wilke, W., Ed. Steinkopff: 1985; Vol. 71, pp 113-118.

32. Zhu, R.; Hoshi, T.; Chishima, Y.; Muroga, Y.; Hagiwara, T.; Yano, S.; Sawaguchi, T. *Macromolecules* **2011**, *44*, 6103-6112.
33. Hildebrand, J. S., R. L., *The Solubility of Nonelectrolytes, 3rd Ed.* Reinhold, New York, 1950.
34. Hildebrand, J. S., R. L., *Regular Solutions*,. Prentice-Hall Inc.: Englewood Cliffs, NJ, 1962.
35. Stefanis, E.; Panayiotou, C. *International Journal of Thermophysics* **2008**, *29*, 568-585.
36. Hansen, C. M. S., Klemen. *Journal of Paint Technology* **1967**, *39*, 511-514.
37. Hoy, K. L. *J. Paint Technol.* **1970**, *42*, 76-118.
38. Krevelen, P. J. H. D. W. v., *Properties of Polymers*. 2nd ed.; Elsevier: Amsterdam, 1976.
39. Lee, H.-i.; Wu, W.; Oh, J. K.; Mueller, L.; Sherwood, G.; Peteanu, L.; Kowalewski, T.; Matyjaszewski, K. *Angewandte Chemie International Edition* **2007**, *46*, 2453-2457.
40. Matyjaszewski, K. *Macromolecules* **2012**, *45*, 4015-4039.

CHAPTER 2
UV-SENSITIZED BLOCK COPOLYMER THIN FILMS

E. M. White, G. Sheppard, J. B. Grubs, J. Locklin. *To be submitted*

Abstract

A series of photochromic block copolymers of containing spiropyran as a UV probe whereby A-B type and A-B-A type block copolymers were fabricated by sequential monomer addition and from macroinitiators to compare nano-phase separation profiles by tapping mode atomic force microscopy (TM-AFM). The observed MC-SP ring-closing isomerization demonstrated near first-order rates in tri-block copolymers fabricated from acrylic and methacrylic comonomers. A polymer fabricated with a high mole percent of spiropyran monomer in the methacrylate block demonstrated reproducible UV-induced phase transitions observed by TM-AFM. The polymer data was treated with Hansen solubility parameter calculations using the group contribution method to determine the solubility parameter of the UV-active block, δ_t , and the Flory interaction parameter, χ_{12} , for nano-phase separation domain predictions.

Introduction

Poly acrylates and methacrylates are used in a broad spectrum of applications, and span a large number of industries. Tunable material properties, vast monomer selection, low cost, ease of synthesis through radical polymerization, and a history of considerable effort to characterize these materials makes them a desirable polymer choice for experimentation. Material science has developed many methods to quantify intrinsic properties of polymers like the poly(meth)acrylates. Built from the work of Hildebrand and Scott, Hansen, and Stefanis and Panayiotou, this chapter uses some of the earlier discussed principles of heterogeneous mixing to build UV-active copolymers.

Polymer phase separation is a phenomenon that has been studied heavily since the 1980s.^{1,2} The intent of the work presented in this chapter is to investigate chain mobility of such phase separated, dry-state polymer films by tapping mode atomic force microscopy (TM-AFM) using the UV-induced spiropyran-merocyanine (SP-MC) isomerization as a stimuli-responsive probe. As discussed in Chapter 1, the nano-phase separation of block copolymers is governed by the polymer-polymer compatibility described by χ_{12} , molecular weight, and the volume fraction of each polymer block. Since the domain segregation of block copolymers is influenced by the partial Hansen solubility parameters, δ_D , δ_P , and δ_H , the nano-phase separation domain could, in theory, shift to another ordered domain with changes in χ_{12} . Such transitions of δ may influence the nano-scale architecture and could perhaps induce larger macroscopic property changes. Some examples of block copolymers are outlined in Figure 2.1 to illustrate the diverse properties of poly(meth)acrylates.



Figure 2.1. Depiction of the various tack and elastic properties of copolymers. Poly(meth)acrylates are used as adhesives used to back high-temperature tapes, acrylic shoe soles, and low weight windows such as the glassy homopolymer p(MMA).

A spectrum of material properties for poly(meth)acrylates exists, from the adhesives found on tapes, to acrylic shoe soles, and glassy pMMA. The synthesis and thin film

characterization of some UV-sensitive spiropyran (meth)acrylate mixed block copolymers are described. UV-treatment of these films show variations in the polymer-air interface, as suggested by TM-AFM imaging, and a theoretical calculation of the nano-phase separated domain for UV-sensitive polymers is discussed. The synthetic approach to investigate UV-induced changes in block copolymer nanophase separation followed a few criteria:

1. One phase of the block copolymer must have a low glass transition temperature, T_g
2. The spiropyran chromophore must be contained in only one block
3. Sufficiently high molecular weight is required to resist homogeneous mixing, yet sufficiently low molecular weight and polydispersity are required to promote domain mobility

The ideal target molecular weights and domain boundaries can be illustrated by revisiting the idealized phase separation diagram in Figure 2.2. It is important to note that the nano-phase separation observed in the (meth)acrylic block copolymers deviates slightly from the generalized case.

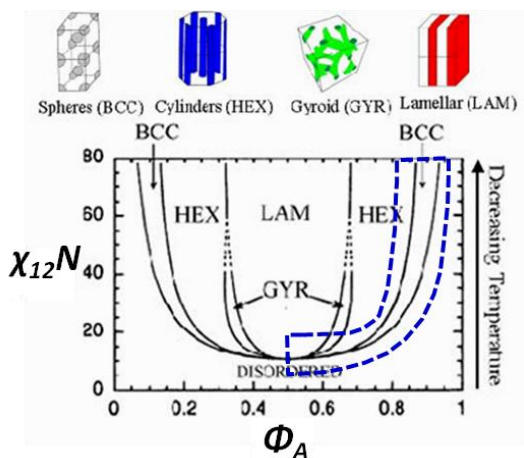


Figure 2.2. Target values of $\chi_{12}N$ and Φ_A . Adopted from Huck *et. al.*, the plot shows target values of $\chi_{12}N$ and Φ_A outlined in blue.³ Reprinted with permission from *Chemical Communications* **2005**, 4143-4148. 2014 Copyright Clearance Center, Inc.

When spiropyran isomerizes, it is assumed that the volume change in the block copolymer is negligible, and the volume fraction, Φ_A , will not change with changes in χ_{12} , as discussed in Chapter 1. However, changes in $\chi_{12}N$ may be able to influence the domain order. A block copolymer with both blocks above the respective T_g may be able to undergo a transition from the disordered domain to the spherical and cylindrical domain by increasing $\chi_{12}N$.

It should be recognized that such a transition was the initial aim of the approach, but a domain change was not conclusively observed. Rather, a block copolymer film demonstrated a spherical/cylindrical phase separation domain that could be recruited to the surface by UV light. The synthesis of block copolymers containing SP monomers covalently attached to the polymer backbone is described. The reaction rates of MC to SP in the bulk of these copolymers in the dry state were investigated by UV-vis spectroscopy. Images from TM-AFM of spin coated films have shown UV-induced transitions in both the phase and height channels, suggesting some degree of domain mobility at the air-polymer interface.

Results

General Chain Extension Polymerization (detailed extension polymerizations in Appendix A)

Two similar classes of block copolymers were built to investigate nano-phase separation, A-B type and A-B-A type block copolymers. Preservation of end groups was determined by the reaction kinetics monitored by GC and GPC and the molecular weight was determined from GPC and NMR analysis. Initiator group analysis by ^1H NMR helps in determining the molecular weight when macroinitiators below about $10,000 \text{ g}\cdot\text{mol}^{-1}$ are formed. An example GPC kinetic plot and chain extension from a relatively monodisperse poly(n-butylacrylate-Br), p(nBA-Br), macroinitiator is shown in Figure 2.3

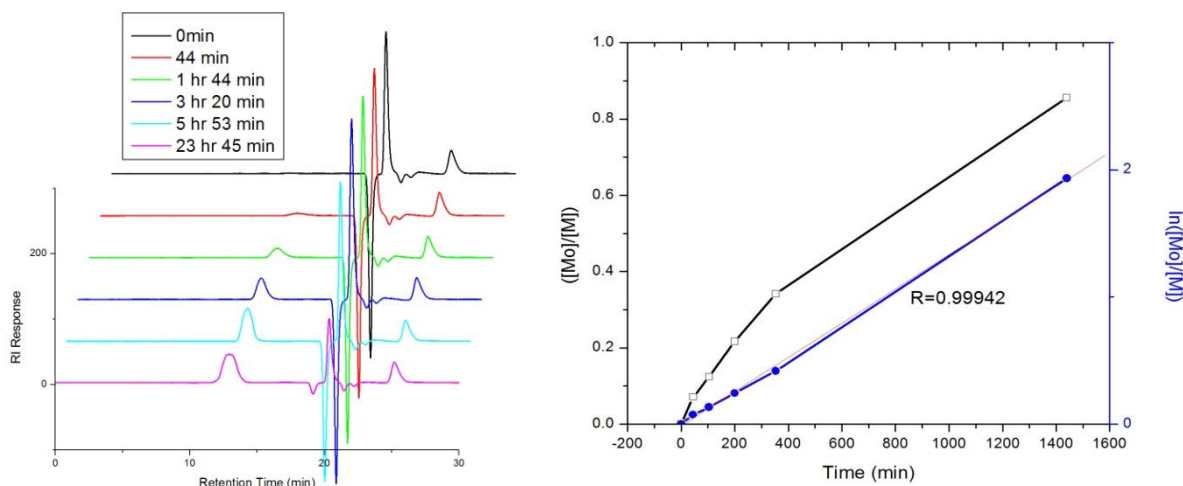


Figure 2.3. GPC reaction kinetic profile of p(nBA-Br). The formation of the polymer can be followed by the formation of the peak at 14.7 minutes which shifts to 13.5 minutes through the reaction. The monomer and internal standard, anisole, elute at 19.2 and 20.4 minutes, respectively. Right: Plot of conversion versus time, black, and first order kinetic plot, blue, to determine the rate order of the polymerization.

The formation of polymer can be monitored from aliquots taken throughout polymerization. Typically, several samples taken in the first few hours of polymerization provide sufficient data points to determine the reaction rate and to predict polymerization quenching time. The first order reaction kinetics may be determined by integration of the Refractive Index (RI) signal of the monomer versus the internal standard. The monomer conversion, C , may be related to the rate of polymerization by monitoring monomer consumption by GC or GPC using the relationship

$$C = 1 - \left(\frac{M_x}{S_x} \frac{M_0}{S_0} \right) \quad \text{(Equation 2.1)}$$

where M_x and S_x represent the monomer and internal standard integrated signals, respectively, at a given time, x , of the reaction. M_0 and S_0 represent the respective initial signals from the monomer and standard. Control of the polymerization was determined by linear analysis of the first order conversion plot for macroinitiators; conversion data, volume fraction, and molecular weight are presented in Table 2.1.

Table 2.1 SPA influence on polymerization conversion. The SPA mol percent represents molar concentration relative to p(nBA) block. Φ_B represents the volume fraction of the second p(nBA) block of the copolymer. The dispersity, D , of the polymer and conversion, C , were determined from GPC and GC data, respectively.

Polymer	Sample	SPA mol %	Φ_A (acrylate)	M_n theor.	M_n GPC	M_n NMR	D	C
1	p(MMA ₇₇ -Br/Cl)	N/A	0.00	5,186	7,877	6,644	1.046	51%
2	P(MMA ₇₇ -b-nBA ₁₄₂)	0%	0.89	26,220	40,377	30,612	1.072	35%
3	P(MMA ₇₇ -b-nBA ₃₈ -co-SPA ₄) dNbpv	10%	0.34	14,871	18,240	14,396	1.222	11%
4	P(MMA ₇₇ -b-nBA ₅₂ -co-SPA ₆) PMDETA	10%	0.48	17,062	19,600	17,600	1.175	15%

As can be seen from GC conversion data, the conversion of polymerizations incorporating 10 mol % spiropyran in the second block was reduced. This is the case of all polymerizations using spiropyran (meth)acrylate monomers, which suggests the ATRP catalyst is interacting with the chromophore. The increased dispersity can be seen in Figure 2.4.

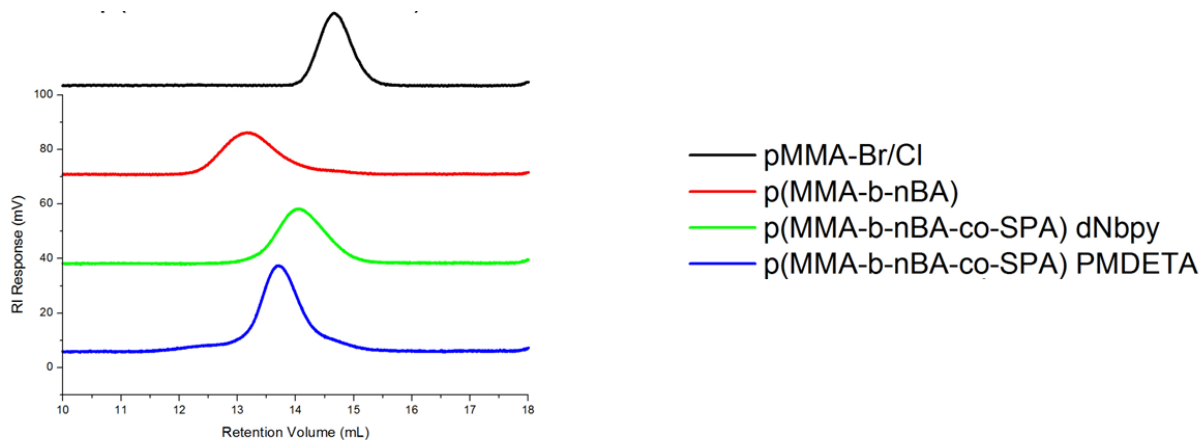


Figure 2.4. Chain extension of pMMA-Br/Cl with p(nBA). Reaction conditions and polymerization times are equivalent for chain extension polymerizations, red, green and blue traces, varying ligand choice between dNbpy and PMDETA.^a

The author speculates that the MC isomer act as a competing ligand to dNbpy or PMDETA ligands, affording loss of polymerization control when compared to a control reaction, Polymer 2 in Table 2.1. Furthermore, binding of the MC isomer to copper has been demonstrated spectroscopically in the literature.⁴⁻⁶ The lower conversion and increase in dispersity, \mathcal{D} , also support the argument of catalyst poisoning early in the polymerization; however, the polymerization continues to sufficient conversion to form low molecular weight blocks. It is important to note that all polymers built via ATRP which contain spiropyran chromophores were not able to reinitiate in a subsequent polymerization.

From the molecular weight acquired by the three techniques, an average value for MW may be predicted to determine the phase separation architecture of these block copolymers. The degree of polymerization, N , is the sum of all repeat units in a given polymer and the volume fraction, Φ_A , may be determined by manipulation of physical parameters. This relationship is governed by Equation 2.2

$$\Phi_A = \left(\frac{\rho_A n_B MW_B}{\rho_B n_A MW_A} + 1 \right)^{-1} \quad (\text{Equation 2.2})$$

where ρ_A and ρ_B represent the polymer the density of each block, n_A and n_B represent the molar ratio of each block's monomer repeat unit, and MW_A and MW_B are the molecular weight of each block.

For block copolymers where the second block is a copolymer, i.e. a mixture of SPA and nBA as in Polymer 3, the solubility parameter for that block must also be determined by the weighted volume fraction average of the dispersion partial solubility parameter, $\delta_{average, D}$, described by Equation 2.3

$$\delta_{average, D} = \varphi_a \delta_{D,a} + \varphi_b \delta_{D,b} \quad (\text{Equation 2.3})$$

where φ_a and φ_b represent the volume fractions of the comonomers SPA and nBA contained within the same block, respectively ($\varphi_a + \varphi_b = 1.0$). $\delta_{D,a}$ and $\delta_{D,b}$ correspond to the calculated HSP for comonomers SPA and nBA, respectively. The calculation for φ_a is treated the same as Equation 2.2, except the density, molar ratio, and molecular weight values correspond to comonomers in the block same block. The weighted volume fraction average of the polar and hydrogen bonding parameters $\delta_{average, P}$ and $\delta_{average, H}$, are treated in the same manner. The calculated Hansen partial solubility parameters are tabulated in the appendix in this chapter.

By the group contribution method introduced by van Krevelen and modified by Stefanis, the solubility parameter of each may be determined the dimensionless Flory interaction parameter, χ_{12} , described in Chapter 1, which may be determined by group contribution of Hansen partial solubility parameters by the relationship:

$$\chi_{1,2} = \frac{V_{mol}[(\delta_{D1} - \delta_{D2})^2 + 0.25(\delta_{P1} - \delta_{P2})^2 + 0.25(\delta_{H1} - \delta_{H2})^2]}{RT} \quad (\text{Equation 2.4})$$

The subscripts for δ_{D1} , δ_{P1} , and δ_{H1} correspond to block A while the subscripts for δ_{D2} , δ_{P2} , and δ_{H2} correspond to block B. The temperature, T , is considered in Kelvin, and R is the universal gas

constant ($8.3144621 \text{ cm}^3 \cdot \text{MPa} \cdot \text{K}^{-1} \cdot \text{mol}^{-1}$). The molar volume in $\text{cm}^3 \cdot \text{mol}^{-1}$, V_{mol} , is determined by the fraction average of each block's repeat unit composition as described by Equations 2.5 and 2.6.

$$V_{mol,A} = \frac{\varphi_a mw_a + \varphi_b mw_b}{\varphi_a \rho_a + \varphi_b \rho_b} \quad (\text{Equation 2.5})$$

$$V_{mol,B} = \frac{\varphi_a mw_a + \varphi_b mw_b}{\varphi_a \rho_a + \varphi_b \rho_b} \quad (\text{Equation 2.6})$$

Where ρ_a and ρ_b are the densities of each copolymer in the block, respectively ($1.185 \text{ g} \cdot \text{cm}^3$ and $1.089 \text{ g} \cdot \text{cm}^3$ for p(MMA) and p(nBA)). If the block is homogeneous, i.e. $\varphi_a = 1.0$ and $\varphi_b = 0.0$, and the second term drops from the equation. The value for V_{mol} in Equation 2.4 is the average of $V_{mol,A}$ and $V_{mol,B}$. The terms mw_a and mw_b are the molecular weight of each copolymer in the block. The parameters outlined in Table 2.2 were calculated by this approach to predict phase separation of A-B type spiropyran containing block copolymers.

Table 2.2. Calculations for $\chi_{12}N$ for SPA-containing polymers. Spiropyran-containing block copolymers repeat units were determined from ^1H NMR, GPC, and GC conversion data.

Polymer	Sample	M_n average	Φ_A (nBA)	Φ_B (MMA)	χ_{12}	N	$\chi_{12}N$
1	p(MMA ₇₇ -Br/Cl)	6,569	0.00	1.00	N/A	77	0
2	p(MMA ₇₇ -b-nBA ₁₄₂)	32,403	0.89	0.11	0.20	221	44.2
3	p(MMA ₇₇ -b-nBA ₃₈ -co-SPA ₄) dNbpv	15,836	0.34	0.66	0.28	119	33.2
4	p(MMA ₇₇ -b-nBA ₅₂ -co-SPA ₆) PMDETA	18,087	0.48	0.52	0.29	135	39.1

By inspection of the idealized phase separation plot in Figure 2.2, we can predict which phase separation domain is likely to occur in a spin coated film. The phenomenon of nano-phase separation of these polymers as thin films can be investigated with TM-AFM.

TM-AFM of Spin Coated block copolymer films

Spin coated films cast from dilute polymer solutions were prepared on silicon in all cases. When the solvent evaporates to dryness in air, a dry-state block copolymer film resolves; these architectures can be measured by the phase and height channels to confirm the domain of nano-phase separation as predicted by Φ_A and $\chi_{12}N$. Imaged in Figure 2.5 is a 59 nm spin coated film of p(nBA-b-MMA) prepared by sequential monomer addition.

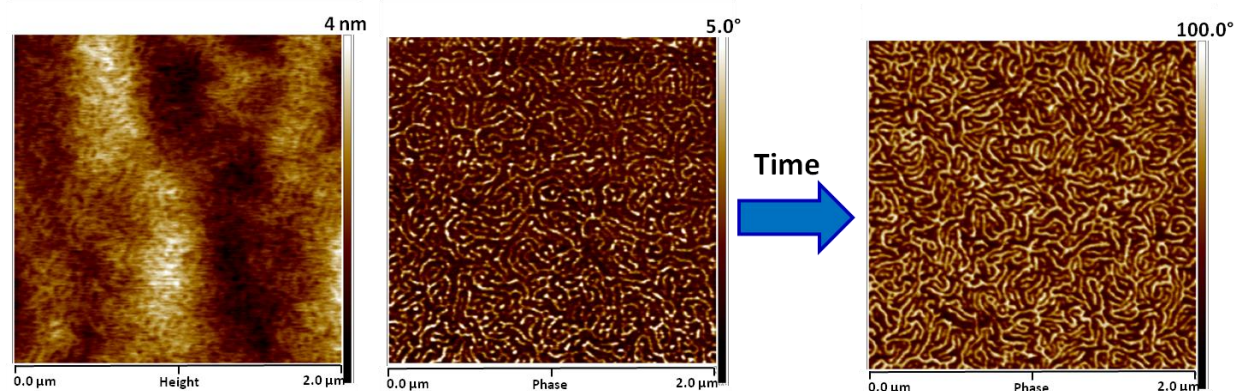


Figure 2.5. Spin coated film on silicon of p(nBA-b-MMA-co-nBA), Polymer 7. $\Phi_A = 0.88$ by sequential monomer addition. These block copolymers anneal at room temperature due to the low T_g of the nBA block. Note the change in the phase Z-scale after room temperature annealing.

An advantage of sequential monomer addition is a one-pot synthetic approach to achieve high conversions of the second block, and to investigate the properties of block copolymers of a homopolymer-block-mixed copolymer type architecture. The domain organization shown here is the cylindrical domain, and this polymer demonstrates elastic properties. When the column fraction of the MMA block is lowered slightly in a tri-block copolymer, a cylindrical/spherical order is observed. Below is height and phase TM-AFM data from annealing a p(nBA-b-MMA-co-nBA) films above T_g with $\Phi_A = 0.86$ for p(nBA) block.

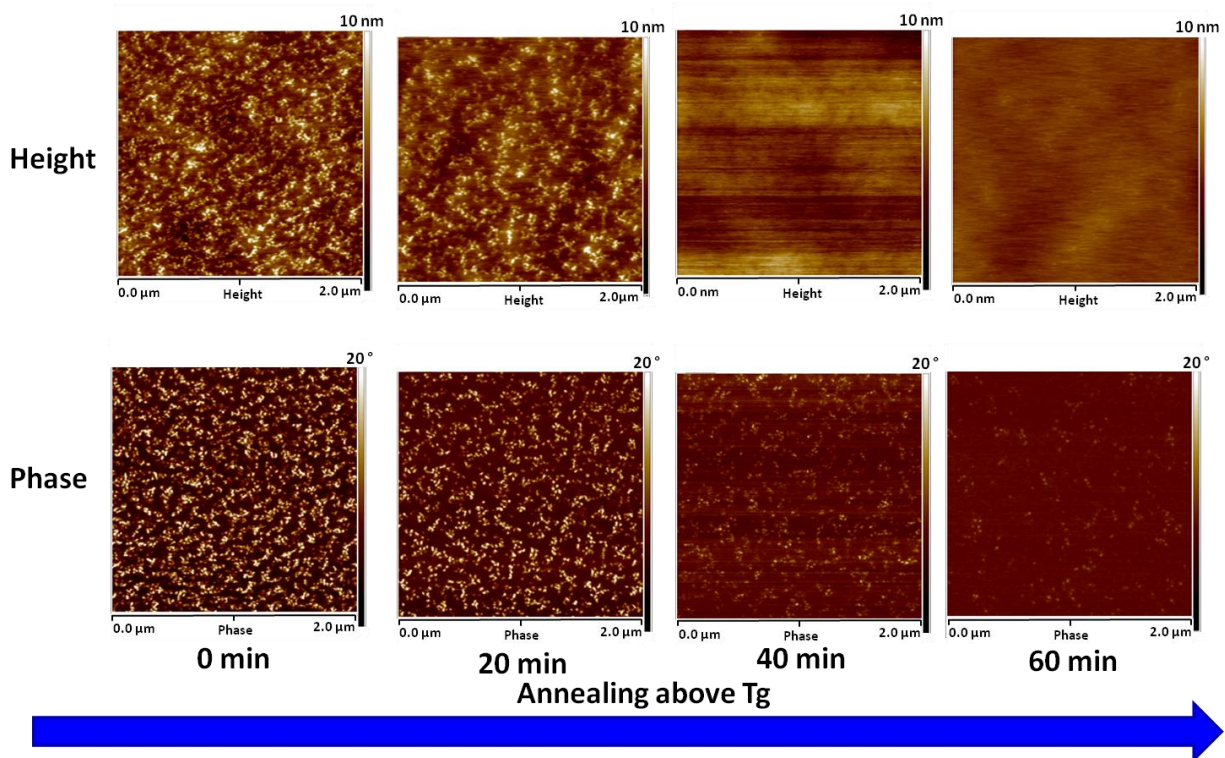


Figure 2.6. TM-AFM annealing study, Polymer 8. $P(\text{MMA}_{50}\text{-co-nBA}_4\text{-b-nBA}_{310}\text{-b-MMA}_{50}\text{-co-nBA}_4)$ samples were annealed at 100°C in ambient conditions for 60 minutes. The $p(\text{MMA})$ domains can be seen migrating below the surface and exposing nearly homogeneous $p(\text{nBA})$ domains.

As can be seen from the AFM data, a somewhat heterogeneous packing of near-spherical domain orientation is observed. The thermal annealing accelerates the phase separation to a steady-state orientation and did not change after 1 hour annealing. The major domain correlates to the lower phase change signal (darker regions in phase image) and represents the low T_g $p(\text{nBA})$ block. The lighter spherical domains represent the $p(\text{nBA}_4\text{-co-MMA}_{50})$ domains of the second block. The parameters for this polymer are outlined in Polymer 8 in Table 2.3. However, when the film is annealed at 110°C at 20 minute intervals in ambient atmosphere, the $p(\text{nBA})$ block appears to rise to the air-polymer interface by the homogenization in the phase and height

image. As described in more detail in Chapter 1, the Hansen solubility parameter for each block may be determined by Equation 2.7.

$$\delta = \delta_d^2 + \delta_p^2 + \delta_h^2 \quad (\text{Equation 2.7})$$

The calculated Hansen partial solubility parameters for p(nBA) and p(MMA) are outlined in the supporting information. The other calculated solubility parameters for other block copolymers in this work are outlined in the appendix.

As predicted by the group contribution method, the Hansen solubility parameter, δ_t is calculated to the 20.21 Mpa^{1/2} for p(nBA) and 20.55 Mpa^{1/2} for p(MMA), respectively. Polar solvents such as the water layer inherently present during ambient TM-AFM imaging have a high solubility parameter, 47.807 Mpa^{1/2}.⁷ The migration of p(nBA) to the surface during annealing supports the values calculated by this method. By comparison, the Hildebrand solubility parameters of 18.41 and 19.43 Mpa^{1/2} for p(nBA) and p(MMA), respectively.

True block copolymers were also prepared from macroinitiators to generate a relatively more homogeneous domain segregation pattern. The A-B-A type block copolymers of Polymer 8 and 9 in Table 2.3 are both dominantly p(nBA) with comparable Φ_A values, 0.954 and 0.908 for Polymer 8 and 9, respectively. Similarly, the dimensionless $\chi_{12}N$ values are comparable at 83.92 and 62.33 for Polymer 8 and 9, respectively.

Table 2.3. Calculations for $\chi_{12}N$ for mixed block copolymers. Values for the volume fractions, Φ_A and Φ_B , were determined from Equation 2.2.

Polymer	Sample	M_n average	Φ_A (acrylic)	Φ_B (methacrylic)	χ_{12}	N	$\chi_{12}N$
5	p(Br-MMA ₇₅ -Br)	7,837	0	1	0	75	0
6	p(Br-nBA ₂₆₁ -Br)	33,871	1	0	0	261	0
7	p(nBA ₃₈₀ -b-MMA ₁₃₇ -co-nBA ₁₄)	64,410	0.886	0.114	0.1995	531	105.6
8	p(MMA ₅₀ -co-nBA ₄ -b-nBA ₃₁₀ -b-MMA ₅₀ -co-nBA ₄)	51,100	0.954	0.0459	0.2008	418	83.92
9	p(MMA ₂₂ -b-nBA ₂₆₁ -b-MMA ₂₂)	43,246	0.908	0.0916	0.2044	305	62.33

The phase images of p(MMA₅₀-co-nBA₄-b-nBA₃₁₀-b-MMA₅₀-co-nBA₄) and p(MMA₂₂-b-nBA₂₆₁-b-MMA₂₂) true block copolymer are shown in Figure 2.7. The un-annealed film of the true block copolymer shows more uniform phase separation in the spherical domain, and was built from the macroinitiator p(Br-nBA-Br)₂₆₁, Polymer 6. More distinct spherically phase separated and chain extended polymers may be built from macroinitiators when compared to the sequential addition method as seen by AFM phase imaging.

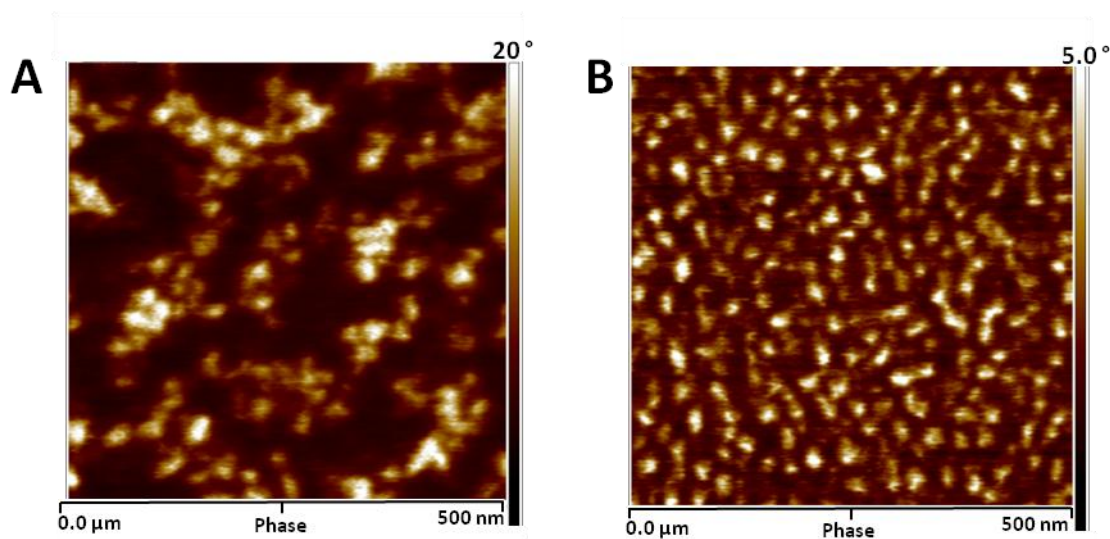


Figure 2.7. TM-AFM images of A-B-A type block copolymers. The polymers were prepared by sequential monomer addition (left) and from a macroinitiator substrate (right).

The volume fraction of the heterogeneous block may be calculated by applying Equation 2.2 for the mixed block, giving φ_a and φ_b of 0.9901 and 0.0098 for the MMA and nBA content, respectively. The 1% volume fraction content of nBA in the p(MMA) block is sufficient to disorder the film organization at the air interface. Due to the small influence of nBA affecting the domain ordering, chromophore containing block copolymers are prepared from macroinitiators. Two polymers are compared to investigate the chromophore isomerization kinetics in the p(nBA) and p(MMA) matrixes as dry films. A polymer with the chromophore in a low T_g acrylate block and a polymer with the chromophore in the high T_g methacrylate blocks are compared. The corresponding calculated parameters for the polymers are shown in Table 2.4.

UV-vis Kinetic Study of Spiropyran-Merocyanine Isomerization

Spin coated films were all cast from acetonitrile for the block copolymers, affording uniform films devoid of pit or holes. The films were irradiated with 365 nm UV light to observe the chromophores UV-induced isomerization from spiropyran to merocyanine. Irradiation for 10 minutes at $0.125 \text{ mW}\cdot\text{cm}^2$ is not sufficient time to convert all species to the ring open isomers as can be seen in kinetic plot A of Figure 2.8 by following the formation of the merocyanine peak at 575 nm as shown in the spectral waterfall plot C. In order to avoid prolonged exposure time, which leads to photobleaching of the sample, the ring-opening isomerization was stopped at 10 minutes irradiation and the thermally induced ambient isomerization back to the ring-closed spiropyran was monitored at 575 nm by the disappearance of the peak, plot B in Figure 2.8. This process is reversible dozens to hundreds of times before a photobleached films are generated.

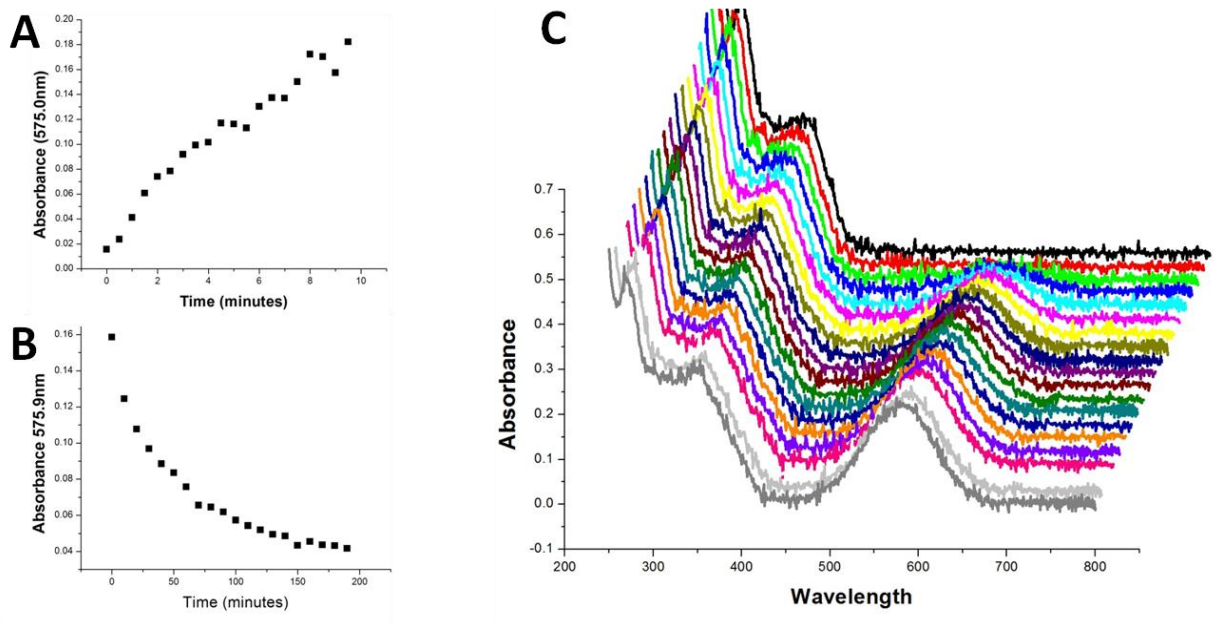


Figure 2.8. Kinetic plots of SP to MC isomerization. **A**, MC to SP isomerization, **B**, and waterfall plot **C** of SP to MC. The black trace represents $t = 0$ min UV irradiation of a 56 nm spin coated film on a quartz slide.

It is important to note that the films do vary in thickness, with an average thickness of approximately 56 nm by ellipsometry. This affords significant varying spiropyran content between samples, and despite the uses of a stable and constant irradiation source, non-linear kinetics are observed for four spiropyran-containing polymers as expected for irradiation of dissimilar film composition and thickness, as shown in Figure 2.9.

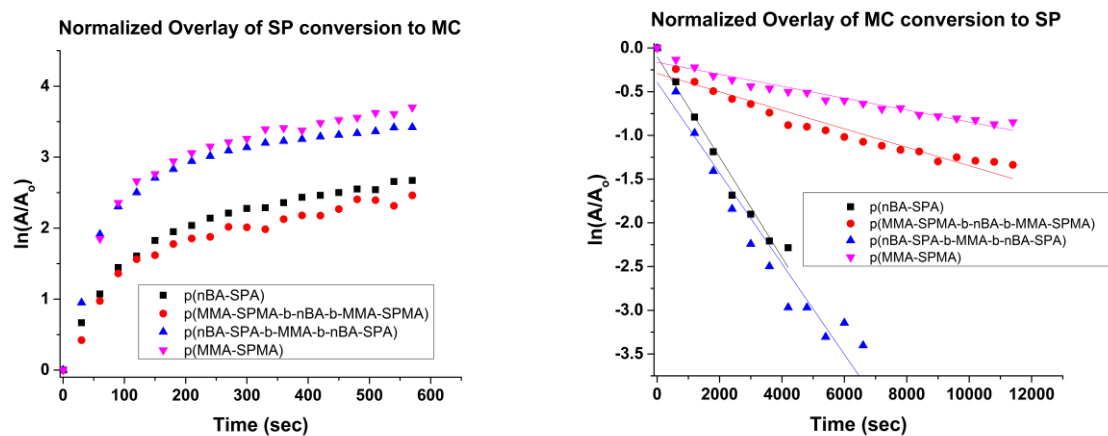


Figure 2.9. Normalized isomerization reaction profiles. Left: normalized overlay of SP to MC for four spiropyran-containing copolymers. Right: the corresponding ring-closing isomerization of MC to SP in ambient conditions.

The ring closure isomerization demonstrates near first-order kinetics in all polymers; however, the linear analysis provided in Table 2.4 shows still a slight deviation from first-order kinetics, k_i , which may be determined by the linear fit R-squared values.

Table 2.4. Comparison of MC-SP ring-closure isomerization rates. Low R^2 values indicate first-order reaction kinetics deviate from linearity due to matrix effects.

Polymer	Sample	$k_i \times 10^4 \text{ (s}^{-1}\text{)}$	R^2
10	p(MMA ₃₀ -co-SPMA ₁₅ -b-nBA ₂₆₁ -b-MMA ₃₀ -co-SPMA ₁₅)	1.05	0.919
11	p(nBA ₆₈ -co-SPA ₃ -b-MMA ₇₅ -b-nBA ₆₈ -co-SPA ₃)	5.19	0.935
12	p(nBA-co-SPA)	5.74	0.973
13	p(MMA-co-SPMA)	0.682	0.942

Matrix dependant reaction rates were also observed by Albrecht and coworkers in a p(MMA) polymer bulk material doped with methyl spiropyrans, and the mathematical treatment of this dynamic rate was applied to temperature dependant decoloration rates.⁸

Similar to the UV-vis data experiments, equivalent UV exposure doses for in situ TM-AFM imaging were performed on photochromic spiropyran-containing A-B-A type tri-block copolymers where the outside groups contain the chromophore monomer. The experimental set up is depicted in Figure 2.10.

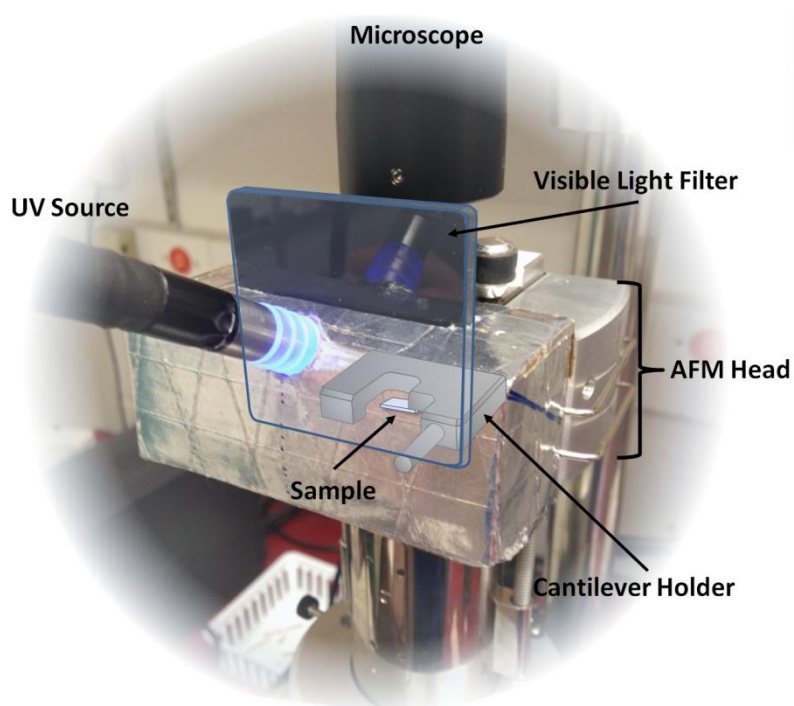


Figure 2.10. Experimental in situ UV AFM set-up. The UV filter upper cut-off is about 390 nm. This is to prevent photonic contamination from the UV source during the experiment by eliminating the visible purple light.

The two polymers of interest, 10 and 11, are presented in Table 2.5. The calculated Flory interaction parameter, $\chi_{12}N$, for Polymer 10 is calculated from the solubility parameters of

the spiropyran form, the zwitterionic merocyanine form, and the neutral quinodal isomer labeled 10_a, 10_b, and 10_c, respectively. The same isomer labeling is applied to Polymer 11 as well. In the calculations, the volume fractions, Φ_A and Φ_B , are assumed to remain constant.

Table 2.5. Physical parameters for the spiropyran block copolymers. The values for $\chi_{12}N$ were determined for polymers before irradiation (SPMA and SPA), for the UV-induced zwitterionic merocyanine (MCMA and MCA), and the UV-induced quinodal form (QMA and QA).

Polymer	Sample	M_n average	Φ_A (acrylic)	Φ_B (methacrylic)	χ_{12}	N	$\chi_{12}N$
10a	p(MMA ₃₀ -co-SPMA ₁₅ -b-nBA ₂₆₁ -b-MMA ₃₀ -co-SPMA ₁₅)	52,798	0.9188	0.0812	0.8012	352	282.1
10b	p(MMA ₃₀ -co-MCMA ₁₅ -b-nBA ₂₆₁ -b-MMA ₃₀ -co-MCMA ₁₅)	52,798	0.9188	0.0812	0.3659	352	57.12
10c	p(MMA ₃₀ -co-QMA ₁₅ -b-nBA ₂₆₁ -b-MMA ₃₀ -co-QMA ₁₅)	52,798	0.9188	0.0812	0.3461	352	121.8
11a	p(nBA ₆₈ -co-SPA ₃ -b-MMA ₇₅ -b-nBA ₆₈ -co-SPA ₃)	27,589	0.5762	0.4238	0.3996	217	86.71
11b	p(nBA ₆₈ -co-MCA ₃ -b-MMA ₇₅ -b-nBA ₆₈ -co-MCA ₃)	27,589	0.5762	0.4238	0.3393	217	73.62
11c	p(nBA ₆₈ -co-QA ₃ -b-MMA ₇₅ -b-nBA ₆₈ -co-QA ₃)	27,589	0.5762	0.4238	0.2343	217	50.85

With Φ_A held constant, UV treatment may only influence the domain location along the y-axis of the phase separation diagram shown in Figure 2.2. In the case of low spiropyran content in the acrylate block of a cylinder-domain block copolymer, UV irradiation for 12 minutes affords no significant change in the height or phase image as shown in Figure 2.11.

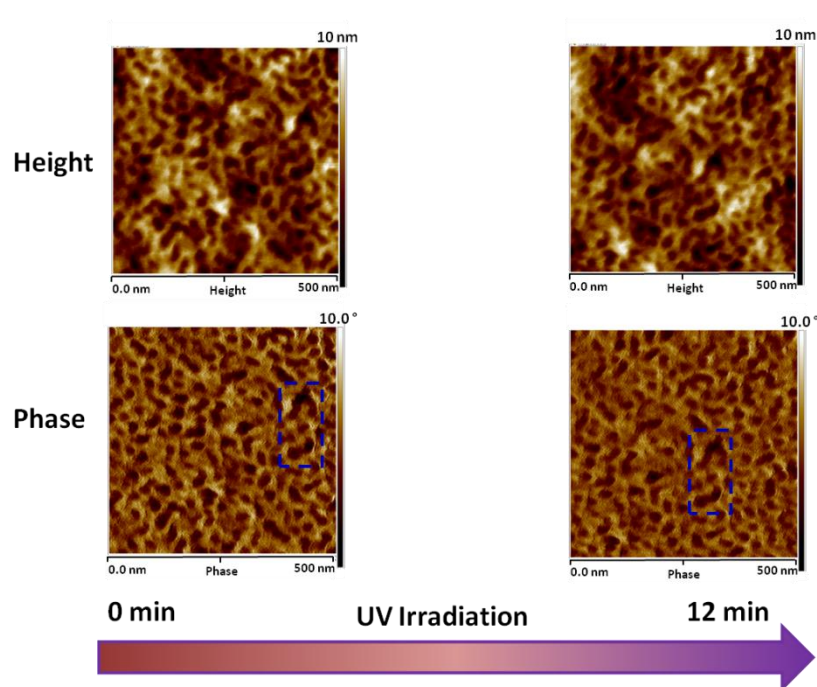


Figure 2.11. TM-AFM height and phase images of photochromic block copolymer 11. A 61 nm A-B-A type photochromic block copolymer film is shown with spiropyran in the low T_g acrylate block. The dashed blue represents the same structure as the film drifted slightly over 12 minutes. This film was prepared from Polymer 11a.

No molecular movement is observed when UV-induced $\chi_{12}N$ changes are small and the volume fraction Φ_A is low (0.5762) giving cylindrical domain phase separation. The calculated changes in $\chi_{12}N$ for Polymer 11 is 86.71 for the spiropyran form before irradiation and 73.62 and 50.85 for the merocyanine and quinodal form of the polymer, Polymer 11b and Polymer 11c, respectively. In order to further encourage a domain change, a polymer with a higher Φ_A value for and larger swings in $\chi_{12}N$ must be required. Polymer 10 has a larger content p(nBA) with $\Phi_A = 0.9188$, and calculated changes in $\chi_{12}N$ of 282.16 for the pre-UV spiropyran polymer and 57.12 and 121.84 for the post-UV merocyanine and quinodal isomeric forms of the polymer. Upon

UV-irradiation of this film as shown in Figure 2.12, a distinct change in the phase image was observed within similar time frame experiments for UV-vis studies.

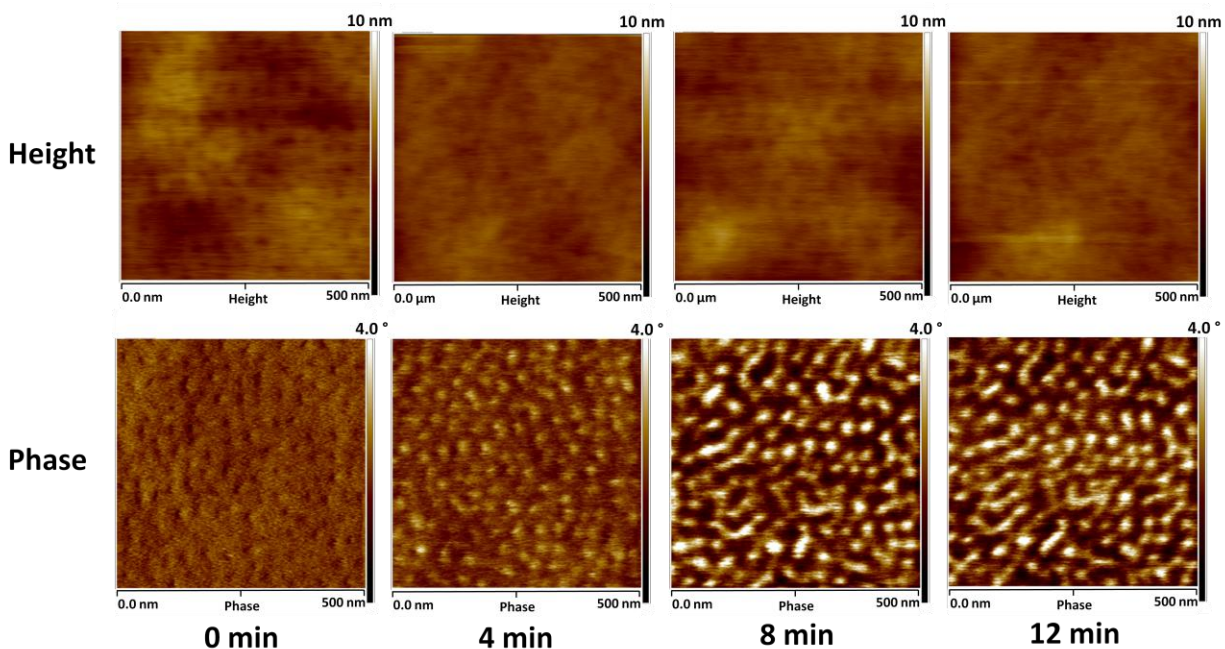


Figure 2.12. TM-AFM height and phase images of photochromic block copolymer 10. A 50 nm A-B-A type photochromic block copolymer is shown with spiropyran in the high T_g methacrylate block. This film was prepared from Polymer 10a. UV irradiation was conducted *in situ*, using a visible light filter.

This phenomenon was reproducible several times with this polymer, and with two separate spin coated films. The UV filter in Figure 2.10 was built in efforts to prevent UV-source light influence of the diode photodetector in the AFM head, so the author suggests that this is not an artifact of light contamination from the technique. In four independently prepared films, a similar change in the phase image was observed. Interestingly, in one sample a significant change in the topology image was also observed as shown in Figure 2.13; the arrows in the image represent scan direction. The changes in the phase image are suggested to be small

distance reorganization of the domain with no overall domain change. The z-distance reorganization of the glassy pMMA-co-SPMC blocks is suspected to be correlated to the z-piezoelectric changes in distance, proportional to the height image. However, the overall representation of polymers just below the surface in the bulk of the film is hard to assess by a surface technique like TM-AFM.

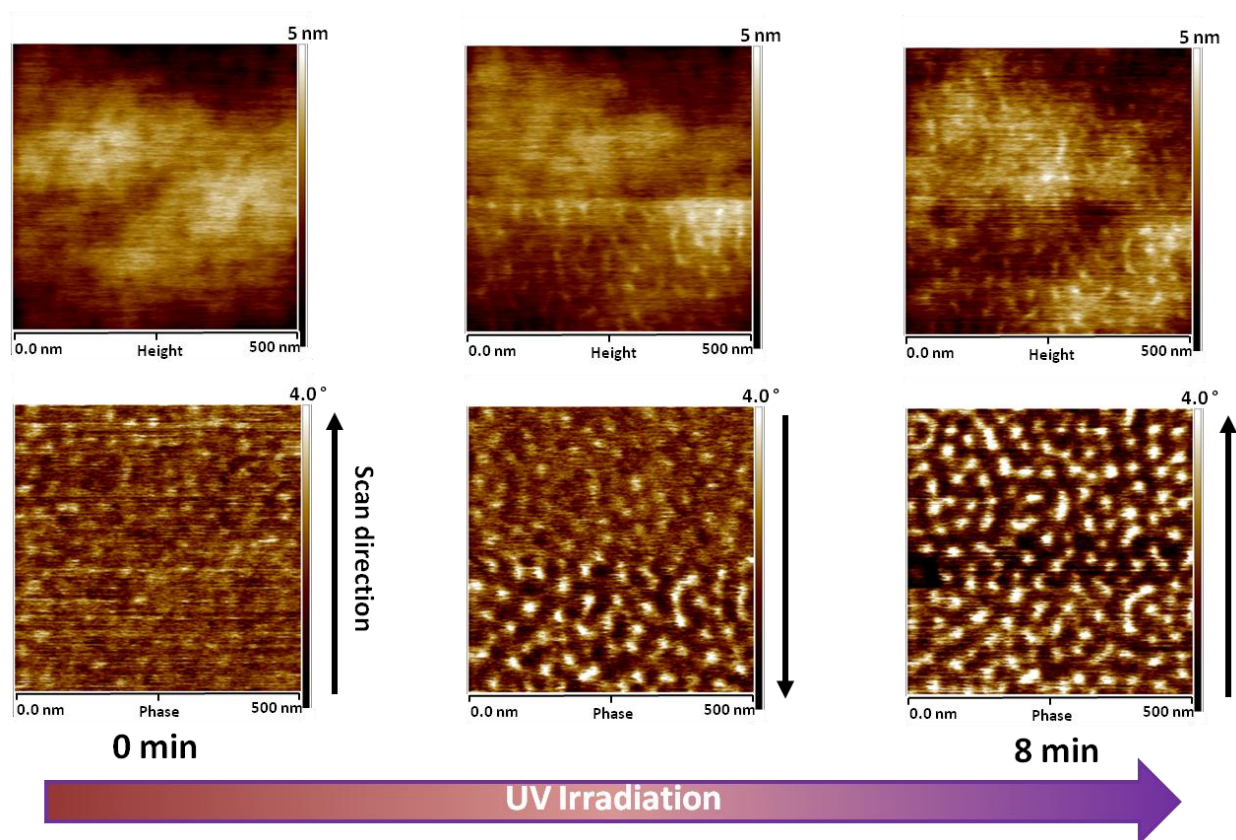


Figure 2.13. In situ observation of discrete phase changes of Polymer 10. p(MMA₃₀-co-SPMA₁₅-b-nBA₂₆₁-b-MMA₃₀-co-SPMA₁₅). At approximately 4 minutes UV-irradiation, the polymer film interface demonstrated a phase transition. It's important to note that scanning parameters were kept constant throughout the experiment.

When the computed values of $\chi_{12}N$ and Φ_A of the polymers considered in this work are plotted on a nano-phase separation diagram, a better picture for this p(nBA) and p(MMA) system can be seen by Figure 2.14.

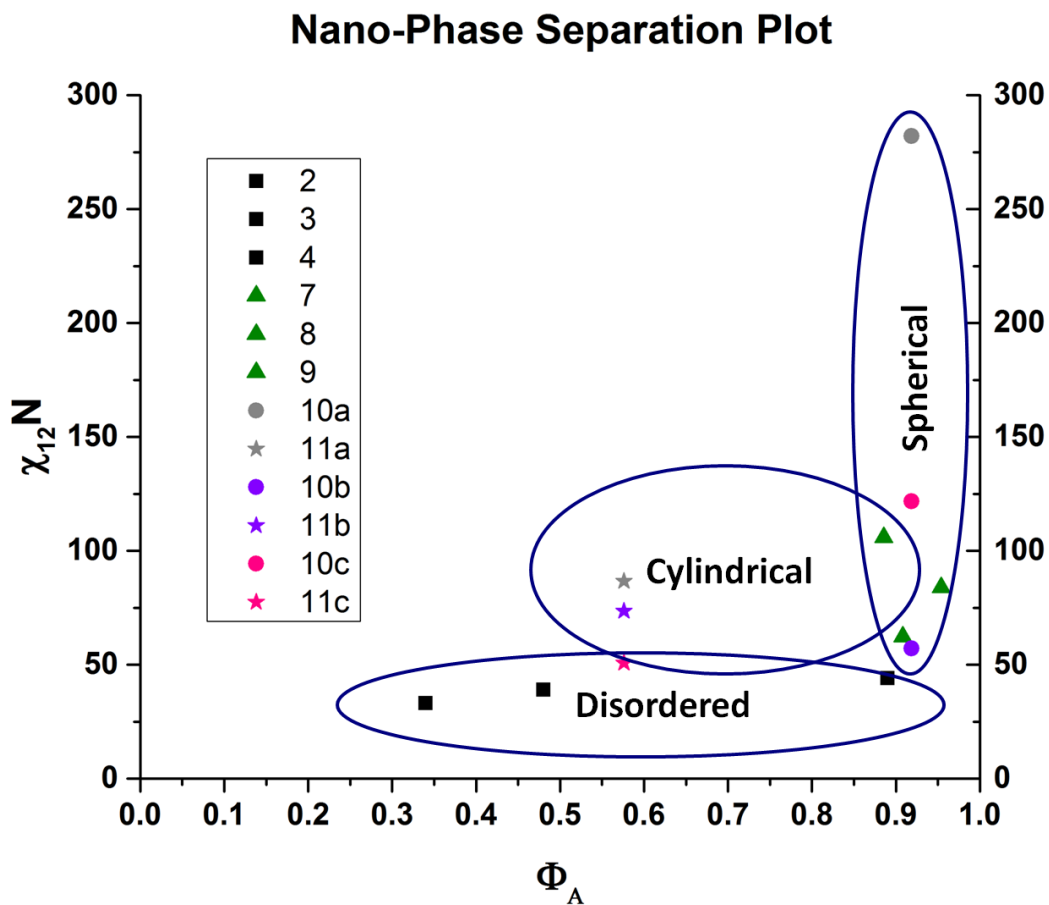


Figure 2.14. Nano-phase separation plot of block copolymers. The homopolymers are not included in this diagram. The gray symbols corresponds to spiropyran polymers, the purple symbols correspond to merocyanine polymers, and the pink symbols correspond to the quinodal isomer.

The values presented in this plot are calculated predictions; however, some assumptions on the group contributions must be considered. The group contribution method presented by

Stefanis clearly demonstrates good agreement other methods for polymers with simple side groups and fewer atoms, such as p(nBA) and p(MMA). There is no present first- or second-order group contribution assignment in the literature to date for treatment of zwitterionic, conjugated heterocyclic, or some other second-order conformations known to be present in the merocyanine form.⁵ These values seem to predict well phase separation of the mixed block samples with no spiropyran content like spherically phase separated Polymers 7 and 8, as confirmed by AFM imaging. The solubility parameter, δ_t , for the zwitterionic form of both p(MCMA) and p(MCA) polymers, 22.65 MPa^{1/2} for 10b and 26.90 MPa^{1/2} for 11b, is lower than that of the quinodal form of p(QMA) and p(QA), 24.41 MPa^{1/2} for 10b and 26.30 MPa^{1/2} for 11b, respectively. However, the predicted δ_t for the spiropyran blocks seem to be overstated, with 29.15 MPa^{1/2} for p(SPA) and 27.32 MPa^{1/2} for p(SPMA), respectively.

Conclusions

This work presents the synthesis of photochromic block copolymers containing spiropyran as a UV probe. A-B type and A-B-A type block copolymers were fabricated by sequential monomer addition and from macroinitiators to compare nano-phase separation profiles by TM-AFM. The observed MC-SP ring-closing isomerization demonstrated near first-order rates in tri-block copolymers fabricated from acrylic and methacrylic comonomers. A polymer fabricated with a high mole percent of spiropyran monomer in the methacrylate block demonstrated reproducible UV-induced phase transitions observed by TM-AFM.

The phase transition observed in photochromic polymer films is ascribed to small domain re-organization at the polymer-air interface. The inherent water layer present in ambient AFM conditions and the associated changes in the solubility parameter of the UV-active block, δ_t ,

influences the value of $\chi_{12}N$. This change in polymer-polymer miscibility may provide sufficient entropic changes in the dissimilar polymer matrix to encourage these changes. In order to confirm this theory, computational closer assessment of group contributions should be considered for the chromophore and all possible isomers, and 2nd order contributions may need to be added to the model to treat the isomers.

Experimental Details

Materials

Ethyl 2-bromo-2-methylpropanoate (Et₂Br) was used as received. Methyl ethyl ketone (MEK), methanol (MeOH), diphenyl ether (DPE), 4,4'-Dinonyl-2,2'-dipyridyl (dNbpy), *N*-methyl-*N,N,N*-trioctyloctan-1-ammonium chloride (aliquot 336), *p*-toluenesulfonyl chloride (TsCl), anhydrous copper(I) chloride (CuCl), and copper(I) bromide (CuBr), were used as received. The monomers *n*-butyl acrylate (nBA) and methyl methacrylate (MMA) were passed through a plug of neutral alumina and distilled under reduced pressure.

Synthesis of spiropyran(meth)acrylate

The general synthetic scheme for the synthesis of the spiropyran monomer is shown in Figure 2.15. The synthesis for precursor 1'-(2-hydroxyethyl)-3'-dimethyl-6-nitrospiro(2H-benzopyran-2,2'-indole) as product (**5**) may be found in the literature.⁹ The coupling reaction between either acrylic or methacrylic acid (**6**) was performed following the procedure by Prodi and coworkers.¹⁰

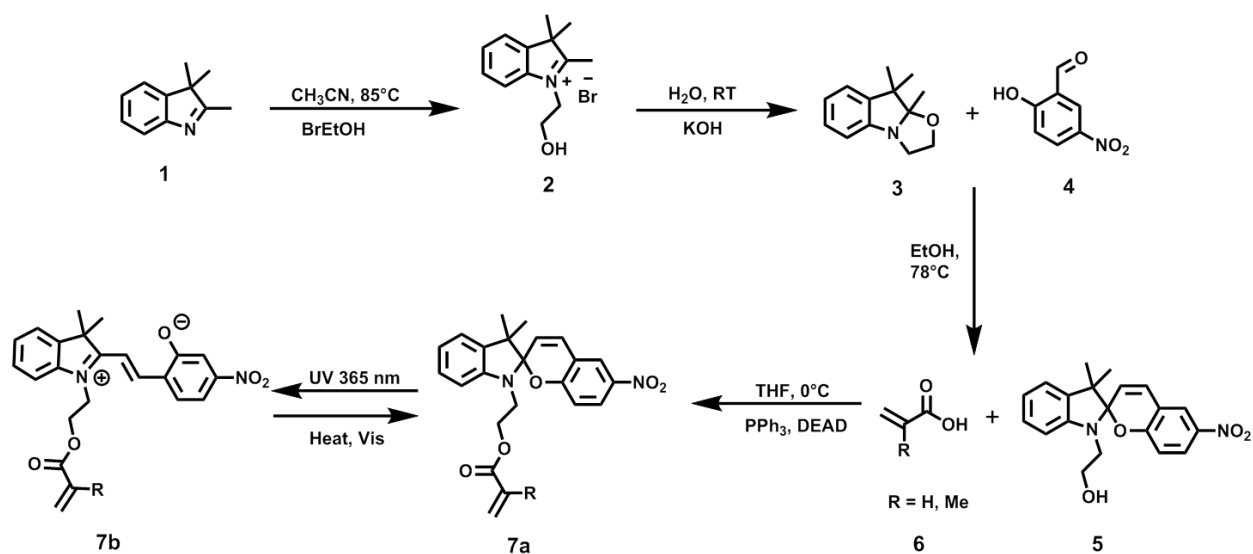


Figure 2.15. Schematic synthesis of spiropyran(meth)acrylate chromophore monomer.

Initiator Synthesis

The synthesis of the A-B-A type ATRP initiator ethane-1,2-diyl bis(2-bromo-2-methylpropanoate) (BBiBE) can be found in the literature.¹¹ The synthesis of the A-B-A type ATRP initiator dimethyl 2,6-dibromoheptanedioate (DMDBH) is also found in the literature.¹² The polymer constructed from Ethyl 2-bromo-2-methylpropanoate (Et2Br) as an initiator (Polymer 7) is depicted in Figure 2.16.

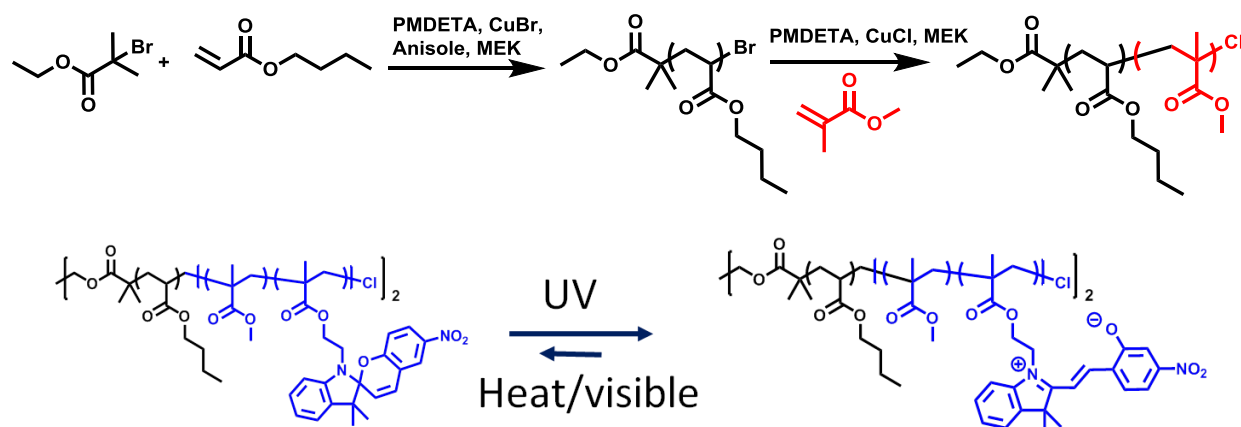


Figure 2.16. General approach for synthesis of block copolymers by ATRP. The UV-induced isomerization of a mixed block A-B-A type copolymer is depicted.

Formation of block copolymers by sequential addition is a notable way to form block copolymers in one-pot by taking advantage of halogen exchange between the terminal alkyl bromide of the growing chain and the addition of chloride to the catalyst. The formation of the second block may be monitored by the GC and GPC conversion of the introduced monomer and the residual monomer from the A block. All chromophore-containing polymers were prepared from macroinitiators. An advantage to preparing block copolymers this way is that the second, chain extended block will not contain any repeat units from the formation of the macroinitiator as shown in Figure 2.16, bottom.

Synthesis of p(MMA₇₇-Br/Cl) macroinitiator, Polymer 1

To a 35 mL Schlenk flask, 10.003 g of MMA (99.9 mmol), 500 μ L of anisole, 10.0 mL of DPE, and a stir bar were added and degassed for 1 hour with argon. To a 12 mL Schlenk flask, 2.0 mL DPE and 0.1888 g (TsCl) were added and degassed for 1 hour in a room temperature bath. After degassing 1 hour, 0.4046 g dNbpy (0.989 mmol) and 0.0718 g CuBr (0.989 mmol) were added to the MMA solution under positive pressure and degassing continued an additional 10 minutes, resolving a deep brown-red homogeneous solution. The MMA solution was equilibrated at 90°C, and an aliquot was taken for GC. The TsCl solution was injected via degassed syringe, displaying a color change from deep brown-red to a homogeneous dark green.

At 16 hours, 30 minutes elapsed polymerization time (conversion 51.3 %), an aliquot was taken, and the reaction was quenched by exposing to air, cooling to 0°C, and diluting with an equal volume of THF. This mixture was passed through a plug of basic alumina and precipitated into 0°C MeOH. The polymer was collected on by vacuum filtration, re-dissolved and re-precipitated in the same manner. The collected polymer was dried by rotary evaporation and high vacuum to resolve a fine white powder.

Synthesis of p(MMA₇₇-b-nBA₁₄₂), Polymer 2

To a 35 mL Schlenk flask, 1.0038 g of Polymer 1 (0.1528 mmol), 7.7650 g nBA (60.62 mmol), 1.0 mL of anisole, 0.1228 g dNbpy (0.303 mmol), 8.5 mL of DPE, and a stir bar were charged and degassed with argon at room temperature for 2.5 hours, resolving a homogeneous solution. CuBr (0.0227 g, 0.151 mmol) was added under positive pressure, and the solution was degassed an additional 20 minutes, resolving a red-brown homogeneous solution. An aliquot was taken for GC and the mixture was submerged in a 90°C bath to initiate polymerization.

At 18 hours, 12 minutes elapsed polymerization time, an aliquot was taken for conversion, and the reaction was quenched by opening to air, cooling to 0°C, and diluting with 20 mL acetone. This solution passed through basic alumina to remove the catalyst and was precipitated into 0°C 9:1 MeOH:H₂O mixture to give an elastic and sticky white polymer. The polymer was collected by decanting, re-dissolved, and re-precipitated again in the same manner. The polymer was collected and dried overnight under vacuum at 80°C to remove residual monomer.

Synthesis of p(MMA₇₇-b-nBA₃₈-co-SPA₄) using dNbpy, Polymer 3

To a 12 mL Schlenk flask, 0.0302 g Polymer 1 (0.0457 mmol), 20981 g nBA (16.37 mmol), 250 µL anisole, 4.0 mL DPE, 0.0377 g dNbpy (0.0909 mmol), 0.7403 g SPA (1.818 mmol), and a stir bar were charged and degassed with stirring for 1.5 hours with argon at room temperature. An aliquot was taken for GC and the polymerization was initiated by submerging in a 90°C bath.

After 18 hours, 10 min elapsed polymerization time, the reaction was quenched by exposing the reaction to air and cooling to 0°C. The polymer solution was dissolved with an equal volume of acetone and precipitated in excess 9:1 MeOH:H₂O mixture. The solvent was

decanted to waste and polymer was collected, dissolved again in acetone and precipitated in excess hexane. The polymer was collected and dried by rotary evaporation and high vacuum overnight, resolving a pink, tough elastomeric polymer.

Synthesis of p(MMA₇₇-b-nBA₅₂-co-SPA₆) using PMDETA, Polymer 4

To a 12 mL Schlenk flask, 0.2988 g Polymer 1, 2.122 g nBA, 250 μ L anisole, 4.0 mL DPE, 0.7436 g SPA, and a stir bar were charged and degassed with argon for 1.5 hours at room temperature. An aliquot was taken for GC conversion and the flask was immersed in a 90°C bath.

After 18 hours, 10 minutes elapsed polymerization time, the reaction was quenched by exposing the mixture to air, cooling to 0°C, and precipitating in 9:1 MeOH: H₂O, giving a purple polymer. The polymer was dried under vacuum briefly to remove solvent, was redissolved in acetone and precipitated once more in hexanes. The polymer was dried at 50°C overnight under high vacuum.

Synthesis of p(Br-MMA₇₅-Br) nb3_p56 macroinitiator, Polymer 5

To a 35 mL Schlenk flask, 10.00 g of MMA (99.88 mmol), 0.342 g DMDBH (0.988 mmol), and 5.0 mL DPE and 1.0 mL of anisole were added with a stir bar and degassed 1.5 hours at 0°C. To a 12 mL Schlenk flask, 5.0 mL DPE and 0.606 g of dNbpy (1.48 mmol) were added and degassed for 1.5 hours in a room temperature bath. After degassing, CuBr (0.1418 g, 0.988 mmol) and CuBr₂ (0.0665 g, 0.297 mmol) were added to the dNbpy solution and degassed for an additional 15 minutes.

An aliquot was taken for GC, and the complexed dNbpy solution was injected into the MMA solution and submerged in a bath at 70°C to initiate polymerization. At 19 hours polymerization (74.1 % conversion), the reaction was quenched by exposing to air, cooling to

0°C, and dissolving in equal volume of 50:50 acetone:THF mixture with warming to approximately 50°C. The warm solution was passed through a plug of neutral alumina and precipitated into 0°C MeOH. The polymer was collected by vacuum filtration, dried under vacuum, redissolved in 50:50 acetone:THF mixture, and re-precipitated in the same manner. The polymer was collected to dry under high vacuum overnight, resolving a fine white powder.

Synthesis of p(Br-nBA₂₆₁-Br) macroinitiator, Polymer 6

To a 35 mL Schlenk flask, 17.88 g of nBA (139.5 mmol), 37.6 µL of PMDETA (0.179 mmol), and a stir bar were added and degassed via 4 freeze-pump-thaw cycles. On the last freeze, 0.0258 g of CuBr (0.179 mmol) was added to the flask. The headspace was evacuated and replaced with nitrogen several times, and the flask was equilibrated at 70°C. An aliquot was taken for GC and 0.0648 (0.179 mmol) BBiBE was added under positive N₂ pressure to initiate the polymerization, and the headspace of the flask was purged for several minutes.

The polymerization was quenched at 15.5 hours (29.1 % conversion) by cooling to 0°C and exposing to the mixture to air. The mixture was diluted with 50 mL THF and passed through 2 plugs of basic alumina. THF and residual monomer were removed by rotary evaporation and high-vacuum, resolving a viscous, green polymer.

Synthesis of p(nBA₃₈₀-b-MMA₁₃₇-co-nBA₁₄) nb2_p41, Polymer 7

To a 35 mL Schlenk flask, 10.0 mL nBA (70.1 mmol), 58.5 µL of PMDETA (0.280 mmol) and 3.5 mL of anisole were added. To a 10 mL Schlenk flask, 1.0 mL nBA (7.01 mmol), 2.0 mL anisole and 20.5 µL of Et₂Br (0.140 mmol) were added, and both flasks were degassed with argon for 1 hour at 0°C. At 45 minutes degassing, CuBr was added into the larger flask and the mixture degassed an additional 15 minutes, developing a light green solution. The large flask was equilibrated at 70°C and the Et₂Br solution was injected via degassed needle to initiate

polymerization. An aliquot was taken immediately after the injection. Aliquots were taken periodically throughout the reaction to monitor conversion.

Separately, a solution of 3.0 mL MEK, 7.46 mL MMA, and 58.5 μ L of PMDETA was degassed at 0°C, 40 minutes. CuCl was thereafter added to the MMA solution as a solid and degassing continued for 20 minutes at room temperature, affording copper dissolution with mild sonication, and stored under inert atmosphere.

At 23 hours, 45 minutes polymerization time, an aliquot was taken to determine conversion of the p(nBA) block, 76.8%, and the degassed MMA solution was injected via syringe and stirred vigorously. The polymerization was quenched by opening to air and cooling to 0°C after 1 hour of chain extension (27.3% conversion) of the MMA monomer. The residual 16.7 mmol of unreacted nBA further polymerized in the second block (12.0% conversion). This mixture was diluted with equal volume of 50:50 acetone:chloroform solution and passed through a basic alumina column to remove the catalyst. The eluent was precipitated into 19:1 MeOH:H₂O solution to resolve a white, gooey precipitate. The polymer was recollected, dissolved, and precipitated once more in the same manner. The polymer was dried overnight under vacuum prior to ¹H NMR, GPC, and AFM analysis.

Synthesis of p(MMA₅₀-co-nBA₄-b-nBA₃₁₀-b- MMA₅₀-co-nBA₄), Polymer 8

To a 15 mL Schlenk flask, 10.0 mL of nBA (70.0 mmol), 73 μ L of PMDETA (0.35 mmol) and 2.0 mL of anisole and a stir bar were added and degassed at 0°C for 1.5 hours with argon. The flask was transferred to a nitrogen Schlenk line and CuBr, 0.050 g (0.35 mmol) was added to the solution and degassing continued for 15 minutes. The flask was equilibrated at 60°C, an aliquot was taken for GC, and 0.080 g of BBiBE was added under positive N₂ pressure to initiate polymerization. A separate solution of 2.355 mL MMA (21.9 mmol), 73 μ L PMDETA

(0.35 mmol), and 0.034 g CuCl (0.35 mmol) were degassed in the same manner and stored under inert atmosphere.

After 9 hours polymerization, the MMA solution was injected via syringe and stirred vigorously. At 12 hours, 15 minutes elapsed polymerization time, the reaction was quenched by exposing to air and cooling to 0°C, resolving a highly viscous dark green mixture. An aliquot was taken for GC and the mixture was dissolved in an equal volume of chloroform and passed through a plug of basic alumina to remove the catalyst. The eluent was precipitated in 0°C 19:1 MeOH:H₂O. The polymer was redissolved and precipitated once more and dried under vacuum for two days to resolve a foamy-white polymer.

Synthesis of p(MMA₂₂-b-nBA₂₆₁-b-MMA₂₂) nb2_p86, Polymer 9

To a 12 mL Schlenk flask, 1.9908 g of Polymer 6 (0.0690 mmol), 6.0 mL of anisole, 108 µL of PMDETA (0.517 mmol), 0.0852 g of aliquot 336, 0.99 mL of MMA (9.187 mmol), and a stir bar were added. This solution was vortexed and stirred for 30 minutes until homogeneous and degassed with argon at 0°C for 30 minutes. CuCl (0.027 g, 0.2596 mmol) was added under positive pressure and the solution degassed for an additional 5 minutes. The mixture was stirred vigorously at room temperature for 10 minutes to resolve a light blue, homogeneous solution. The flask was placed in at 60°C bath to initiated chain extension.

At 19 hours, 20 minutes elapsed polymerization time, the reaction was quenched by exposing to air, cooling to 0°C, and diluting with 50:50 chloroform:acetone mixture. This mixture passed through a plug of basic alumina to remove the catalyst and precipitated into 19:1 MeOH:H₂O to resolve a sticky, very light green polymer.

Synthesis p(MMA_{30-co}-SPMA₁₅-b-nBA₂₆₁-b-MMA_{30-co}-SPMA₁₅), nb2_p88, Polymer 10

To a 12 mL Schlenk flask, 2.0130 g Polymer 6 (0.05905 mmol), 8.0 mL anisole, 108 μ L PMDETA (0.517 mmol), 0.0833 g aliquot 336, 494 μ L MMA (4.64 mmol), and 0.9835 g SPMA (2.339 mmol), and a stir bar were charged, dissolved with stirring, and degassed for 1.5 hours with argon at 0°C. An aliquot was taken for GC, and 26.0 g CuCl (0.263 mmol) was added under positive pressure. Degassing continued an additional 3 minutes to purge the headspace. The flask was stirred vigorously for 5 minutes on a stir plate to dissolve the catalyst, resolving a dark green solution. The flask was placed in a 60°C bath to initiate the polymerization. The solution turned a deep blue shortly after immersing at 60°C.

At 18 hours, 20 minutes elapsed polymerization time, the reaction was quenched by exposing the mixture to air, cooling to 0°C, and addition of 15 mL of 50:50 acetone:chloroform mixture. This solution was precipitated into 0°C MeOH, resolving a deep blue-brown, sticky polymer. The polymer was redissolved twice in 50:50 acetone:chloroform and reprecipitated twice into MeOH, collected by decanting and drying under vacuum at 50°C overnight.

Synthesis p(nBA_{68-co}-SPA₃-b-MMA₇₅-b-nBA_{68-co}-SPA₃), nb3_p73, Polymer 11

To a 12 mL Schlenk flask, 0.4992 g Polymer 5 (0.06380 mmol), 2.5761 g nBA (20.10 mmol), 0.3390 g SPA (0.8294 mmol), 5.0 mL DPE and a stir bar were charged, stirred vigorously, and degassed via 4 freeze-pump-thaw cycles. On the fourth freeze, 0.0038 g CuBr (0.0265 mmol) was added under positive pressure. The headspace was evacuated and refilled with N₂ several times, and an aliquot was taken for GC once thawed. In an 8 mL Schlenk flask, 2.5 mL DPE and 49.5 μ L PMDETA were added and degassed in a room temperature bath for 1 hour. The nBA/SPA solution was equilibrated at 110°C and the PMDETA solution was injected via degassed syringe to initiate polymerization.

At 63 hours, 30 minutes elapsed polymerization time (63.0% conversion), the reaction was quenched by exposing the mixture to air, cooling to 0°C, and diluting with an equal volume of THF. The polymer solution was precipitated into 0°C ethanol, resolving a pink semi-solid polymer. The polymer was redissolved in THF and precipitated once more in cold ethanol, collected by decanting solvent to waste, and drying under high vacuum for a few days.

Synthesis p(nBA-co-SPA), Polymer 12

To a 12 mL Schlenk flask, 3.46 mL nBA, 0.400 g SP, 70 μ L Et₂Br, 65 μ L PMDETA, 346 μ L DMF, and a stir bar were added and the solution degassed 1 hour. The flask was submerged in a 90°C bath for 18 hours. The reaction was quenched by exposing to air and cooling to 0°C. 6 mL THF was added to the mixture and passed through a plug of alumina to remove the catalyst. The residue was condensed down to a red sticky solid under high vacuum, redissolved in DCM and loaded onto a column with 8:2 hexane:EtOAc as eluent. The SPA monomer was eluted first ($R_f = 0.2$), and once monomer removed the column was flushed with acetone to collect the polymer.

Synthesis p(MMA-co-SPMA), Polymer 13

To a 12-mL Schlenk flask, 0.8202 g MMA, 0.380 g SPMA, 4.0 mL THF, 93.5 μ L Me₆TREN, 100 μ L toluene, and a stir bar were added. To a small vial, 1.0 mL THF and 0.0053 mL Et₂Br was added. Both solutions degassed at 0°C for 1 hour, after which 0.0052g CuBr was added to the MMA solution. Degassing continued 5 minutes, and the bath was placed in a 65°C bath. An aliquot was taken immediately for GC, and the Et₂Br solution was injected via degassed syringe.

At 24 hours 11 minutes polymerization, the reaction was quenched by exposing to air, cooling to 0°C, and an aliquot was taken for GC conversion. The polymer was precipitated twice

into 90:10 MeOH:H₂O from THF to give a light pink polymer. The polymer was collected with vacuum filtration and dried under high vacuum.

References

1. Ronca, G.; Russell, T. P. *Macromolecules* **1985**, 18, 665-670.
2. Gopishetty, V.; Tokarev, I.; Minko, S. *Journal of Materials Chemistry* **2012**, 22, 19482-19487.
3. Huck, W. T. S. *Chemical Communications* **2005**, 4143-4148.
4. Fries, K. H.; Driskell, J. D.; Samanta, S.; Locklin, J. *Anal. Chem.* **2010**, 82, 3306-3314.
5. Fries, K. H.; Driskell, J. D.; Sheppard, G. R.; Locklin, J. *Langmuir* **2011**, 27, 12253-12260.
6. Fries, K.; Samanta, S.; Orski, S.; Locklin, J. *Chemical Communications* **2008**, 6288-6290.
7. Hansen, C., M., *Hansen Solubility Parameters: A User's Handbook*. CRC Press LLC: Boca Raton, London, New York, Washington D.C., 2000.
8. Albrecht, U.; Schäfer, H.; Richert, R. *Chem. Phys.* **1994**, 182, 61-68.
9. Nolan, E. M.; Lippard, S. J. *Chem. Rev.* **2008**, 108, 3443-3480.
10. Prodi, L.; Bolletta, F.; Montalti, M.; Zaccheroni, N. *Coordination Chemistry Reviews* **2000**, 205, 59-83.
11. Kavitha, A. A.; Singha, N. K. *Macromolecules* **2010**, 43, 3193-3205.
12. Borea, G.; Cignarella, S. *Il Farmaco* **2000**, 55.

CHAPTER 3

ADVANCES IN SMART MATERIALS: STIMULI-RESPONSIVE HYDROGEL THIN FILMS

¹ White, E. M.; Yatvin, J.; Grubbs, J. B.; Bilbrey, J. A.; Locklin, J, Reprinted with permission from *Journal of Polymer Science Part B: Polymer Physics* **2013**, 51, 1084-1099. Copyright 2013 Wiley Periodicals, Inc..

Abstract

This review highlights recent developments in the field of stimuli-responsive spiropyran and other light responsive hydrogels, focusing primarily on thin films, with a thickness range between 100 nm to 10 μm . The theory and dynamics of hydrogel swelling is reviewed, followed by specific applications. Gels are classified based on the active stimulus and fabrication methods, design constraints, and novel stimuli-responses are discussed. Often, these materials display large physiochemical reactions to a relatively small stimulus. Noteworthy materials larger than 10 μm , but with response times on the order of seconds to minutes are also discussed. Hydrogels have the potential to advance the fields of medicine and polymer science as useful substrates for “smart” devices and the Flory and Rehner theory to hydrogel behavior is addressed.

Introduction

Hydrogels are used regularly in daily life and are found in consumer products such as shampoos and toothpaste, cleaners, cell cultures substrates, wound dressings, and drug delivery devices. However, advances in stimuli-responsive hydrogel materials may offer methods to make these materials more intelligent in design or purpose. Hydrogels are prevalent in nature as an excellent support scaffold for an immense diversity of life on Earth, with cells as the chief example.²⁻⁸ Following nature’s successful model, a wide array of research, from tissue cultures to nano-size actuators,⁹ has demonstrated the diverse assortment of physical properties attributed to these materials.

Hydrogels have become a popular platform for the fabrication of smart devices because of their overall biocompatibility, high storage capacity for cells and small molecules, and low interfacial tension at the gel-aqueous solution interface.¹⁰ Hydrogels respond to a large range of

stimuli and offer a medium where spatially-immobilized chemical functionalities may be manipulated under aqueous conditions. Several review articles have been dedicated to the application of stimuli-responsive hydrogels.¹¹⁻¹⁴ For example, previous work by Tokarev and Minko outlined burgeoning technologies, addressing a wide range of interesting applications of responsive hydrogel thin films,¹⁰ while Buengera et al. summarized the use of hydrogels as stimuli-responsive sensors.¹⁵

This review includes a survey of noteworthy advances in thin film hydrogels, ranging from approximately 100 nm to 10 μm , developed in the past five years, and is not meant to be an exhaustive review of hydrogel technology. Thin films find commercial use today in familiar products such as paints, stains, surface cleaners, mirrors, electroplated metals, to name a few. Recent advancements in organic thin films may help improve performance and reduce future production costs and the amount of materials used for a variety of existing technologies including photovoltaics, sensors, membrane technology, and drug delivery systems. Herein, we have classified the gels based on the stimulus response (i.e. *light-responsive* hydrogels); therefore, this review outlines the general theory of hydrogels, followed by a discussion of how these materials respond to the various stimuli: mechanical, chemical, pH, heat, and light.

Theory of Swelling

Typically, hydrogels are three-dimensional networks of either chemically or physically cross-linked polymers that swell upon the addition of water. The ratio of the swollen volume to the dry volume of the polymer matrix is often referred to as the *degree of swelling*, and is a common parameter for describing many hydrogels.¹⁰ The degree of swelling of poly[acrylamide-*stat*-(acrylic acid)] hydrogels, for example, may be as high as 20,000, which indicates a

volumetric expansion greater than four orders of magnitude.¹⁶ The degree of swelling is dependent on polymer composition and architecture, as well as inherent properties of the aqueous solution such as temperature or ionic strength.

Equilibrium Swelling Theory

The equilibrium swelling theory of neutral, isotropic polymer networks in the presence of small molecules was first described by Flory and Rehner.¹⁷ The Flory-Rehner model was proposed for the structure of a cross-linked polymer network immersed in a good solvent where the free energy of mixing from osmotic pressure induces solvent migration into the network. The model assumes both a Gaussian distribution of polymer chain lengths and average cross-links to be tetrafunctional. The theory considers forces arising from three sources:

- 1) the entropy change associated with mixing of polymer and solvent
- 2) the entropy change arising from reduced polymer conformations upon swelling
- 3) the enthalpy of mixing the polymer and solvent¹⁶

The entropy change from polymer-solvent mixing is positive and favors swelling, while the entropy change from chain stretching (reduction of the number of possible conformations) is negative and opposes swelling. The enthalpy of mixing, which is dependent on the gel composition, can be either positive (opposing mixing), negative (favoring mixing), or zero. Swelling of the gel is a function of elastic retractive forces of the polymer chains and the expansive thermodynamic contribution of mixing of polymer and solvent. From this, the free energy of a neutral hydrogel in the absence of charged species can be expressed as:

$$\Delta G = \Delta G_{el} + \Delta G_{mix} \quad \text{(Equation 3.1)}$$

where ΔG_{el} is the free energy of elastic retractive forces and ΔG_{mix} is the free energy of polymer and solvent mixing. The term ΔG_{mix} is a measure of the compatibility of the polymer with the surrounding solvent molecules.¹⁸ At equilibrium conditions, the net chemical potential (μ) must equal zero:

$$\mu = \mu_{el} + \mu_{mix} = 0 \quad \text{(Equation 3.2)}$$

Therefore, any changes in the chemical potential due to mixing (μ_{mix}) are balanced by elastic retractive forces (μ_{el}) of the network. The change in chemical potential due to such forces can be expressed by the theory of rubber elasticity proposed by Edwards.¹⁹

Polymer Volume Fraction

Among the many parameters used to characterize hydrogels, the polymer volume fraction in the swollen state ($v_{2,s}$), the molecular weight of the polymer chain between cross-links (\bar{M}_c), and the mesh size of the gel (ξ) are among the most informative, especially for drug delivery applications (Figure 3.1).¹⁸ These three parameters can be determined using the equilibrium swelling theory of rubber elasticity modified by Flory.²⁰

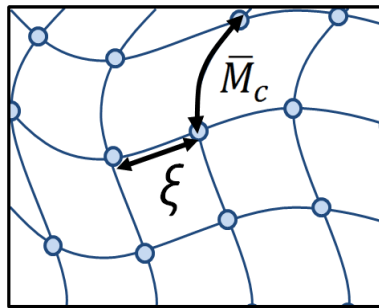


Figure 3.1. Schematic representation of a polymeric hydrogel. The molecular weight of the polymer chain between cross-links (\bar{M}_c), and the mesh size of the gel (ξ) are represented.

The swollen state polymer volume fraction $v_{2,s}$ (analogous to the *degree of swelling*) is the ratio of the polymer volume (V_p) to the swollen gel volume (V_g). These terms are related to the

volumetric swollen ratio (Q), which is dependent on the densities of the solvent (ρ_1) and polymer (ρ_2), and the mass swollen ratio (Q_m) as in the following equation:²¹

$$v_{2,s} = \frac{V_p}{V_g} = Q^{-1} = \frac{1}{\frac{\rho_2}{\rho_1} + 1} \quad (\text{Equation 3.3})$$

The architecture of a swollen hydrogel can be quantified by the molecular weight between cross-links in the absence of solvent and is expressed by:²²

$$\frac{1}{\bar{M}_c} = \frac{2}{\bar{M}_N} - \frac{\left(\frac{\bar{v}}{v_1}\right)[\ln(1-v_{2,s})+v_{2,s}+\chi_1 v_{2,s}^2]}{(v_{2,s})^{\frac{1}{3}} - \left(\frac{v_{2,s}}{2}\right)} \quad (\text{Equation 3.4})$$

where \bar{M}_N is the number average molecular weight of the polymer chains prepared in the absence of cross-linkers. \bar{v} and V_1 are the specific and molar volume of polymer and solvent, respectively. $v_{2,s}$ is the volume fraction of polymer in the swollen mass, and χ_1 is the Flory-Huggins polymer-solvent dimensionless interaction term.

Equation 3.4 describes gels that are swollen from the dry state; however, many gels are prepared in the presence of water. A new term was introduced by Peppas and Merrill to account for the presence of water and subsequent changes in chemical potential, which describes the volume fraction density of the chains during cross-linking.²² The original Flory-Rehner model was revised to incorporate a term describing the polymer in the relaxed, unstretched state ($v_{2,r}$):

$$\frac{1}{\bar{M}_c} = \frac{2}{\bar{M}_N} - \frac{\left(\frac{\bar{v}}{v_1}\right)[\ln(1-v_{2,s})+v_{2,s}+\chi_1 v_{2,s}^2]}{v_{2,r} \left[\left(\frac{v_{2,s}}{v_{2,r}}\right)^{\frac{1}{3}} - \left(\frac{v_{2,s}}{2v_{2,r}}\right) \right]} \quad (\text{Equation 3.5})$$

When ionic groups are present in the network, the swelling equilibrium becomes more complicated. In addition to the entropic contributions described in Equation 3.1, a contribution from ions to the total change in Gibbs free energy is:

$$\Delta G = \Delta G_{el} + \Delta G_{mix} + \Delta G_{ion} \quad (\text{Equation 3.6})$$

At equilibrium, the net chemical potential still equals zero, and expressions for the ionic contribution to this potential are added to Equation 5. Terms for the ionic strength, I , and the dissociation constants K_a and K_b have been added to account for the strong dependency on the ionic strength of the surrounding medium and the nature of these ions.²³⁻²⁵

$$\frac{V_1}{4I} \left(\frac{v_{2,s}^2}{\bar{v}} \right) \left(\frac{K_a}{10^{-pH} - K_a} \right)^2 =$$

$$\left[\ln(1 - v_{2,s}) + v_{2,s} + \chi_1 v_{2,s}^2 \right] + \left(\frac{V_1}{\bar{v} \bar{M}_c} \right) \left(1 - \frac{2\bar{M}_c}{\bar{M}_n} \right) v_{2,r} \left[\left(\frac{v_{2,s}}{v_{2,r}} \right)^{1/3} - \left(\frac{v_{2,s}}{v_{2,r}} \right) \right]$$

(Equation 3.7)

$$\frac{V_1}{4I} \left(\frac{v_{2,s}^2}{\bar{v}} \right) \left(\frac{K_b}{10^{-pH-14} - K_b} \right)^2 =$$

$$\left[\ln(1 - v_{2,s}) + v_{2,s} + \chi_1 v_{2,s}^2 \right] + \left(\frac{V_1}{\bar{v} \bar{M}_c} \right) \left(1 - \frac{2\bar{M}_c}{\bar{M}_n} \right) v_{2,r} \left[\left(\frac{v_{2,s}}{v_{2,r}} \right)^{1/3} - \left(\frac{v_{2,s}}{v_{2,r}} \right) \right]$$

(Equation 3.8)

For polyelectrolyte gels, Equations 3.7 and 3.8 are equivalent expressions for anionic and cationic hydrogels prepared in the presence of a solvent. Artificially engineered protein-based hydrogels present a challenge in polymer physics; however, work by Kim et al. reviews some of the progress on the physics of the dynamic intermolecular interactions of protein hydrogels.²⁶

Dynamic Swelling of Hydrogels

The theories described above address the equilibrium swelling state of hydrogels; however, an understanding of the swelling dynamics through volume phase transitions may be useful for predicting the hydrogel behavior with time. There are many various models that simulate volume transition reviewed in earlier work by Wu et al.²⁷ and Saunders et al.²⁸ Recently, work by Li et al.²⁹ and Lai et al.³⁰ investigated the swelling dynamics of hydrogels by the multi-effect-coupling

ionic-strength-stimulus model (MECis), which integrates the Nernst–Planck equation for mobile ion concentrations, the Poisson equation for the electric potential associated with the fixed charges, and equations to describe the mechanical displacement of a deformable network and the phase field variable. The MECis model is designed to study hydrogels stimulated by changes in ionic strength in two dimensions.

Both linear and nonlinear theories have been developed to describe the swelling kinetics and the processes of mass transport and mechanical deformation. Tanaka et al. derived a linear diffusion equation for polyacrylamide gels treated as a mixture of solid and liquid.^{31, 32} A second linear theory by Scherer treats the gel as a continuum phase with pore pressure as a state variable.^{33, 34} Recent work by Yoon et al. examines experimental swelling kinetics of thin layers of poly(*N*-isopropylacrylamide) with the model of linear poroelasticity.³⁵ Through fluorescent particle tracking with a microscope, these experiments were able to accurately monitor thickness changes on the order of 100 μm in good agreement with a linear model of poroelasticity. The linear theory works well for small deformations; however, Hong et al. formulated a nonlinear theory for coupled mass transport and large deformations on the macroscopic scale.³⁶ Recent work by Bouklas et al. presents a good comparison between the linear theory and the more recent nonlinear theory of poroelasticity for polymer gels.³⁷ In this work, the dynamics of swelling of a gel affixed to a substrate as well as free swelling are both addressed.

Calculation of the Mesh Size

Many of the target applications for the stimuli-responsive gels outlined in this review are for drug delivery, where mesh size, sometimes referred to as the ‘pore’ size, becomes important. The

mesh size is described by the correlation length (ξ) which is defined as the linear distance between two adjacent cross-links (Figure 1) and is calculated by:

$$\xi = \alpha(\bar{r}_0^2)^{1/2} \quad (\text{Equation 3.9})$$

where α is the elongation ratio of the polymer chains in any direction and $(\bar{r}_0^2)^{1/2}$ is the root-mean-squared, unperturbed end-to-end distance of the polymer chain between cross-links.^{18,38}

For gels swollen to isotropic equilibrium, the elongation ratio can be related to the swollen polymer volume fraction, $v_{2,s}$, by:

$$\alpha = v_{2,s}^{-1/3} \quad (\text{Equation 3.10})$$

The end-to-end distance of network chains between two adjacent cross-links in the unperturbed state may be determined from the Flory characteristic ratio, C_N , the length of the bond along the backbone, l (1.54 Å for vinylic polymers), and the number of links per chain, N , calculated by Equations 3.11 and 3.12.

$$(\bar{r}_0^2)^{1/2} = l(C_N N)^{1/2} \quad (\text{Equation 3.11})$$

$$N = \frac{2\bar{M}_c}{\bar{M}_r} \quad (\text{Equation 3.12})$$

where \bar{M}_r is the molecular weight of the polymer repeat unit. By combination of Equations 3.9 – 12, the end-to-end distance and pore size of an isotropically swollen hydrogel can be calculated by:

$$\xi = v_{2,s}^{-1/3} \left(\frac{2C_N \bar{M}_c}{\bar{M}_r} \right)^{1/2} l \quad (\text{Equation 3.13})$$

Swelling, and therefore mesh size, is affected by numerous physiochemical conditions and structural factors.³⁹⁻⁴³ Many ionic hydrogels exhibit a first-order volume-phase transition where the degree of swelling can change dramatically with only a small change in conditions or application of a stimulus (Figure 3.2).¹⁶

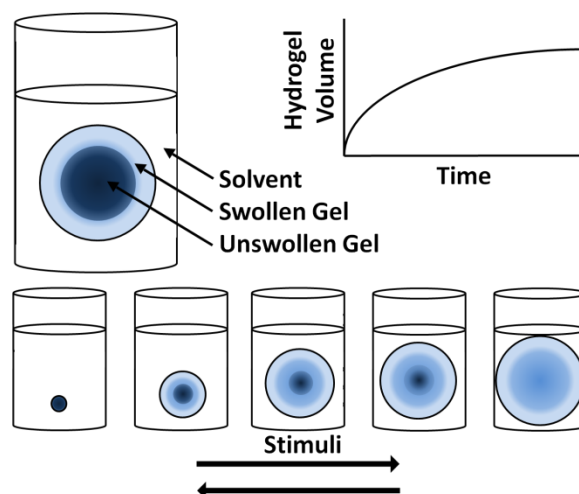


Figure 3.2. The first-order volumetric swelling response of hydrogels with respect to time.

The swelling transition has a first-order response that involves the coexistence of two gel phases, the swollen and unswollen volume components. Polyelectrolyte gels often swell to a significantly greater extent when compared to neutral gels because of the additional osmotic pressure arising from mobile counter-ions, as well as the electrostatic repulsion of anchored ionizable groups.¹⁰ Charged particles inside the gel fail to distribute evenly between the inside of the gel and the outside medium. This difference in mobile ion concentrations between the gel and the surrounding solution causes the gel to swell to a greater extent and is governed by the Donnan equilibrium.⁴⁴ For highly ionized polyelectrolyte gels, Donnan theory was modified by Rička and Tanaka to include an osmotic pressure ion contribution term to better approximate volume transitions due to the additional equilibrium swelling pressure.²⁵ As a result, modifications of these theories have emerged to describe hydrogel swelling behaviors.^{23, 45-47} Long-range repulsive electrostatic interactions between the polyelectrolyte segments favor swelling, while attractive electrostatic interactions between counter-ions and charged polymer segments favor shrinking. Counter-ion condensation leads to anisotropic charge distribution and

the formation of ion pairs. The non-Gaussian conformation of charged polymer segments, Debye screening contributions, and other gel responses are also described.²⁰⁻²²

In the interest of practicality, fast response action is required for most stimuli-responsive thin-film devices. The volume phase transition response is the most common mechanism among hydrogel-based “smart” devices. This transition is driven by a diffusion limited process; therefore, at least one dimension of the hydrogel must be sufficiently small so that the response behavior occurs on the order of seconds to minutes. Early work by Tanaka and Fillmore shows the volumetric response time of a gel is proportional both to the square of the smallest linear dimension of a gel and to the diffusion coefficient of the gel network, D ,³¹ which governs response time by:

$$D = \frac{E}{f} \quad \text{(Equation 3.14)}$$

where E is the longitudinal bulk modulus of the network, and f is the coefficient of friction between the network and the solvent.³¹ Stimuli-responsive materials that respond on the order of seconds are typically 10 μm or less in their smallest linear dimension, reducing the physical restrictions to response time. This is not a strict geometric limitation; however, noteworthy examples of gels with a larger dimension, but second to minute response times, are also highlighted. Furthermore, not all of the stimuli-responsive devices outlined in this review are governed by diffusion limited processes.

Light Stimulus

Spatial, wavelength, and intensity parameters of light can be varied quickly, easily, and remotely, enabling light to be one of the most controllable stimuli. Research has taken advantage of this unique control to synthesize gels that use the fine spatial and time resolution afforded by

photo-irradiation. In the context of hydrogels, light is most often used to induce cross-linking, which can be used to produce novel results, such as in the aforementioned work by Hayward.⁴⁸ In terms of responses, light can stimulate a variety of useful responses, such as cleavage of cross-links, diffraction shifts in the presence of analytes, biomolecule and nanoparticle uptake and release, and ion detection.⁴⁹⁻⁵⁴

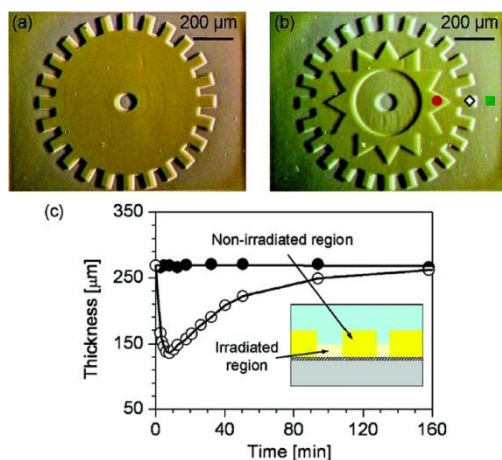


Figure 3.3. Spiropyran hydrogel micro-relief patterning. (a, b) Images of the pSPNIPAAm hydrogel layer just after the micro patterned light irradiation. Duration of irradiation was (●, red) 0 seconds, (◇) 1 second, and (○, green) 3 seconds. (c) Height change of the hydrogel layer in (b) non-irradiated and (O) irradiated region as a function of time after 3 seconds blue light irradiation. Reprinted with permission from *Chem. Mater.* **2007**, *19*, 2730-2732. Copyright 2007 American Chemical Society.

The Kanamori group has used the high spatial-resolution of light to form microscopic surface motifs on poly(*N*-isopropylacrylamide-co-acrylospiropyran) films with *N,N*-methylenebis(acrylamide) included as a cross-linker.⁵⁵ Acidifying the gel in the dark can induce ring opening into the protonated merocyanine isomer. After exciting the acidified gel with 436 nm light, micromotifs could be created from the decrease in swelling caused by the switching of

merocyanine in irradiated domains to the ring-closed hydrophobic spiropyran isomer (Figure 3.3). Depending on irradiation time (1 – 3 sec), motifs were formed which varied in height up to 130 μm . The pattern completely faded after 3 hours in the dark, and a new one could be installed on the same gel.

Photodegradable cross-links are critical tools for designing responsive gels. Pioneering work by the Anseth group,⁴⁹ using acrylates connected by a nitrobenzyl ether photodegradable moiety to PEG cross-links, has opened new avenues of research. Degrading the cross-links uniformly can alter the overall material properties; however, local photoirradiation with either a single photo 405 nm laser or a two photon 740 nm laser can form 3D structures in the material. Anseth's work focused on creating a unique and tunable cell culture environment, but broader work in this area promises powerful new applications.

The *cis-trans* isomerization photoresponse of azobenzene is commonly used in photoresponsive materials.⁵⁶⁻⁵⁸ Liu et al. examined the release kinetics, poration, and swelling kinetics of a gel containing azobenzene.⁵⁹ It was shown that the *cis* conformation allows widening of the pores to release of trapped water from a hydrogel.

Another adaption of this azobenzene chemistry was shown by the Tieke group with copolymerization of pNIPAM and (11-(acryloyloxy)undecyl)trimethylammonium bromide gel using gamma radiation.⁶⁰ The gel was swelled with an aqueous disodium 4,4'-di(6-sulfatohexyloxy)azobenzene solution, which is electrostatically adsorbed onto the polymer matrix. Below the LCST the azo group freely isomerizes in response to light, but above the LCST the azo group cannot interconvert between isomers, likely due to the steric hindrance of a shrunken gel and the loss of optical clarity after the LCST transition. Using temperature to trap gel properties allows the building of smarter and more complex systems.

Future Outlook for Hydrogels

This review outlines recent progress in the field of stimuli-responsive hydrogels. As these films improve through creative new designs, their influence is likely to expand to new areas of science, industry, and health. The rapid expansion of this field has created novel devices that stretch across disciplines including polymer science, biochemistry, tissue engineering, and medicine.^{2, 61-71} Although developing hydrogel systems that respond quickly to external stimuli is a challenge, films that have a fast, easily observable response to minimal stimuli have undergone tremendous improvement. Furthermore, developing a single system that can respond to multiple stimuli is often challenging and requires precise molecular engineering,^{56, 72-75} although some examples of multiple-response materials promise unforeseen applications.^{56, 76-82}

In living systems, nature exploits the principle of partitioning: compartmentalized cells are separated by biochemically selective membranes which interact dynamically with their surrounding environment.⁸³ Imitating this type of hierarchal organization of complex stimuli-responses will help aid in the development of increasingly more utilitarian stimuli-response materials.

Future advances in porous membrane fabricated from hydrogels may one day provide angstrom-precise selectivity to molecule passivity. Photonic hydrogels may offer a scaffold for the development of flexible, liquid-like, color displays. The controlled stimulus, sol-gel transitions of hydrogel materials may lead to advanced biodegradable products to be used commercially. Future electricity-free biomolecule sensors constructed from hydrogels may come packaged as dry state devices, activated with the addition of water. Hydrogels present a useful substrate for functional, stimuli-responsive devices, and many more applications for these devices will develop as the technology for intelligent, stimuli-responsive materials improves.

References

1. White, E. M.; Yatvin, J.; Grubbs, J. B.; Bilbrey, J. A.; Locklin, J. *Journal of Polymer Science Part B: Polymer Physics* **2013**, 51, 1084-1099.
2. Discher, D. E.; Mooney, D. J.; Zandstra, P. W. *Science* **2009**, 324, 1673-1677.
3. Schade, R.; Weiss, T.; Berg, A.; Schnabelrauch, M.; Liefelth, K. *The International Journal Of Artificial Organs* **2010**, 33, 219-227.
4. Geckil, H.; Xu, F.; Zhang, X.; Moon, S.; Demirci, U. *Nanomedicine* **2010**, 5, 469-484.
5. Kuo, Y.-C.; Chang, Y.-H. *Colloids and Surfaces B: Biointerfaces* **2013**, 102, 405-411.
6. Lee, K. Y.; Mooney, D. J. *Chem. Rev.* **2001**, 101, 1869-1880.
7. Li, X.; Katsanevakis, E.; Liu, X.; Zhang, N.; Wen, X. *Prog. Polym. Sci.* **2012**, 37, 1105-1129.
8. Tibbitt, M. W.; Anseth, K. S. *Biotechnology and Bioengineering* **2009**, 103, 655-663.
9. Sidorenko, A.; Krupenkin, T.; Aizenberg, J. *Journal of Materials Chemistry* **2008**, 18, 3841-3846.
10. Tokarev, I.; Minko, S. *Soft Matter* **2009**, 5, 511-524.
11. Tokarev, I.; Minko, S. *Advanced Materials* **2010**, 22, 3446-3462.
12. Piepenbrock, M.-O. M.; Lloyd, G. O.; Clarke, N.; Steed, J. W. *Chem. Rev.* **2009**, 110, 1960-2004.
13. Van Vlierberghe, S.; Dubruel, P.; Schacht, E. *Biomacromolecules* **2011**, 12, 1387-1408.
14. Kloxin, C. J.; Scott, T. F.; Adzima, B. J.; Bowman, C. N. *Macromolecules* **2010**, 43, 2643-2653.
15. Buenger, D.; Topuz, F.; Groll, J. *Prog. Polym. Sci.* **2012**, 37, 1678-1719.

16. Sperling, L. H., *Introduction to Polymer Science*. Fourth Edition ed.; John Wiley & Sons Inc.: Hoboken, New jersey, 2006.
17. Flory, P. J.; John Rehner, J. *J. Chem. Phys.* **1943**, 11, 521-526.
18. Peppas, N. A.; Bures, P.; Leobandung, W.; Ichikawa, H. *Eur. J. Pharm. Biopharm.* **2000**, 50, 27-46.
19. SF., E. *Br. Polymer J.* **1977**, 9, 140-143.
20. Flory, P. J. *Polymer* **1979**, 20, 1317-1320.
21. Lin, C.-C.; Metters, A. T. *Adv. Drug Delivery Rev.* **2006**, 58, 1379-1408.
22. Peppas, N. A. M., Edward W. *J. Appl. Polym. Sci.* **1977**, 21, 1763-1770.
23. Katchalsky, A.; Michaeli, I. *J. Polym. Sci.* **1955**, 15, 69-86.
24. Brannon-Peppas, L.; Peppas, N. A. *Chem. Eng. Sci.* **1991**, 46, 715-722.
25. Rička, J.; Tanaka, T. *Macromolecules* **1984**, 17, 2916-2921.
26. Kim, M.; Tang, S.; Olsen, B. D. *Journal of Polymer Science Part B: Polymer Physics* **2013**, 51, 587-601.
27. Wu, S.; Li, H.; Chen, J. P.; Lam, K. Y. *Macromolecular Theory and Simulations* **2004**, 13, 13-29.
28. Saunders, J. R.; Abu-Salih, S.; Khaleque, T.; Hanula, S.; Moussa, W. *Journal of Computational and Theoretical Nanoscience* **2008**, 5, 1942-1960.
29. Li, D.; Yang, H.; Emmerich, H. *Colloid and Polymer Science* **2011**, 289, 513-521.
30. Lai, F.; Li, H. *Soft Matter* **2010**, 6, 311-320.
31. Tanaka, T.; Fillmore, D. J. *J. Chem. Phys.* **1979**, 70, 1214-1218.
32. Tanaka, T.; Hocker, L. O.; Benedek, G. B. *J. Chem. Phys.* **1973**, 59, 5151-5159.
33. Scherer, G. W. *Journal of Non-Crystalline Solids* **1989**, 113, 107-118.

34. Scherer, G. W. *Journal of Non-Crystalline Solids* **1992**, 144, 210-216.
35. Yoon, J.; Cai, S.; Suo, Z.; Hayward, R. C. *Soft Matter* **2010**, 6, 6004-6012.
36. Hong, W.; Zhao, X.; Zhou, J.; Suo, Z. *Journal of the Mechanics and Physics of Solids* **2008**, 56, 1779-1793.
37. Bouklas, N.; Huang, R. *Soft Matter* **2012**, 8, 8194-8203.
38. Canal, T. P., Nikolaos A. *J. Biomed. Mater. Res. Part B* **1989**, 23, 1183-1193.
39. Pourjavadi, A.; Salimi, H. *J. Ind. Eng. Chem.* **2008**, 47, 9206-9213.
40. Swann, J. M. G.; Bras, W.; Topham, P. D.; Howse, J. R.; Ryan, A. J. *Langmuir* **2010**, 26, 10191-10197.
41. Gao, M.; Gawel, K.; Stokke, B. T. *Soft Matter* **2011**, 7, 1741-1746.
42. Donati, I.; Mørch, Y. A.; Strand, B. L.; Skjåk-Bræk, G.; Paoletti, S. *J. Phys. Chem. B* **2009**, 113, 12916-12922.
43. Kudaibergenov, S. E.; Sigitov, V. B. *Langmuir* **1999**, 15, 4230-4235.
44. Donnan, F. G. *Z. Elektrochem. Angew. P.* **1912**, 17.
45. Katchalsky; Lifson, S.; Eisenberg, H. *J. Polym. Sci.* **1951**, 7, 571-574.
46. Khokhlov, A. R.; Starodubtzev, S. G.; Vasilevskaya, V. V., *Advances in Polymer Science: Responsive Gels: Volume Transitions*. I ed.; Springer: Verlag, Berlin, 1993; Vol. 109.
47. Mayer, S. W. *J. Am. Chem. Soc.* **1950**, 72, 2292-2293.
48. Kim, J.; Hanna, J. A.; Byun, M.; Santangelo, C. D.; Hayward, R. C. *Science* **2012**, 335, 1201-1205.
49. Kloxin, A. M.; Kasko, A. M.; Salinas, C. N.; Anseth, K. S. *Science* **2009**, 324, 59-63.
50. Klinger, D.; Landfester, K. *Macromolecules* **2011**, 44, 9758-9772.

51. Holtz, J. H.; Asher, S. A. *Nature* **1997**, 389, 829-832.
52. Gong, C.; Wong, K.-L.; Lam, M. H. W. *Chem. Mater.* **2008**, 20, 1353-1358.
53. Yan, B.; Boyer, J.-C.; Habault, D.; Branda, N. R.; Zhao, Y. *J. Am. Chem. Soc.* **2012**, 134, 16558-16561.
54. Dave, N.; Chan, M. Y.; Huang, P.-J. J.; Smith, B. D.; Liu, J. *J. Am. Chem. Soc.* **2010**, 132, 12668-12673.
55. Szilágyi, A.; Sumaru, K.; Sugiura, S.; Takagi, T.; Shinbo, T.; Zrínyi, M.; Kanamori, T. *Chem. Mater.* **2007**, 19, 2730-2732.
56. Liu, J.; Chen, G.; Guo, M.; Jiang, M. *Macromolecules* **2010**, 43, 8086-8093.
57. Zhao, Y.-L.; Stoddart, J. F. *Langmuir* **2009**, 25, 8442-8446.
58. Kamenjicki, M.; Asher, S. A. *Macromolecules* **2004**, 37, 8293-8296.
59. Liu, J.; Nie, J.; Zhao, Y.; He, Y. *Journal of Photochemistry and Photobiology A: Chemistry* **2010**, 211, 20-25.
60. Friedrich, T.; Mielke, T.; Domogalla, M.; Hentschel, M.; Kraus, K.; Tieke, B. *Macromol. Rapid Commun.* **2013**, 34, 393-398.
61. Nettles, D. L.; Chilkoti, A.; Setton, L. A. *Adv. Drug Delivery Rev.* **2010**, 62, 1479-1485.
62. Abu Hashim, I. I.; Higashi, T.; Anno, T.; Motoyama, K.; Abd-ElGawad, A.-E. H.; El-Shabouri, M. H.; Borg, T. M.; Arima, H. *International Journal of Pharmaceutics* **2010**, 392, 83-91.
63. Casuso, P.; Carrasco, P.; Loinaz, I.; Grande, H. J.; Odriozola, I. *Organic & Biomolecular Chemistry* **2010**, 8, 5455-5458.
64. Zhang, X.; Huang, J.; Chang, P. R.; Li, J.; Chen, Y.; Wang, D.; Yu, J.; Chen, J. *Polymer* **2010**, 51, 4398-4407.

65. Li, J. *NPG Asia Mater* **2010**, 2, 112-118.
66. Li, X.; Li, J.; Gao, Y.; Kuang, Y.; Shi, J.; Xu, B. *J. Am. Chem. Soc.* **2010**, 132, 17707-17709.
67. Liang, G.; Yang, Z.; Zhang, R.; Li, L.; Fan, Y.; Kuang, Y.; Gao, Y.; Wang, T.; Lu, W. W.; Xu, B. *Langmuir* **2009**, 25, 8419-8422.
68. Liu, K. L.; Zhang, Z.; Li, J. *Soft Matter* **2011**, 7, 11290-11297.
69. Naskar, J.; Palui, G.; Banerjee, A. *J. Phys. Chem. B* **2009**, 113, 11787-11792.
70. Rodriguez-Llansola, F.; Miravet, J. F.; Escuder, B. *Chemical Communications* **2011**, 47, 4706-4708.
71. Zhu, W.; Li, Y.; Liu, L.; Chen, Y.; Wang, C.; Xi, F. *Biomacromolecules* **2010**, 11, 3086-3092.
72. Dou, C.; Li, D.; Gao, H.; Wang, C.; Zhang, H.; Wang, Y. *Langmuir* **2009**, 26, 2113-2118.
73. Liu, J.-W.; Yang, Y.; Chen, C.-F.; Ma, J.-T. *Langmuir* **2010**, 26, 9040-9044.
74. Wang, Y.; Zhan, C.; Fu, H.; Li, X.; Sheng, X.; Zhao, Y.; Xiao, D.; Ma, Y.; Ma, J. S.; Yao, J. *Langmuir* **2008**, 24, 7635-7638.
75. Liu, Z.-X.; Feng, Y.; Yan, Z.-C.; He, Y.-M.; Liu, C.-Y.; Fan, Q.-H. *Chem. Mater.* **2012**, 24, 3751-3757.
76. Adhikari, B.; Nanda, J.; Banerjee, A. *Soft Matter* **2011**, 7, 8913-8922.
77. Appel, E. A.; Loh, X. J.; Jones, S. T.; Biedermann, F.; Dreiss, C. A.; Scherman, O. A. *J. Am. Chem. Soc.* **2012**, 134, 11767-11773.
78. Chen, Y.; Pang, X.-H.; Dong, C.-M. *Advanced Functional Materials* **2010**, 20, 579-586.
79. Dong, S.; Luo, Y.; Yan, X.; Zheng, B.; Ding, X.; Yu, Y.; Ma, Z.; Zhao, Q.; Huang, F. *Angewandte Chemie* **2011**, 123, 1945-1949.

80. Pasparakis, G.; Vamvakaki, M. *Polymer Chemistry* **2011**, 2, 1234-1248.
81. Ren, L.; He, L.; Sun, T.; Dong, X.; Chen, Y.; Huang, J.; Wang, C. *Macromolecular Bioscience* **2009**, 9, 902-910.
82. Wang, K.; Guo, D.-S.; Wang, X.; Liu, Y. *ACS Nano* **2011**, 5, 2880-2894.
83. Stuar, M. A. C.; Huck, W. T. S.; Genzer, J.; Müller, M.; Ober, C.; Stamm, M.; Sukhorukov, G. B.; Szleifer, I.; Tsukruk, V. V.; Urban, M.; Zauscher, F. W. S.; Luzinov, I.; Minko, S. *Nat. Mater.* **2010**, 9, 101-113.

CHAPTER 4

SWITCHING THE ADHESIVE STATE OF POLYMERIC HYDROGELS USING
PHOTOTITRATION

¹ E. M. White, Jonathan E. Seppala, P. M. Rushworth, B. W. Ritchie, S. Sharma, and J. Locklin.
Reprinted with permission from *Macromolecules*, **2013**, *46* (22), 8882–8887. Copyright 2013
American Chemical Society.

Abstract

A polyacrylamide hydrogel system that can be liquefied by remote activation using UV irradiation is investigated as a degradable adhesive. The linear polyacrylamide copolymer, formed by conventional free-radical polymerization, contains biomimetic catechol–iron-mediated cross-linkers that are sensitive to pH changes. Hydrogel films and bulk gels are prepared by basic titration of a polymer solution doped with a photoacid generator, diphenyliodonium chloride, generating an ionic cross-linked network via the catechol pendant groups. Irradiation of these hydrogels with UV light affords a viscous liquid solution, demonstrating a gel–sol transition with a subsequent decrease in the adhesive strength of the material. These gels may be prepared in high throughput and require few synthetic steps with commercially available precursors.

Introduction

Inspired by cascading biological systems, a proof-of-concept hydrogel which may be converted from an adhesive gel state to a non-adhesive liquid solution state upon UV light irradiation is reported. The facile synthesis and gel-sol transition demonstrates how small influences in network architecture may influence larger macroscopic changes.

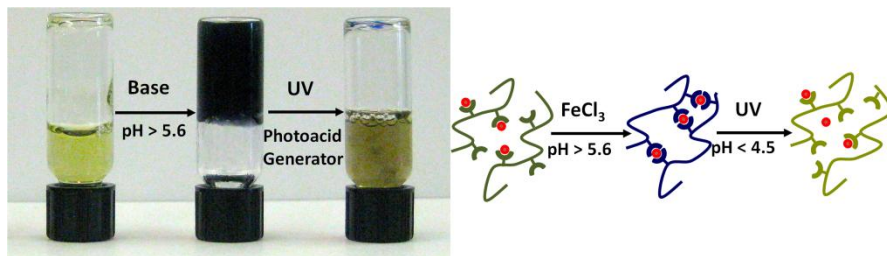


Figure 4.1. Switching the adhesive state of catecholic hydrogels using phototitration. The DOPA residues found in the proteins of coastal muscles is mimicked by and acrylamide analogue.²

The strong, aqueous adhesion of these particular proteins is attributed to the 3,4-dihydroxyphenylalanine (DOPA) residues that coordinatively bond to transition metal oxides on the surface of rocks. Much work has been accomplished to understand the adhesive properties of DOPA, which is found in high concentration in the mussel's adhesive plaques, and similar synthetic analogues.²⁻¹³ Recent polymeric hydrogels containing DOPA analogues have produced a variety of novel devices that respond macroscopically to external stimuli, such as changes in pH¹³⁻¹⁵ or light.^{6, 16} Some other smart hydrogels can respond to changes in ionic strength,^{17, 18} temperature,¹⁹ mechanical stress,^{15, 20} enzymatic degradation,^{21, 22} and light, which is of particular interest because of remote activation.^{6, 16, 23-31}

Among the many stimuli-responsive functions, developing a material that undergoes a sol-to-gel transition has been an attractive response behavior, which often operates on the dissolution or cross-linking of the polymeric network.^{16, 32-38} Such hydrogels are typically 90% or more by weight solvent, and form gels from a prepolymer solution upon the application of a stimulus. The use of gels with switchable architectures, such as cross-linkers, has the potential to contribute added function to biodegradable adhesives, medical devices, and other smart materials. Furthermore, polymeric hydrogel system constructed from acrylic monomers are commonly used commercially due to their ease of fabrication, biocompatibility, and low cost. Combining the use of biomimetic chemistry with acrylic polymers will advance adhesion science with dynamic bonding-debonding architectures.

This paper describes the development of a pH-dependant biomimetic hydrogel that can be switched to a liquid solution state upon irradiation with UV light (254 nm). These hydrogels are prepared post polymerization by cross-linking linear acrylic polymers with the addition of NaHCO₃ in the presence of pendant catechol groups and aqueous Fe³⁺ above pH 5.6 through

coordinative complexation. The iron-catechol complex is switchable, and may be uncross-linked in acidic conditions (Figure 4.2).¹⁴

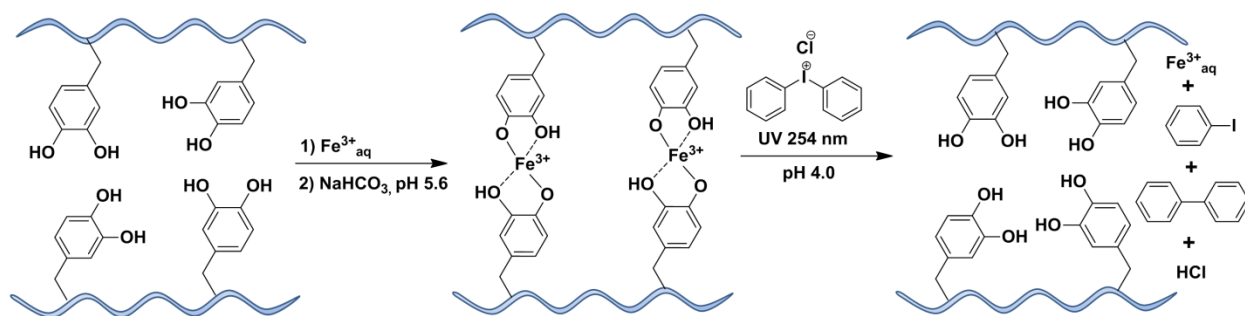


Figure 4.2. Formation of switchable hydrogels and photodegradation. The iron-mediated bis-catechol complex (shown middle) may be dismantled by protonation of the ferric-phenoxide coordinative bond by photo-induced titration with the photoacid generator diphenyliodonium chloride.

This hydrogel system contains two stimuli-responsive components that operate concertedly under UV irradiation, resulting in a decrease in the overall cohesive strength of the material. The pH sensitive DOPA analogue is complexed to aqueous iron through the bis-catechol cross-links by basic titration to pH 5.6 – 7.0.^{13, 15} The network accommodates a light-responsive photoacid generator, which functions as the remote trigger for acid production. As pH decreases within the gel upon UV irradiation, pH sensitive cross-link points are dismantled and the hydrogel reverts to an aqueous solution. Herein we investigated the photo-induced transformation of these systems, as bulk gels and solution cast films, from a gel to the resulting liquid polymer solution.

Experimental Details

Synthesis of N-(3,4-dihydroxyphenethyl)methacrylamide monomer modified from Langmuir, 2009, 25, 6607-6612.

Synthesis and characterization of *N*-(3,4-dihydroxyphenethyl) methacrylamide (DMA) was synthesized in a similar fashion as previously reported.¹¹ 10.0 g of Na₂B₄O₇ (26.22 mmol) and 4.0 g of NaHCO₃ (47.61 mmol) were first dissolved in 100 mL of 18 MΩ water, displaying some insolubility. This solution was degassed for 45 minutes with nitrogen, after which 5.0 g (32.64 mmol) of dopamine HCl was added to the mixture and allowed to stir under nitrogen atmosphere. A separate a solution of 4.7 mL (31.71 mmol) of methacrylic anhydride in 25 mL of degassed THF was prepared and added dropwise. The pH of the reaction mixture was monitored periodically with pH paper and maintained slightly basic (pH 8 – 9) by addition of degassed 1.0 M NaOH. Once all the methacrylic anhydride solution was added, the solution was allowed to stir for 17 hours at room temperature, resulting in a light brown solution. This solution was washed with two 50 mL portions of ethyl acetate and the resulting aqueous layer was filtered. The filtrate was acidified to pH 2 with 6M HCl. This mixture was extracted three times with 50 mL of ethyl acetate, dried with MgSO₄ and condensed down to approximately 20 mL under reduced pressure, and precipitated into 0°C hexane. The white precipitate was collected and recrystallized from boiling ethyl acetate to afford white crystals collected by vacuum filtration and dried under vacuum in 82% isolatable yield. ¹H NMR (300 MHz, DMSO-*d*₆, δ): 8.740 (s, 1H, ArOH), 8.625 (s, 1H, ArOH), 7.927 (t, *J* = 5.4, 1H, NH), 6.630 (d, *J* = 7.9, 1H, ArH), 6.578 (d, *J* = 2.0, 1H, ArH), 6.439 (dd, *J*₁ = 7.9, *J*₂ = 2.0, 1H), 5.616 (t, *J* = 1.5, 1H, CH₂), 5.304 (t, *J* = 1.5, 1H,), 3.230 (q, *J* = 6.0, 2H, CH₂), 2.554 (t, *J* = 7.5, 2H, CH₂), 1.840 (s, 3H, CH₃).

Synthesis of poly(dopamine methacrylamide-co-N-isopropylacrylamide-co-acrylamide).

Acrylamide (1.479 g, 20.81 mmol), *N*-isopropylacrylamide (2.355 g, 20.81 mmol), *N*-(3,4-dihydroxyphenethyl) methacrylamide (0.252 g, 1.138 mmol), and azobisisobutyronitrile (0.043 g, 0.263 mmol) were dissolved in a Schlenk flask with 10 mL DMSO and degassed for 2 hours with argon sparging at room temperature. The solution was then placed in an oil bath thermostated to 60°C for 25 minutes, at which point the solution reaches the gel point. The solution was then quenched by cooling to 0 °C and addition of 40 mL air-free H₂O. This mixture was sonicated and stirred vigorously under nitrogen to redissolve the gel. In a nitrogen glove box, this solution was then washed thrice with 50 mL of degassed dichloromethane and washed once with 50 mL of chloroform. The resulting aqueous layer was precipitated into 50:50 2-propanol:hexane mixture with vigorous stirring resulting in a white, tough, and sticky solid. The polymer was collected by decanting and dried under reduced pressure overnight with an isolatable yield of 82%. The weight average molecular weight (M_w) was determined to be 904 kg/mol by dynamic light scattering (DLS) as shown in Figure S2. The percent catechol retention, χ , of the polymer is determined by the NMR molar ratio, σ , and the molar feed ratio, N , of DMA/NIPAM monomers by equation (1):

$$\chi = \frac{\sigma}{N} \quad \text{(Equation 4.1)}$$

Whereby σ is determined by integrals of the NIPAM proton and two phenolic protons of DMA, Σ_{NIPAM} and Σ_{DMA} respectively, by the equation (2):

$$\sigma = \frac{\frac{\Sigma_{DMA}}{2H}}{\frac{\Sigma_{NIPAM}}{1H}} \times 100\% \quad \text{(Equation 4.2)}$$

All polymer batches prepared at 2.66 mol % DMA retained greater than 97% catechol functionality.

Preparation of hydrogels at 1.6% (w/v)

Dry, native prepolymer p(DMA-co-NIPAM-co-AcAm) is first dissolved at 20 mg·mL⁻¹ with previously degassed water, 5.58 mM DMA content (3 EQ). Once the polymer dissolved, 21 mg·mL⁻¹ of diphenyliodonium chloride (35.7 EQ) was dissolved in the solution with sonication. 1.00 mL of this solution was then mixed with 65 μ L of 28.42 mM FeCl₃ (1 EQ), in a cylindrical mold 0.45 cm high and 2.25 cm in diameter. 200 μ L of 28.42 mM NaHCO₃ (3 EQ) was then mixed aggressively into this solution using a spatula, generating a purple gel which was allowed to cure for 10 minutes covered with a quartz cover slide to prevent evaporation. Thin film gels were prepared in the same fashion except in 75 μ L polymer solution volumes, spread over 645 mm² area on a quartz slide. Subsequently, 15 mg of 28.42 mM NaHCO₃ was then added to the polymer solution by spraying through an aluminum shadow mask to form the gel, at which point the quartz slides are affixed to cure for 10 minutes. The gels were then irradiated with 254 nm light from a hand held UV lamp at a distance of 2 cm for 30 minutes for bulk gels and 60 seconds for thin films.

Results

Synthesis of p(DMA-co-NIPAM-co-AcAm) hydrogel prepolymer was prepared by conventional free radical polymerization of the corresponding acrylamide monomers in DMSO using 2,2'-azobisisobutyronitrile (AIBN) as an initiator (see supplemental information for experimental details). Catechol groups are often protected with alkyl silanes,¹⁴ nitrobenzyl,¹⁶ or boronic esters,³⁹ which prevents oxidation; however, by limiting the polymerization reaction time, increasing monomer concentration, and employing oxygen-free work up protocols, the hydrogel prepolymer was prepared in modest isolatable yields (82%), with a high retention of the

catechol group, (97% by NMR, Figure S1) without the use of protection chemistry. In lieu of aqueous GPC, the polymer's weight average molecular weight, M_w , was determined to be approximately 904 kDa by dynamic light scattering (Figure C.2). The native hydrogel prepolymer solutions were prepared and stored in degassed water prior to use.

Preparation and characterization of hydrogels at 1.6% (w/v)

Previous work by Messersmith and Deming have shown that the catechol groups will irreversibly oxidize to the quinone under basic conditions in the absence of iron.^{3, 40} Addition of aqueous iron to the optimal ratio of 1:3 = Fe^{3+} :catechol (Figure S8) was used for these gels as described in earlier work by the del Campo and Takahara groups.^{6, 14} As the polymer solution is titrated from acidic to more basic pH, there is a distinct increase in viscosity due to the formation of catechol-coordinated ferric ions acting as cross-linkers, along with a discrete colorimetric response (Figure 4.3).

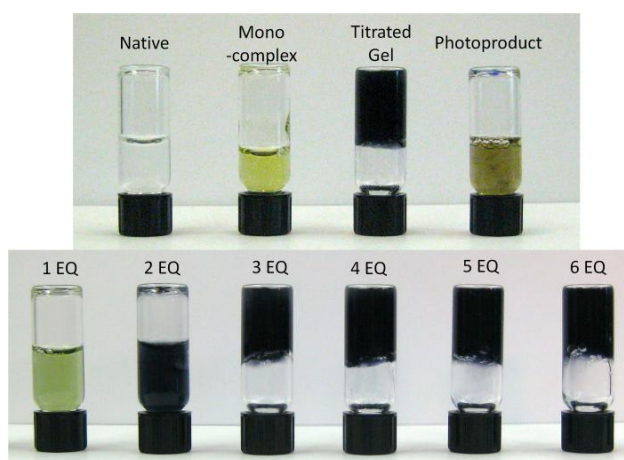


Figure 4.3. Photograph of bulk hydrogels prepared at 1.6 % (w/v) in water. Top: from left to right showing the native polymer solution, mono-complex, titrated gel, and photoproduct. Bottom: demonstrating gel performance and transition about sol-gel point with 1 EQ of NaHCO_3 (pH 4.7) to 6 EQ (pH 7.0).

For bulk gel preparation, 1 mL of 20 mg·mL⁻¹ aqueous, air-free solution of p(DMA-co-NIPAM-co-AcAm) with 5.58 mM DMA content (3 EQ) doped with 21 mg·mL⁻¹ diphenyliodonium chloride (35.7 equivalents, 66 mM) was combined with 65 μL of 28.42 mM FeCl₃ (pH 3.9), generating the green solution of mono-complexed iron-catechol coordinative pendant groups. Titrating the solution to pH 5.6 – 5.7 (3 EQ of NaHCO₃) resulted in a purple gel. Although a strong base like NaOH can be used to induce gelation, the use of the weaker base slowed the rate of gel formation and allowed for a more consistent and uniform gel. Titrating the solution to a ratio of 3:1:3 = DMA:Fe³⁺:NaHCO₃ brings the pH over 5.6 and populates the mixture with the bis-complex cross-linkers and gels the solution. Once gelled, the solution may be irradiated with 254 nm light to generate HCl *in situ* and subsequently uncross-link the gel to form a viscous polymer solution.

Characterization of iron (III) complexation by UV-vis spectroscopy

The sol-gel transition is observed upon the addition of 3 equivalents of NaHCO₃ relative to the catechol groups with gels prepared at 1.6% w/v (Figure 4.3). The colorless native hydrogel prepolymer solution is acidified by the addition of ferric chloride, and catechol complexation was observed by UV-vis spectroscopy through the evolution of a green-yellow solution (Figure S3), with a shoulder peak near 400 nm and a broad peak centered at 710 nm (Figure 4.2). As the mono-complex solution is titrated with NaHCO₃ above pH 5.6, the onset of bis-complex formation is observed by the broad peak centered at 750 nm (Figure 4.4). The decrease in the absorbance at 750 nm and the decrease of the shoulder peak at 400 nm suggest the loss of mono-complexed polymer upon the addition of 6 equivalents of NaHCO₃ (pH = 7.0), and mostly the presence of the bis-complex, $\lambda_{\max} = 585$ nm.

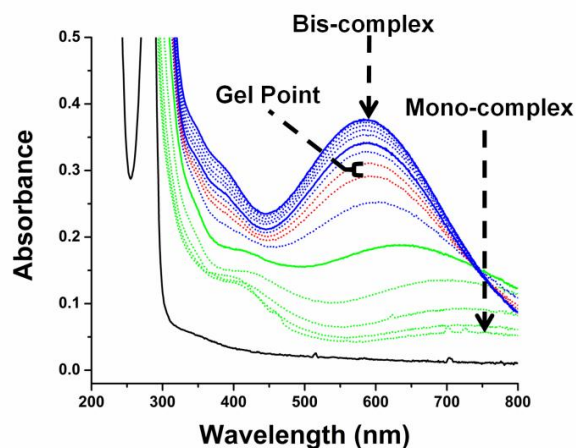


Figure 4.4. UV-vis *in situ* titration and formation of bis-complexed pDMA. The solid black line represents the native catechol polymer in solution at $2 \text{ mg}\cdot\text{mL}^{-1}$. Green lines represent the addition of 2.0 equivalents of NaHCO_3 relative to Fe^{3+} at 0.4 equivalent increments (from pH 4.1 to 5.2). The two solid blue lines represent the addition of 4 and 6 equivalents of NaHCO_3 at pH 6.4 and 7.0 respectively. Red lines represent the gel point pH 5.5 – 5.6.

As pH increases from 4.1 to 5.2 (green lines), the iron-catechol mono-complex displays a hypsochromic shift and, the bis-complex dominates over the mono-complex. Further titrating the gel with sodium bicarbonate to pH 5.5 – 5.6 (red lines) will create a sufficient concentration of cross-link points to form a 1.6 wt% gel. Increasing the pH from 5.6 – 7.0 (blue lines) further cross-links the gel; however, in this system, we aimed to generate a gel just over the sol-gel transition, such that subtle variations in pH would influence a macroscopic transition.

In order to evaluate the phototitration efficacy, a 1.6% (w/v) solution of pDMA-co-NIPAM-co-AcAm was prepared with 3 equivalents of NaHCO_3 relative to ferric ions and was irradiated with 254 nm UV light at $0.22 \text{ mW}\cdot\text{cm}^{-2}$ (Figure 4). The peak at 585 nm representing the bis-complex disappears after approximately 25 minutes of UV exposure. The molar

extinction coefficients for diphenyliodonium chloride and the bis-complex at 253.9 nm was measured to be $5160 \text{ M}^{-1}\cdot\text{cm}^{-1}$ and $2110 \text{ M}^{-1}\cdot\text{cm}^{-1}$ respectively (Figure S4).

The polymer was prepared at $1 \text{ mg}\cdot\text{mL}^{-1}$ (0.28 mM DMA content) concentrations with 3.32 mM, 0.332 mM, and 0.033 mM (35.7EQ, 3.57 EQ and 0.36 EQ respectively) diphenyliodonium chloride concentrations for UV-vis studies in order to investigate the time dependence of the system on photoacid concentration and the minimum photoacid required to reduce the catechol cross-links. Figures S11 and S12 show the corresponding NaHCO_3 titration data with in situ UV-vis data and subsequent phototitration for 300 seconds (20 second exposure intervals) at these concentrations. Phototitration of the bis-complex down to pH 4.6 was observed to occur in 300 and 180 seconds in the case of the 0.332 mM and 3.32 mM diphenyliodonium chloride experiments respectively, but the bis-complex remained at pH 5.4 at 0.033 mM photoacid generator after 300 seconds exposure. At pH 4.6, an equivalence point was observed (Figure S5), suggesting that not all ferric ions are dissociated, rather there is a distribution of mono-complexed and protonated catechol groups below pH 4.6.

The concentration of the photoacid generator is twelve times larger than the DMA complex; therefore, the majority of the UV light is absorbed by the diphenyliodonium chloride rather than the DMA pendant groups. Production of HCl from photoacid action under UV light titrates the gel to approximately pH 4.6, reducing the bis-complex cross-linker to a mixture of the mono-complex and protonated catechol moiety, effectively liquefying the gel to a solution (Figure S5). Irradiation of the control experiment with no photoacid generator present shows no significant change in bis-complex concentration or in pH (Figure S10).

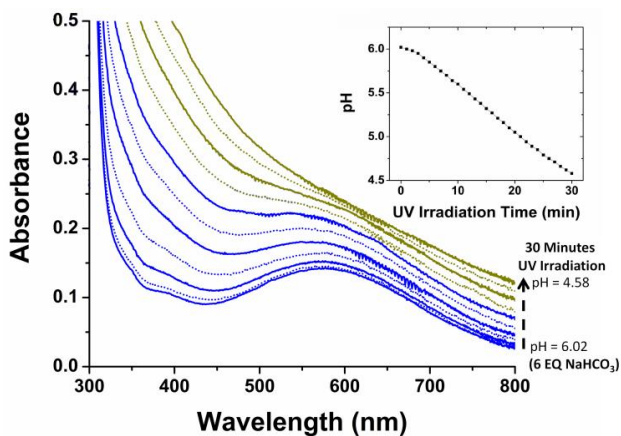


Figure 4.5. UV-vis *in situ* phototitration and dismantling of the bis-complex. A $2 \text{ mg}\cdot\text{mL}^{-1}$ pDMA solution was first titrated to pH 6.02 with NaHCO_3 and subsequent irradiation for 30 minutes at $0.22 \text{ mW}\cdot\text{cm}^{-2}$. The inset is the corresponding titration curve. The overall increase in spectral absorbance is due to light scattering of immiscible photoproducts. Solid lines correspond to 6 minute intervals of UV exposure.

Since only the bis-complex is associated with cross-linking, changes in the concentration of the mono-complex do not change molecular weight between cross-links. It is important to note that the spectra in Figure 4 show an increase in scattering with time at longer wavelengths, which presumably occurs through irreversible cross-linking of the polymer backbone (Figure S6 and S12). This photoproduct is confined as a film on the UV-solution interface, and was easily discarded for reproducible mechanical analysis. Furthermore, the use of a photoacid generator that absorbs at lower energy wavelengths would reduce the formation of the insoluble photoproducts.

Mechanical analysis of hydrogels

Hydrogels were prepared as both bulk gels and films, depending on the analysis technique. The response time for liquefaction of 0.45 cm thick bulk hydrogels is on the order of minutes (Figure S7) to complete the phototitration, while thin films are liquefied in 60 seconds. The bulk hydrogels were prepared at 1.6 wt. % for analysis via small amplitude oscillatory shear (SAOS) to investigate the gel and sol material properties (Figure 5).

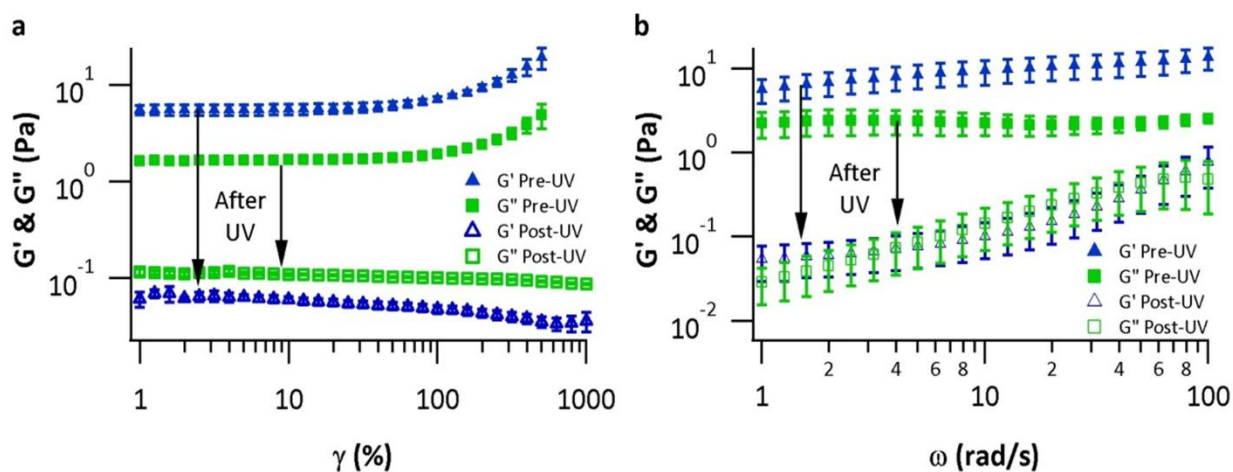


Figure 4.6. Isothermal strain sweeps of 1.6 wt. % hydrogels. Strain sweeps, **a**, and isothermal frequency sweeps, **b**, of 1.6 wt. % hydrogels prepared at 3:1:3 = DMA:Fe³⁺:NaHCO₃ (pH 5.6) before and after UV irradiation with 254 nm light. Error bars indicate first standard deviation from 5 independent samples.

The pre-UV hydrogel exhibits a typical cross-linked material response where the storage modulus (G') is greater than the loss modulus (G''), and the material exhibits shear thickening at high strain amplitude. After UV irradiation, the loss modulus dominates ($G'' > G'$) and the material exhibits slight shear thinning, typical of polymer solutions, demonstrating the material

has transitions from gel to sol. Evidence of this transition by rheological data helps support that the mechanism for liquefaction is acidic titration of the iron-catechol bis-complex.

For thin film preparation, the hydrogel is prepared in the same manner as for bulk gels except in 75 μL volumes spread over one square inch area (645 mm^2) on two quartz slides. To evenly distribute base, the mono-complex prepolymer solution was titrated gravimetrically by adding approximately 15 mg of 28.42 mM NaHCO_3 (3 equivalents) by spraying through an aluminum shadow mask. Immediately after introducing the base, the gel film turned purple in color, and a second quartz slide was affixed to the gel to cure for 10 minutes (Figure S6).

The gels are prepared as films to expedite the reaction time because UV exposure is limited to the gel interface; therefore, acid titration of the cross-link points is assumed to be a diffusion limited process from that interface. The adhesive properties of the gel were analyzed by lap-shear adhesion testing on an Instron tensile tester using a 1.27 mm/min displacement rate. Upon exposure to 60 seconds of 254 nm UV light at a distance of approximately 2 cm ($1.20 \text{ mW}\cdot\text{cm}^{-2}$), the adhesive film's maximum tensile shear strength dropped from 1.68 kPa before irradiation to 0.35 kPa after irradiation (Figure 6). In both experiments, before and after UV exposure, the gel fails cohesively, implying a network failure, rather than adhesive debonding. A time-lapse video of the debonding event in which the substrate supports a 20 g load is shown in the supplemental information.

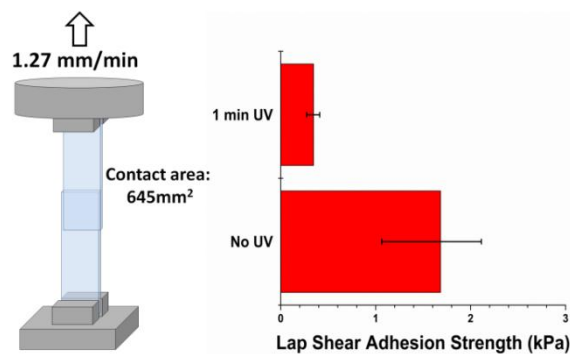


Figure 4.7. Lap shear adhesive strength testing of a 1.6 wt. % hydrogels. The gels were tested before and after UV irradiation at $1.2 \text{ mW} \cdot \text{cm}^{-2}$. Error bars represent the first standard deviation from 8 independent samples.

Similar to the SAOS measurements a large decrease in adhesion strength is observed between the gels before and after UV irradiation, suggesting that the network of catechol cross-links is dismantled as the pH decreases. Earlier work by the Messersmith group showed that the breaking force of a metal-catechol bond is a modest 0.8 nN of force compared to a covalent bond which requires 2-3 nN of force to rupture,³ and more recent work by Zhiping attests to the high bond strength (approximately 6 nN) required to rupture the ferric-catechol bis-complex by DFT calculations.⁴¹ We speculate that the onset of bis-complex formation at pH 5.6 observed by UV-vis develops a minimum population of bis-complex cross-linkers with sufficient mechanical strength to gel the solution. Titrating the hydrogel about this ratio gives the most dramatic changes in cohesive mechanical strength at small changes in pH.

Conclusion

Acrylic copolymer hydrogels offer an attractive approach for the development of smart hydrogels due to their ease of fabrication and commercially available starting materials. We have

designed a biomimetic catechol-based hydrogel that may be remotely activated to photo-degrade back into a sol, displaying a decrease in the modulus and lap shear adhesion strength of the material. Hydrogels prepared in this fashion at pH 5.6 – 6.0 supplies the hydrogel with bis-complex cross-links, demonstrating a sol-gel transition which may be titrated back to a solution with a decrease in pH. This hydrogel incorporates two cooperative systems, a photoacid generator and a pH-responsive cross-linker. Currently we are exploring the use of photobase generators in efforts to develop a material capable of undergoing sol-gel transitions without the constraints of added mass.

Acknowledgements

We gratefully acknowledge financial support from the National Science Foundation (CAREER Award, DMR 0953112).

References

1. White, E. M.; Seppala, J. E.; Rushworth, P. M.; Ritchie, B. W.; Sharma, S.; Locklin, J. *Macromolecules* **2013**, 46, 8882-8887.
2. Waite, J. H. *Nat. Mater.* **2008**, 7, 8-9.
3. Lee, H.; Scherer, N. F.; Messersmith, P. B. *Proceedings of the National Academy of Sciences* **2006**, 103, 12999-13003.
4. Lee, H.; Dellatore, S. M.; Miller, W. M.; Messersmith, P. B. *Science* **2007**, 318, 426-430.
5. White, J. D.; Wilker, J. J. *Macromolecules* **2011**, 44, 5085-5088.
6. Shafiq, Z.; Cui, J.; Pastor-Pérez, L.; San Miguel, V.; Gropeanu, R.; Serrano, C.; del Campo, A. *Angewandte Chemie (International ed. in English)* **2012**, 51, 4332-4335.
7. Yamada, K.; Aoki, T.; Ikeda, N.; Hirata, M. *J. Appl. Polym. Sci.* **2007**, 104, 1818-1827.

8. Monahan, J.; Wilker, J. J. *Langmuir* **2004**, 20, 3724-3729.
9. Lee, B. P.; Messersmith, P. B.; Israelachvili, J. N.; Waite, J. H. *Annual Review of Materials Research* **2011**, 41, 99-132.
10. Chiridon, W. M.; O'Brien, W. J.; Robertson, R. E. *J. Biomed. Mater. Res. Part B* **2003**, 66B, 532-538.
11. Glass, P.; Chung, H.; Washburn, N. R.; Sitti, M. *Langmuir* **2009**, 25, 6607-6612.
12. Brooksby, P. A.; Schiel, D. R.; Abell, A. D. *Langmuir* **2008**, 24, 9074-9081.
13. Holten-Andersen, N.; Harrington, M. J.; Birkedal, H.; Lee, B. P.; Messersmith, P. B.; Lee, K. Y. C.; Waite, J. H. *Proceedings of the National Academy of Sciences* **2011**, 108, 2651-2655.
14. Xu, H.; Nishida, J.; Ma, W.; Wu, H.; Kobayashi, M.; Otsuka, H.; Takahara, A. *ACS Macro Lett.* **2012**, 1, 457-460.
15. Krogsgaard, M.; Behrens, M. A.; Pedersen, J. S.; Birkedal, H. *Biomacromolecules* **2013**, 14, 297-301.
16. Nishida, J.; Kobayashi, M.; Takahara, A. *ACS Macro Lett.* **2013**, 2, 112-115.
17. Bassik, N.; Abebe, B. T.; Laflin, K. E.; Gracias, D. H. *Polymer* **2010**, 51, 6093-6098.
18. Thérien-Aubin, H.; Wu, Z. L.; Nie, Z.; Kumacheva, E. *J. Am. Chem. Soc.* **2013**, 135, 4834-4839.
19. Hu, J.; Liu, S. *Macromolecules* **2010**, 43, 8315-8330.
20. Haque, M. A.; Kurokawa, T.; Kamita, G.; Yue, Y.; Gong, J. P. *Chem. Mater.* **2011**, 23, 5200-5207.
21. Vemula, P. K.; Cruikshank, G. A.; Karp, J. M.; John, G. *Biomaterials* **2009**, 30, 383-393.

22. van Bommel, K. J. C.; Stuart, M. C. A.; Feringa, B. L.; van Esch, J. *Organic & Biomolecular Chemistry* **2005**, 3, 2917-2920.
23. Ercole, F.; Thissen, H.; Tsang, K.; Evans, R. A.; Forsythe, J. S. *Macromolecules* **2012**, 45, 8387-8400.
24. Kim, S.-H.; Hwang, I.-J.; Gwon, S.-Y.; Son, Y.-A. *Dyes and Pigments* **2010**, 87, 158-163.
25. Szilágyi, A.; Sumaru, K.; Sugiura, S.; Takagi, T.; Shinbo, T.; Zrínyi, M.; Kanamori, T. *Chem. Mater.* **2007**, 19, 2730-2732.
26. Kloxin, A. M.; Kasko, A. M.; Salinas, C. N.; Anseth, K. S. *Science* **2009**, 324, 59-63.
27. Tibbitt, M. W.; Anseth, K. S. *Biotechnology and Bioengineering* **2009**, 103, 655-663.
28. Tibbitt, M. W.; Kloxin, A. M.; Dyamenahalli, K. U.; Anseth, K. S. *Soft Matter* **2010**, 6, 5100-5108.
29. Tibbitt, M. W.; Kloxin, A. M.; Sawicki, L. A.; Anseth, K. S. *Macromolecules* **2013**, 46, 2785-2792.
30. White, E. M.; Yatvin, J.; Grubbs, J. B.; Bilbrey, J. A.; Locklin, J. *Journal of Polymer Science Part B: Polymer Physics* **2013**, 51, 1084-1099.
31. Wang, E.; Desai, M. S.; Lee, S.-W. *Nano Lett.* **2013**, 13, 2826-2830.
32. Yang, Z.; Gu, H.; Fu, D.; Gao, P.; Lam, J. K.; Xu, B. *Advanced Materials* **2004**, 16, 1440-1444.
33. Yang, Z.; Liang, G.; Wang, L.; Xu, B. *J. Am. Chem. Soc.* **2006**, 128, 3038-3043.
34. Toledano, S.; Williams, R. J.; Jayawarna, V.; Ulijn, R. V. *J. Am. Chem. Soc.* **2006**, 128, 1070-1071.
35. Vemula, P. K.; Li, J.; John, G. *J. Am. Chem. Soc.* **2006**, 128, 8932-8938.

36. Williams, R. J.; Smith, A. M.; Collins, R.; Hodson, N.; Das, A. K.; Ulijn, R. V. *Nature Nanotechnology* **2009**, 4, 19-24.
37. Yang, Z.; Ma, M.; Xu, B. *Soft Matter* **2009**, 5, 2546-2548.
38. Ryu, J. H.; Lee, Y.; Kong, W. H.; Kim, T. G.; Park, T. G.; Lee, H. *Biomacromolecules* **2011**, 12, 2653-2659.
39. Su, J.; Chen, F.; Cryns, V. L.; Messersmith, P. B. *J. Am. Chem. Soc.* **2011**, 133, 11850-11853.
40. Yu, M.; Hwang, J.; Deming, T. J. *J. Am. Chem. Soc.* **1999**, 121, 5825-5826.
41. Zhiping, X. *Scientific Reports* 3, 2914.

CHAPTER 5

HYDROGELS IN MEDICINE AND CONCLUDING REMARKS

Introduction and Problem

Accidents are a part of human nature, and injury or surgery to correct the damaged tissues of the body is also a familiar scene to most. The medical industry has made many great steps in the evolution of wound management. Improved morbidity rates, lowered post-surgical complications, and expedited recovery times with less scarring are all important attributes in the advances of wound care. From damp cloth bandages to today's more exotic options, there has been a continual turnover of wound care technology, all built on previous efforts and advancements. Of the many types of wound care options, hydrogels are a common selection for many serious or chronic wounds, burns, severe abrasions, and surgical sites that are common locations for infection.

Wound care hydrogels are sterile and often doped with broad-spectrum antimicrobial agent, pH balancing buffers, and other nutrients vital to the wound's endogenous eukaryotic cell growth. Hydrogels offer the advantages of maintaining wound moisture content by preventing wound desiccation and absorbing exudates to prevent wound maceration at oozing wound sites. For severe burn and abrasion victims, a niche compendium of hydrogels is in use in hospital settings. Still today, however, it is common practice to use sterile cotton-based packing media to fill wound voids and to absorb exudate. Presented here are the design concept, some preliminary

results, proposed methodologies, and theories on the mechanisms for use of antimicrobial catecholic hydrogels to maintain the health of eukaryotic cell growth during wound healing.

Hydrogels are often used on relatively new wound sites, where bleeding and bodily fluid leakage is substantial. The hydrogels are typically partially hydrated gels or dry-state polymers capable of swelling to many times their own mass by absorbing exudate. These gels are often backed with a liner of polyethylene, cellophane, or a semi-permeable membrane to act as a moisture and foreign body barrier, akin to the epidermis in function. Wounds that are managed with antimicrobial hydrogels or petroleum jelly both aim to impart moisture retention at the wound site. Oil-based jellies prevent desiccation by forming a moisture barrier for wounds that have stopped or have minimal leaking of bodily fluids and are useful for maintaining closed wound sites with newly developed skin tissue.

A number of broad spectrum antimicrobial topical treatments are available on the market, and the antimicrobial mechanisms of silver-based preparations have been recently confirmed.¹ Silver antibacterial preparations have already shown to inhibit bacterial growth in catechol containing hydrogels.² Recent work has focused on understanding the role of reactive oxygen species in antimicrobial systems using Ag^+ and Ag nano particles alike.³ In pDMA hydrogels at pH 7.4, silver precipitation is rapid in the presence of oxygen and absence of iron, leading to a cross-linked network. Similarly, using DOPA cross-links, a poly(ethylene glycol) (PEG) based poly dopamine was investigated by a year-long *in vivo* biocompatibility study of an islet transplantation, whereby pancreas cells are transplanted from a host to a donor by gluing them with this gel.⁴ Indeed, the formation of poly dopamine and quinone-linked hydrogels showed good biocompatibility for the PEG analogue. However these gels are irreversible, and if the reversible ferric-phenoxide chemistry is to be preserved, special attention to the cross-linking

complex must be addressed. Thus, our objective is to imbed within a reversible hydrogel antimicrobial compounds that maintain their antibacterial activity while facilitating wound healing.

A local company, Molecular Therapeutics®, has developed advanced potentiated® antimicrobial preparations, including preparations that contain silver in solution that is stable in physiologic conditions. This company manufactures Silvion® and SilaKlenz®, both of which are FDA cleared for acute and chronic wounds including post-surgical applications. The current Silvion-SilvaKlenz technology is applied regularly as a spray to topical wound sites and has shown *in vitro* antimicrobial activity against drug resistant microbes such as Methicillin resistant *Staphylococcus aureus* (MRSA), Vancomycin resistant *Enterococcus faecalis* (VRE), multi-drug resistant *Pseudomonas aeruginosa*, and multi-drug resistant *Acinetobacter baumannii*.⁵ Given the successes of this antimicrobial among others like it, silver-based antimicrobials will remain an active area of research and product development for some time. And like all medical developments, continuing innovation is important to advance the technology and to stay competitive in health care. Our goal is to incorporate potentiated silver, as well as other potentiated antimicrobials will into a stimuli-responsive, biomimetic hydrogel akin to the one presented in Chapter 4.

Design Constraints and Considerations

The aim of the project is to develop a self-healing, moldable hydrogel with liquefaction as a response to low concentrations of EDTA and surfactants. The objective is to provide a self-healing hydrogel as a delivery vehicle for a potentiated silver solution, which will offer continual application of moisture-balanced silver to the site. If the conditions present at the wound-

hydrogel interface are sufficiently suitable for mitosis, new cells should be facilitated to grow unhindered by bacterial activity, granted the gel exhibits no cytotoxicity. Therefore, the hydrogels must preserve the antimicrobial efficacy and accelerate wound healing, as shown in the conceptual illustration, Figure 5.1:

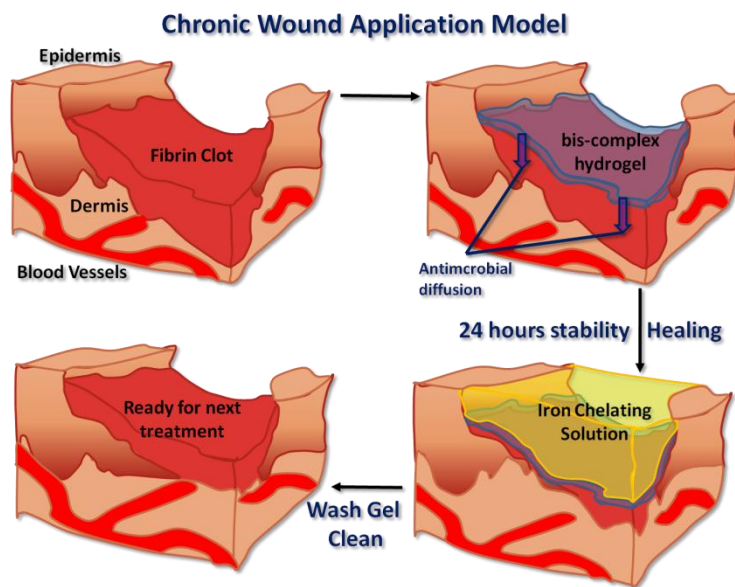


Figure 5.1. Schematic representation of the application and healing model. Note that chronic wounds are often covered with fibrinous clots.

The objective is to extend the duration of silver delivery, thus decreasing the frequency of patient wound manipulation, and investigate how wound healing is affected by the mechanical properties of self-healing gels. The model presented in Figure 5.1 suggest gels are to be reapplied every 24 hours; however, longer times would be more beneficial. Gels may be prepared at very low strengths, like that of jellies, or high concentrations that may approximate the overall properties of natural scabs. With the engineering and tuning of mechanical properties of these gels come economic considerations that are also worth noting.

The hydrogels must be prepared with both practical cost analysis of starting materials and reaction yields, so that the gel is economically viable. A price-point of \$2.00 per gram of

purified polymer was set as a goal for research scales. Furthermore, compounds responsible for the hydrogel oxidative stability and function must be on the FDA's Generally Regarded as Safe (GRAS) list in order to be compliant with regulations. This list was established in 1958 to provide the standard candle for safe food additives and food contact chemicals. Congress recognized that many substances "*intentionally used in a manner whereby they are added to food would not require a formal premarket review by FDA to assure their safety...*" because of the safety, nature, or history of the compound in food use.⁶ A select committee on GRAS substances (SCOGS) was established, which reviewed reports published between 1972-1980 on the safety of over 370 generally recognized as safe (GRAS) food substances. Not included in this database are 539 compounds that have been or currently are under consideration by SCOGS, and the FDA announces letters that rank the safety level, and therefore, the regulation of these compounds.

All together, these 370 and potentially more compounds represent the viable starting materials for topical hydrogels. These compounds, their properties, and the reactions among them populate a relatively constricted tool box for making smart materials; however, by closer inspection of the available structures, some interesting pathways to create useful smart materials are available when considering how nature treats these compounds.

Dissolution Studies

One of the primary advantages of the DOPA-containing hydrogels outlined in Chapter 4 is the ability to dissolve with either acidification, or by competitive ligation with ferric cross-linking. First demonstrated by the Messersmith and Waite groups in 2011,⁷ the ferric-phenoxide complex may be dismantled by a high ionic strength solution (150 mM) EDTA at pH 4.7. This

process is, however, diffusion limited for hydrogels, and a hydrogel approximately 1 mL in volume will take 1 hour to full dissolve, as shown in Figure 5.2.

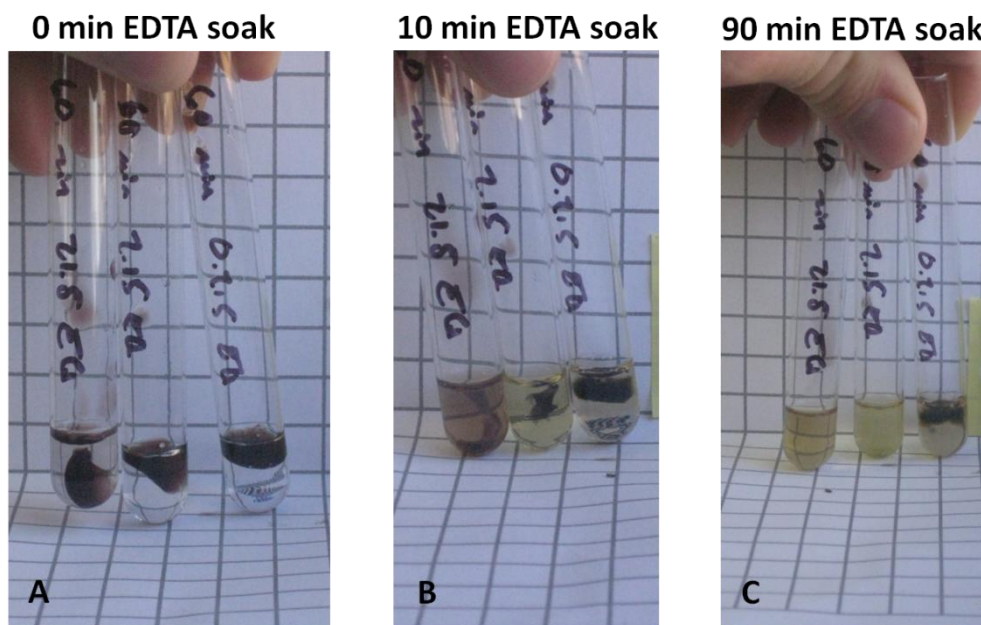


Figure 5.2. Dissolution study of air-stable 6 wt% pDMA. Gels dissolve in 100 mM EDTA solution at pH 7.0. The hydrogel was prepared with 21.5, 2.15, and 0.215 equivalents of sodium ascorbate relative to DOPA and exposed to air for 24 hours. The dissolution of samples with 21.5 equivalents of sodium ascorbate was complete after 90 minutes.

With this time constraint, the thickness of the hydrogel layer applied to wound sites should remain low, as shown in Figure 5.1. Similarly, for these hydrogels to become useful targets for *in vitro* studies, the oxidative stability must be improved. A notorious issue for 3,4-dihydroxyphenethylamines is oxidative stability in basic solutions, so an answer to this instability must be found in order to prove this cross-linking chemistry viable for *in vivo* studies.

Shelf-Life

The catechol group is notorious for the oxidative instability exhibited at physiological pH, and much work has been accomplished to understand the oxidation pathways. The Messersmith group investigated the formation of polydopamine via a two-electron oxidation through a leukodopaminechrome intermediate.⁸ The mechanism of one-electron oxidation will be discussed later. Similarly, in the DOPA hydrogels prepared in Chapter 4 with $\text{FeCl}_3 \cdot 6\text{H}_2\text{O}$, the ferric species had to be prepared fresh, as the formation of FeOH_3 is significant even below pH 5.0. Like nature's iron-grabbing haemoglobin and ferritin complexes and bacteria's enterobactin peptides that sequester iron, the ferric-phenoxide complex in pDMA hydrogels may be oxidatively stabilized with high binding affinity chelating ligands called siderophores.⁹ The crowding of high binding affinity siderophores with denticities of 2, 4, and 6 with respect to $[\text{Ar}] 3d^5$ octahedral configurations, iron(III) can afford stable ferric-complexes. The siderophore-iron(III) affinity constants (pFe^{III}) for a catecholate chelator enterobactin and a hydroxamate desferrioxamine B are 35.5 and 25.0, respectively. These values are on a log scale, indicating that the enterobactin has a roughly 10^5 higher affinity for iron(III) than does desferrioxamine B. By comparison, the pFe^{III} value for the hydroxide anion is 14.6 at physiological pH.⁹

The FDA allows iron supplements in food products like enriched cereal and multivitamins in the form of iron ammonium citrate. The citrate stabilized iron, $\text{pFe}^{\text{III}} = 15.0$ at pH 7.4,⁹ may be exchanged with several ligands until exposed to catecholate ligands in pDMA, in which binding may be monitored by the material's change in mechanical properties. Citrate ligands help prevent Fenton-like reaction when compared to chloride.⁷ This cascading ligand exchange process results in air stable bis-complexed iron-catechol bonds between pH 7.0 and

9.5. The schematic representation in Figure 5.3 illustrates the principle of ligand exchange of siderophores.

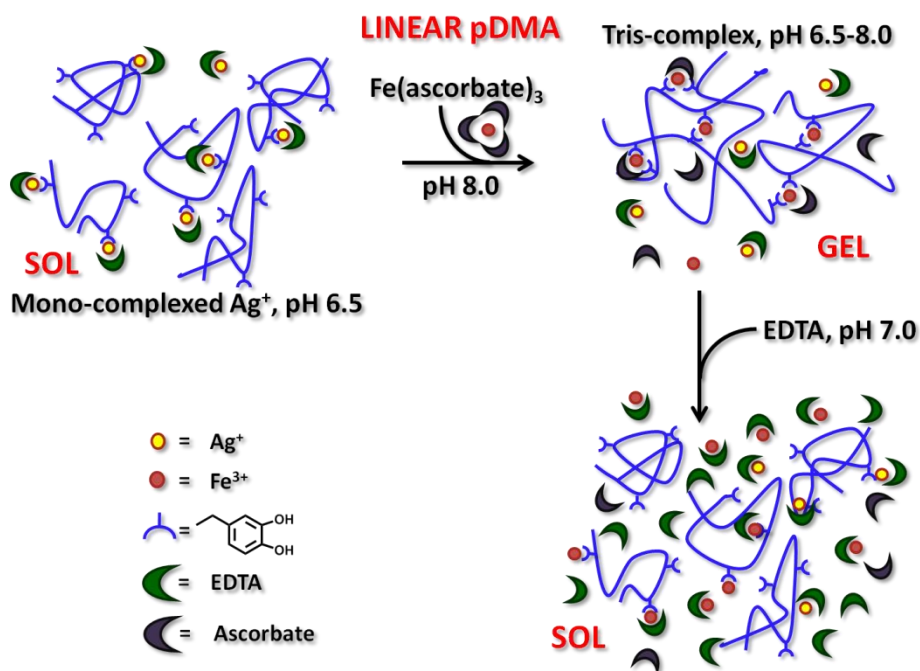


Figure 5.3. Schematic representation of ligand and metal exchange. The Fe(ascorbate)_3 is prepared fresh and separately from iron(III) ammonium citrate and sodium ascorbate at pH 7.0.

Maintaining pH is important to determining the equilibriums of all species in the hydrogel system. In general, as pH is lowered, fewer cross-links exist in the gel and strength of the gel decreases, in turn leading to accelerated creep. The pH of the gels is maintained around 7.0 – 7.5, although prolonged air exposure does lower the pH as low as 6.0 in very dilute gels. The decrease in pH is likely associated with the production of dehydroascorbic acid (DHA), an oxidized form of ascorbic acid, but the mechanism of acid production has not yet been determined for these hydrogels. I posit the reaction is likely due to the reduction oxidation of the DOPA group by a Michael-type reaction of ascorbate with the catechol semi-quinone.

The pH Balance

The hydrogel pH plays an important role in dictating the mechanical properties by varying tris-, bis-, and mono-complexes. The concentration of bis- and tris-complexes may be determined from the speciation plot of catecholic gels as shown in Figure 5.4.

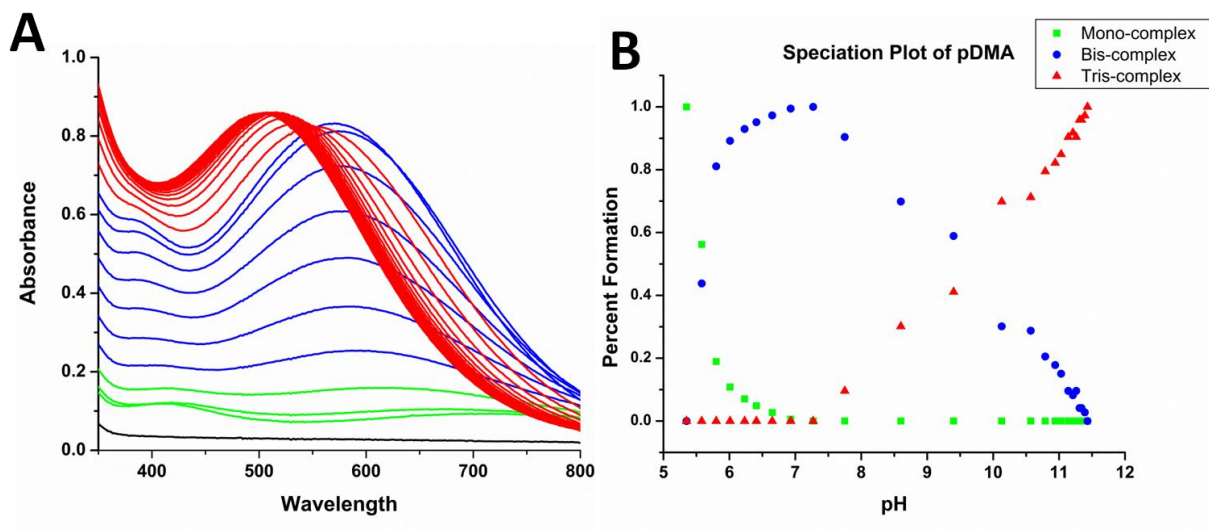


Figure 5.4. Speciation plot of pDMA hydrogels from pH 5.2 to 11.5. **A.** Overlay UV-vis spectra of a 2 wt% pDMA solution titrated from pH 5.2 to 11.5 with NaOH. **B.** Speciation plot for the mono-, bis-, and tris-complexes varying pH.

By blocking the open chelating site in the bis-complex with ascorbate, a suitable Michael donor is immediately next to the DOPA groups of pDMA. The ascorbate anion can also terminate radicals produced either from Fenton Chemistry or other oxidative stress. Figure 5.5 determined by Lee and co-workers, outlines one- and two-electron oxidation pathways to produce irreversible cross-links.¹⁰

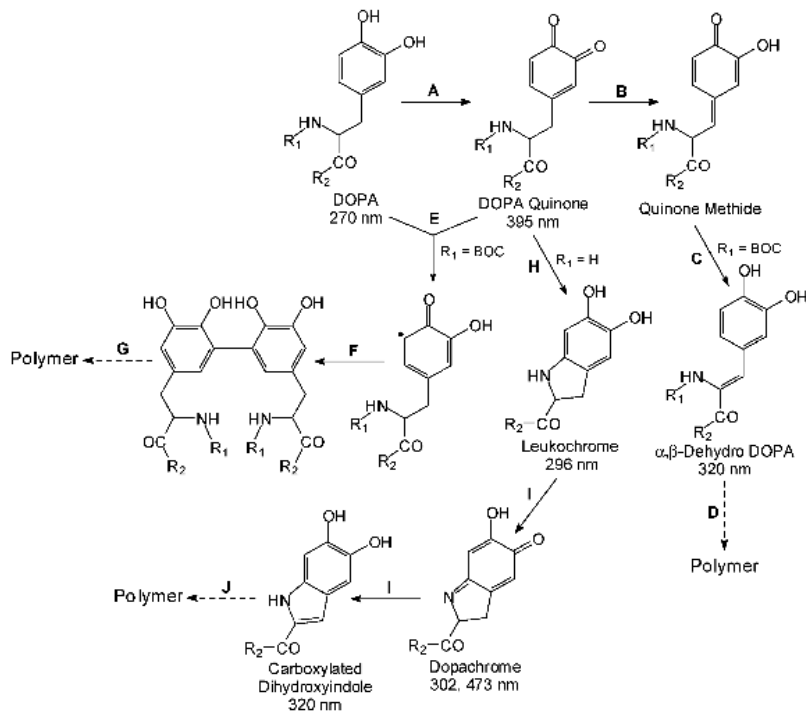


Figure 5.5. Possible oxidation pathways for DOPA compounds. Key: (A) Oxidation by catechol oxidase or other oxidizing reagents. (B) Tautomerization of DOPA quinone. (C) Release of α proton. (D) Cross-linking by a pathway similar to that occurring in insect cuticle sclerotization. (E) Aryloxy free radical generation. (F) Phenol coupling. (G) Further oxidation to form cross-linked polymer. (H) Internal cyclization with $R_1 = H$. (I) Rearrangement of cyclized DOPA derivatives. (J) Cross-linking by a pathway resembling that occurring in melanin formation. Dashed arrows indicate poorly understood pathways that lead to the formation of cross-linked polymers.¹⁰ Reprinted with permission from *Biomacromolecules* **2002**, 3, 1038-1047. Copyright 2002 American Chemical Society.

The oxidative reactivity of catecholic species has drawbacks, and other siderophores may also be investigated. Earlier work by Rosthauser and coworkers in the early 1980s outlines the synthesis of N-hydroxamic acid copolymers through similar iron coordination that exhibit a

similar binding affinity in dilute polymer solutions.¹¹ Of the siderophores outlined by Hider and coworkers,⁹ many may likely be incorporated into synthetic biomimetic hydrogels, and advantageous material properties may arise. Oxidative stability may arise from hydroxamate polymers at the expense of binding affinity to iron, and polymer architectures, i.e. branched polymers or dendrimers, of different biomimetic chemistry also shouldn't be ignored. I speculate that in catecholic systems, semiquinone species may reduce Ag(I) allowing quinone-initiated radical coupling to catechols as well as simultaneous silver nanoparticle formation by the production of Ag(0).

Anti-microbial Studies

Establishing a base model for effective antimicrobial activity is necessary to understand the hydrogel passivity to small molecules, macromolecules, and larger particles. The air-stable hydrogels were doped with $5.1 \text{ mg}\cdot\text{mL}^{-1}$ of potentiated neomycin sulfate to investigate the bacterial growth zone of inhibition. Interestingly, a relatively small margin of approximately 2 cm was observed, show in Figure 5.6.



Figure 5.6. Incubation of a 6 wt% pDMA hydrogel with *S. aureus*. The gel showed a zone of inhibition when loaded with $5.1 \text{ mg}\cdot\text{mL}^{-1}$ potentiated neomycin sulfate.

The potentiated neomycin concentration is relatively high ($5.1 \text{ mg}\cdot\text{mL}^{-1}$) for the zone of inhibition observed here. A semi-permeable membrane may be responsible for the minimal dissolution of the antimicrobial, but more studies are going to be required to understand the rate and concentration of antimicrobials releases from these hydrogels. Fluorescence microscopy studies on fluorescently labeled particles may lend clues to the influence of the mesh size on varying particle dimensions.

Stability Studies – pH and mechanical properties

There is an ongoing stability test for candidate 6 and 9 wt% pDMA Silvion 1X hydrogels. The two hydrogel types outlined in Figure 5.7 are under study for long term shelf-life storage. The engineering of the containers is an important parameter to consider, as gas permeability varies with how the hydrogel is stored. Also application duration and preparation should be considered. Presented below is rotary amplitude sweeps of 12 catecholic hydrogels prepared at

varying iron and polymer concentrations; all hydrogels were stored in 10 cm glass vials fitted with new rubber septa.

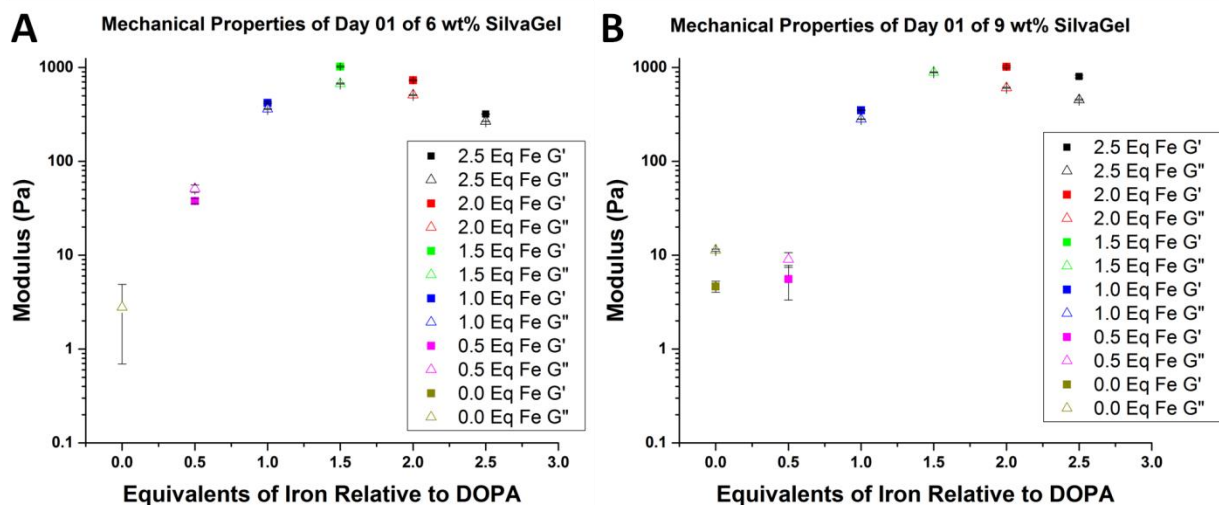


Figure 5.7. Storage modulus (G') and loss modulus (G'') varying iron content. The average storage modulus (G') and loss modulus (G'') data were collected from isothermal strain sweeps of 6 and 9 wt% pDMA SilvaGel® varying iron concentration relative to DOPA groups.

The stability test continues to date, and the results from this air stability study will help determine which system is best suited for animal models and where improvement will be needed. Will one of these candidate hydrogels kill bacteria efficiently when compared to conventional Silvion and SilvaKlenz treatment? How will the mechanical properties change over months or years, and will dissolution be preserved? So long as these criteria are met, the implications and influences of the mechanical properties of self-healing catecholic hydrogels may become more apparent.

Mesh Size Calculations for Particle Delivery

The mesh size of these gels may be related to the swollen state polymer volume fraction, $v_{2,s}$, (analogous to the *degree of swelling*) by the calculations described in Equations 3.3 and 3.4. The calculated mesh size for these 6 wt% hydrogels is 9.6 nm, according to Equations 3.9 – 3.12. In lieu of aqueous GPC, the weight average molecular weight, M_w , of pDMA was determined by light scattering to be $904 \text{ kg}\cdot\text{mol}^{-1}$, and the hydrodynamic radius was measured to be 30.90 nm. Due to the Trommsdorff effect observed in the formation of pDMA, the dispersity, \mathcal{D} , is assumed to be high.¹² The high dispersity increases the adhesion, or tack, in pressure sensitive adhesives formed from low T_g polyacrylates, and likely have the same effect on solvated hydrogels with high T_g comonomers. The dispersity is assumed to be 6.0, similar to polymers formed at near the gel point due to the Trommsdorff effect. This presents a better picture of the polymer network and what particles may diffuse through the hydrogel.

Next Generation Shear Thinning Gels

It is important to consider future improvements on the hydrogel system. One pitfall of reversible, self-healing catecholic hydrogels is the material's innate propensity to creep. The material is a true gel, that is $G' > G''$ and the gel shear thickens at high strain rates; however, at very low strain rates such as sitting under the material's own weight, the hydrogel will flow slowly with time. Work from the Langer group demonstrated how dextran based nanoparticles of chitosan-coated and alginate-coated dextran particles, 340 and 293 nm respectively, displayed shear thinning behavior, a desirable trait for injectable gels.¹³ Similarly, polydisperse microgels of p(NIPAM-co-acrylic acid) were fabricated over a range of sizes with shear thinning character. The AFM height images in Figure 5.8 shows the nano- to micro-sized particles cast on mica.

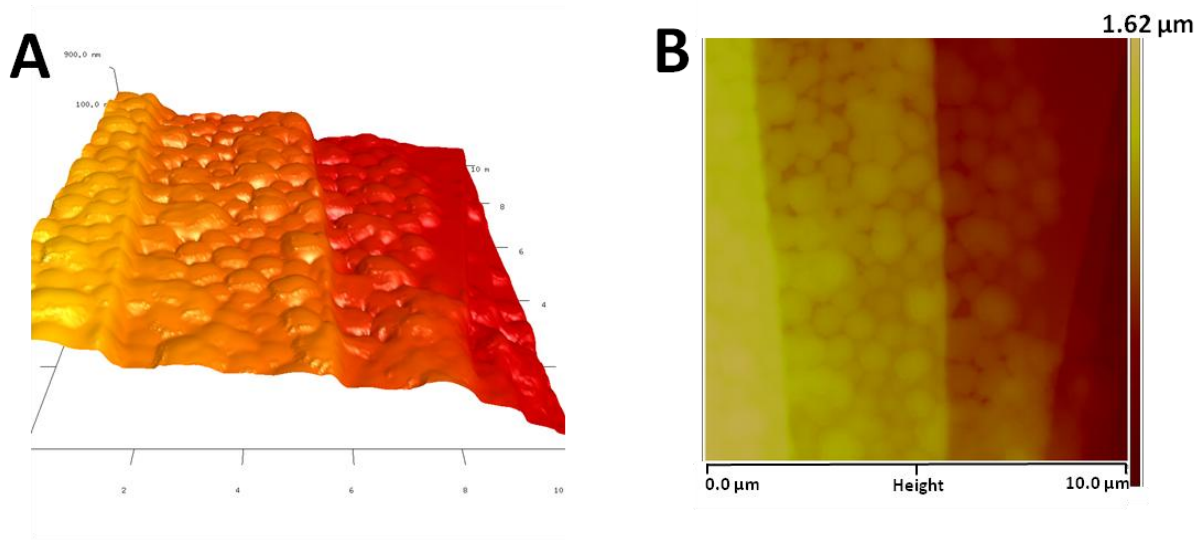


Figure 5.8. TM-AFM topography images of micro- and nano-sized particles. The particles of p(NIPAM-co-acrylic acid) contain 5 mol % acrylic acid content, cast on mica.

Optimization of the mechanical properties of the pDMA gels may require the use of particles like these, either as a doping agent or as a substrate for DOPA attachment chemistry. The carboxylic acid handle inherent in these particles is attractive for carbodiimide coupling as a possible synthetic pathway that has yet to be explored. The Silvion doped hydrogels presented herein have a number of obstacles to overcome and still requires development before it is ready for *in vivo* studies on animal models. But the improved air stability, preserved gel-sol reversibility, the economics of materials, truncated synthetic steps, and improvements on the mechanical properties as of late suggest that pDMA-based hydrogels are likely to ready for animal trials in the near future.

Concluding Remarks on Stimuli-Responsive Polymer Architectures

When investigating polymer systems in both the dry film state and in the hydrogel state, stimulated polymer architectural reorganization may operate; however, the effects are more drastic in the solvated state. In gels, the near-coil, solvated state of polymers affords more drastic effects with respect to mechanical property changes and rheological properties. In the dry state as in the case of polymers with spiropyran groups, molecular mobility is entropically unfavourable, and it is challenging to induce movement of chains due to the packing nature of nano phase separation. Consider Figure 1.3 again to when describing the entropy of mixing of a solvated polymer versus a dry block-copolymer film, devoid of solvent. Polymer-polymer and polymer-solvent systems offer different noncombinatorial free energies of solution, $\Delta G^{\text{M}}_{\text{noncomb}}$, which dictates the mobility of macromolecules in the UV-sensitive films and gels. Taking nature as a model for stimuli-induced changes in mechanical properties, it is likely there is a balance between hydrogel-like and solid polymer supports to afford macroscale changes in adhesion, tack, modulus, or other mechanical characteristics.

Natural stimuli-responsive systems like those mentioned in Chapter 1 operate using the cell as the building block for motion and the manufacturing center for enzyme production. Perhaps adopting the cell as the basic building block, in conjunction with macromolecules, we will afford some more interesting stimuli-responsive architectures in the near future. When attempting to design biomimetic polymeric devices that are intended to operate at fast time scales, we should consider what similar devices have already been developed by biological systems, from single cell organisms to higher mammals, even human beings.

Stimuli-responsive architectures surround us in the natural, *wild* world. Only just recently in time, a species on this planet has created a discipline of producing synthetic polymers through

chemistry. By comparison, the polymers of nature offer much complexity our synthetic analogues have only recently begun to adopt. However, the coming advancements in polymer chemistry will surely change those polymers used in commodity, high-tech, and medical markets. Necessity is truly the mother of invention, and the processes of natural selection in biological polymer systems have forged an impressive library of stimuli-responsive architectures. One of the many necessities for humanity will be to adopt and continually change our polymeric devices. Innovation to develop more useful, more dynamic, more sustainable, and still more economical polymers will always continue in the *wild*. Likely, humans will follow suit.

References

1. Eckhardt, S.; Brunetto, P. S.; Gagnon, J.; Priebe, M.; Giese, B.; Fromm, K. M. *Chem. Rev.* **2013**, 113, 4708-4754.
2. Fullenkamp, D. E.; Rivera, J. G.; Gong, Y.-k.; Lau, K. H. A.; He, L.; Varshney, R.; Messersmith, P. B. *Biomaterials* **2012**, 33, 3783-3791.
3. He, D.; Jones, A. M.; Garg, S.; Pham, A. N.; Waite, T. D. *The Journal of Physical Chemistry C* **2011**, 115, 5461-5468.
4. Brubaker, C. E.; Kissler, H.; Wang, L.-J.; Kaufman, D. B.; Messersmith, P. B. *Biomaterials* **2010**, 31, 420-427.
5. Ritchie, B. Molecular Therapeutics.
<http://moleculartpharma.com/www.moleculartpharma.com/Home.html> (November 23, 2014),
6. (SCOGS), S. C. o. G. S. History of the GRAS List and SCOGS Reviews.
<http://www.fda.gov/Food/IngredientsPackagingLabeling/GRAS/SCOGS/ucm084142.htm>
7. Holten-Andersen, N.; Harrington, M. J.; Birkedal, H.; Lee, B. P.; Messersmith, P. B.; Lee, K. Y. C.; Waite, J. H. *Proceedings of the National Academy of Sciences* **2011**, 108, 2651-2655.
8. Lee, H.; Dellatore, S. M.; Miller, W. M.; Messersmith, P. B. *Science* **2007**, 318, 426-430.
9. Hider, R. C.; Kong, X. *Natural Product Reports* **2010**, 27, 637-657.
10. Lee, B. P.; Dalsin, J. L.; Messersmith, P. B. *Biomacromolecules* **2002**, 3, 1038-1047.
11. Rosthauser, J. W.; Winston, A. *Macromolecules* **1981**, 14, 538-543.
12. Tulig, T. J.; Tirrell, M. *Macromolecules* **1981**, 14, 1501-1511.

13. Gu, Z.; Aimetti, A. A.; Wang, Q.; Dang, T. T.; Zhang, Y.; Veiseh, O.; Cheng, H.; Langer, R. S.; Anderson, D. G. *ACS Nano* **2013**, 7, 4194-4201.

APPENDIX A

NMR of Polymers 1 – 13

In macroinitiators of larger molecular weight, the initiator or end groups of the polymer often are overwhelmed by the larger, broad repeat unit signals and fade into the baseline.

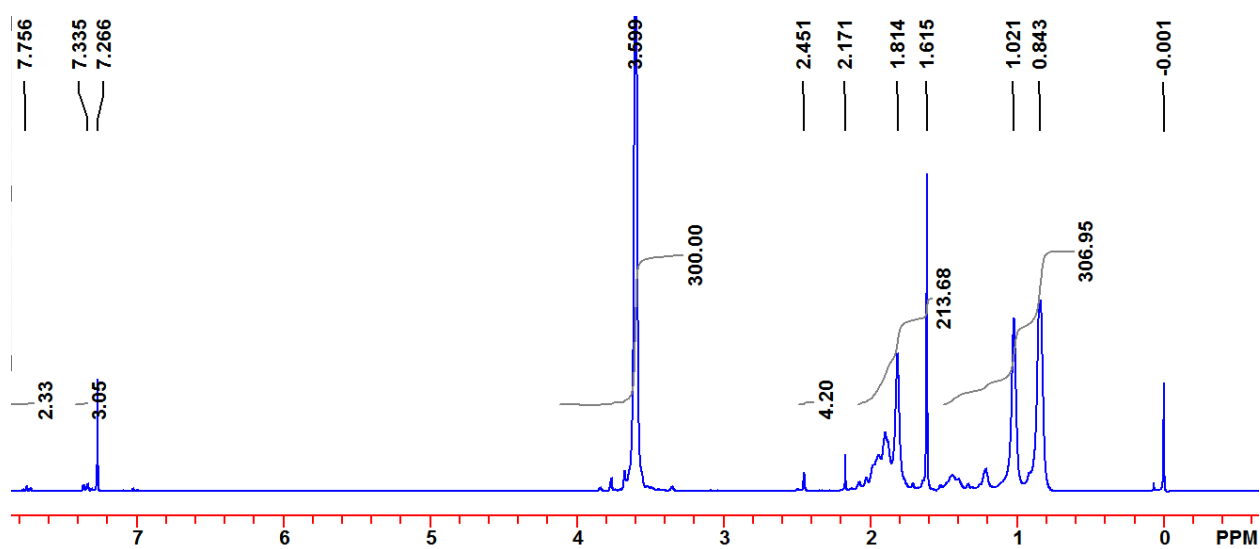


Figure A.1. NMR of *p*(MMA₇₇-Br/Cl) macroinitiator, Polymer 1

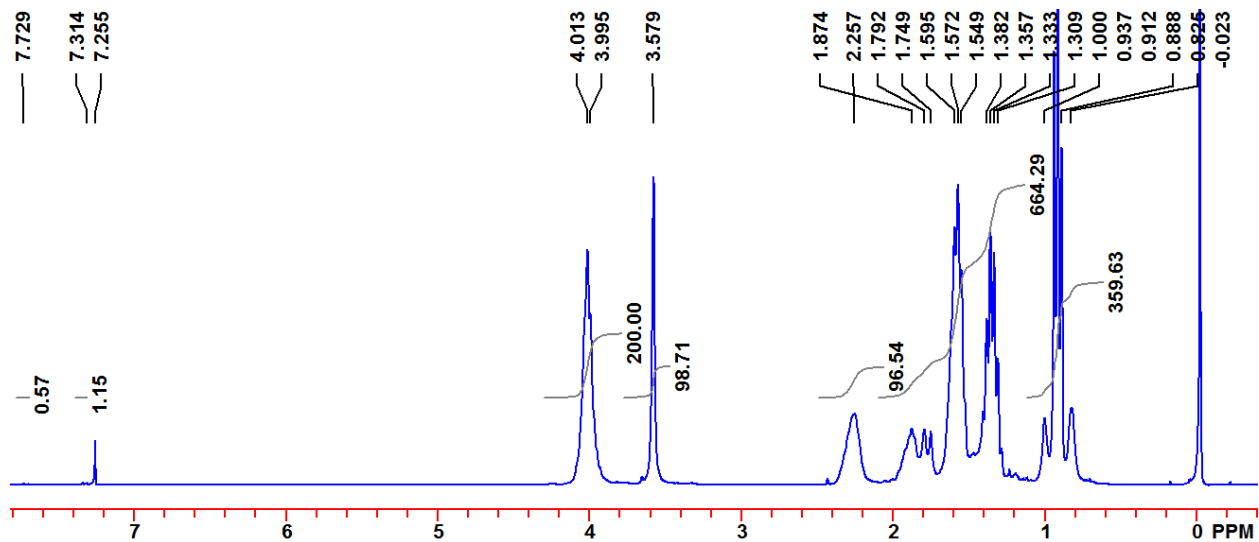


Figure A.2. NMR of $p(\text{MMA}_{77}\text{-}b\text{-nBA}_{142})$, Polymer 2

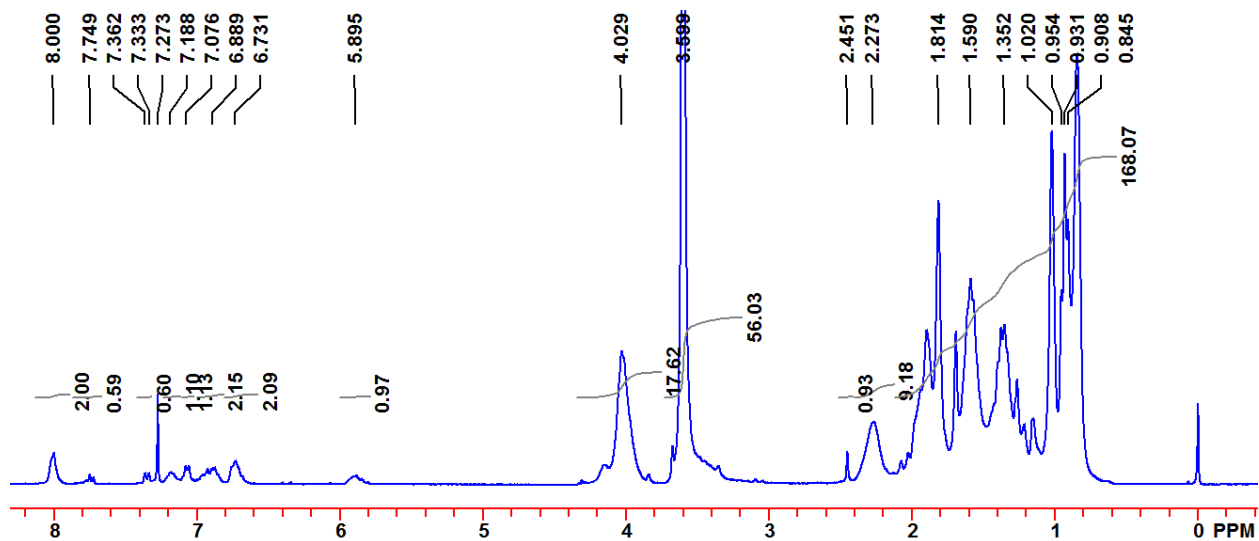


Figure A.3. NMR of $p(\text{MMA}_{77}\text{-}b\text{-nBA}_{38}\text{-co-SPA}_4)$ using $dNbp$, Polymer 3

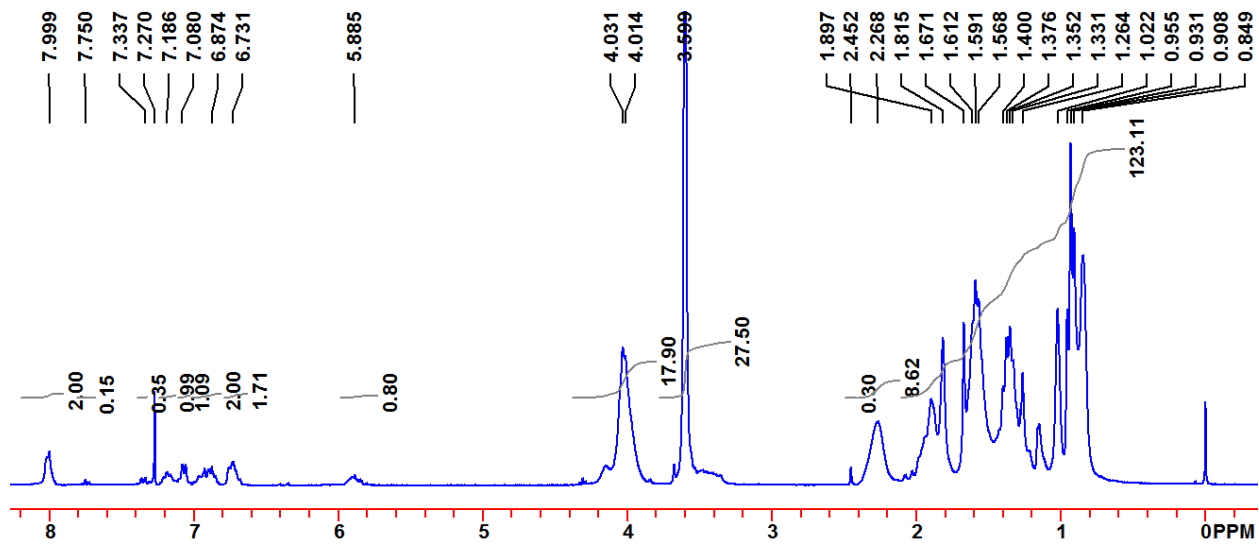


Figure A.4. NMR of $p(\text{MMA}_{77}\text{-}b\text{-nBA}_{52}\text{-co-SPA}_6)$ using PMDETA, Polymer 4

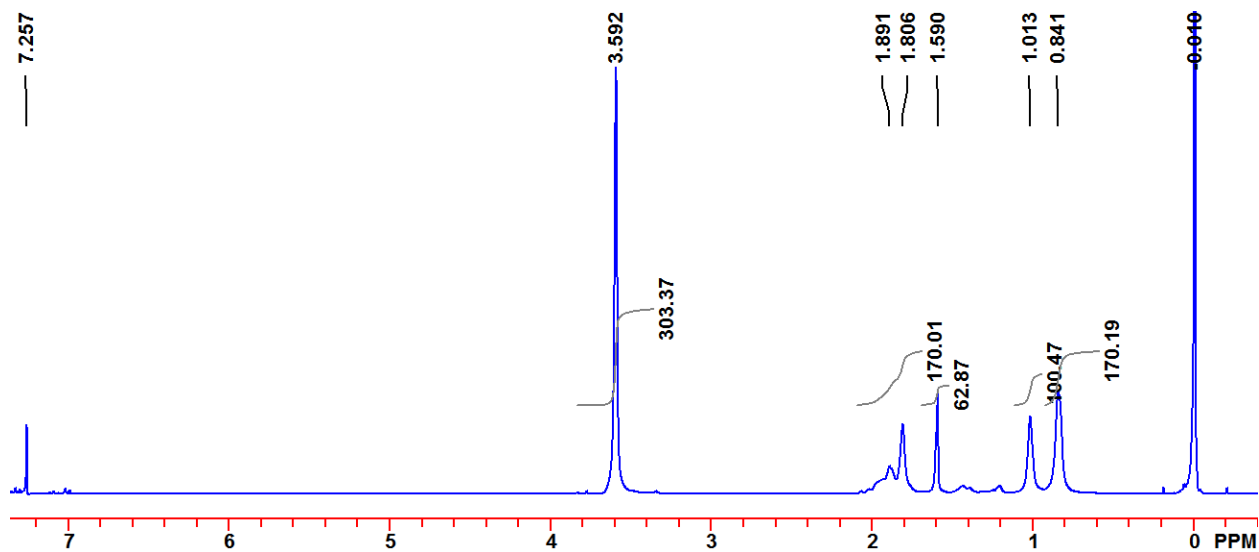


Figure A.5. NMR of $p(\text{Br-MMA}_{75}\text{-Br})$ macroinitiator, Polymer 5

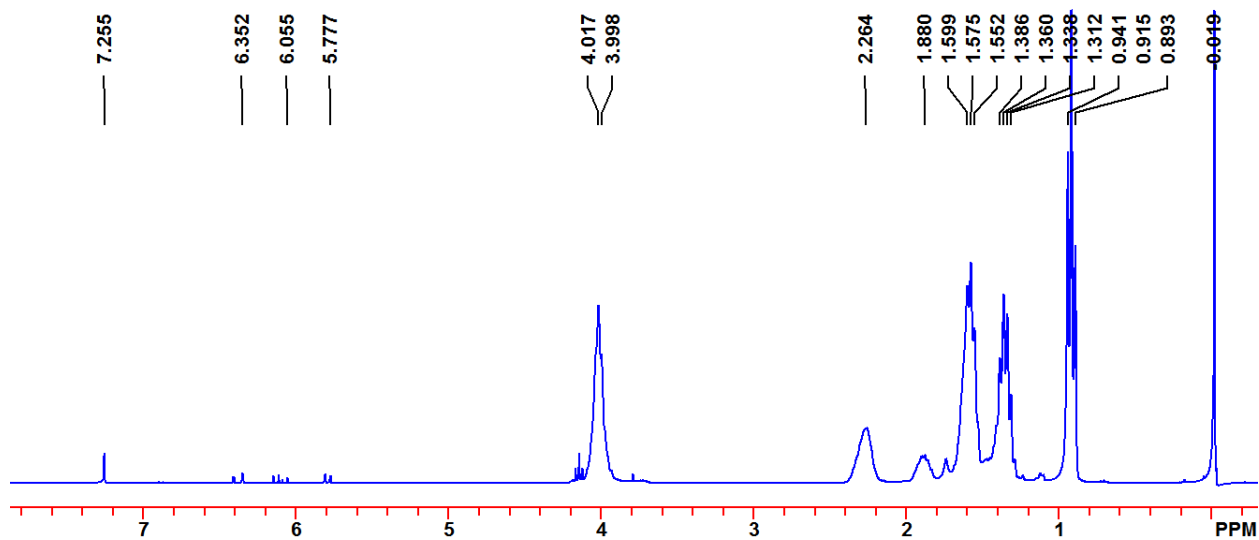


Figure A.6. NMR of $p(\text{Br-nBA}_{261}\text{-Br})$ macroinitiator, Polymer 6

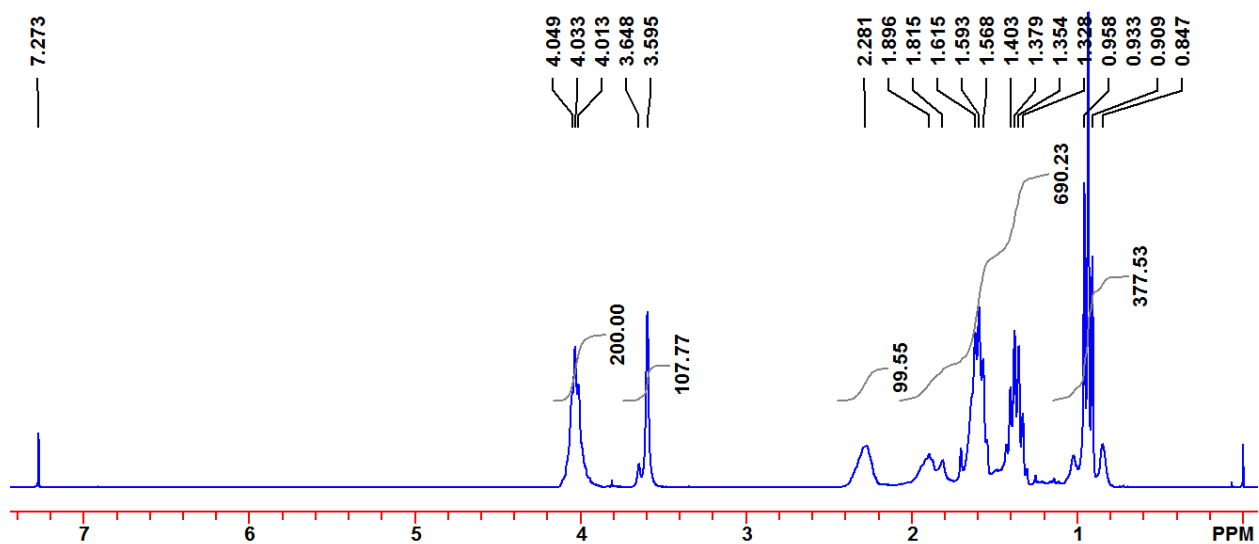


Figure A.7. NMR of $p(\text{nBA}_{380}\text{-}b\text{-MMA}_{137}\text{-co-nBA}_{14})$, Polymer 7

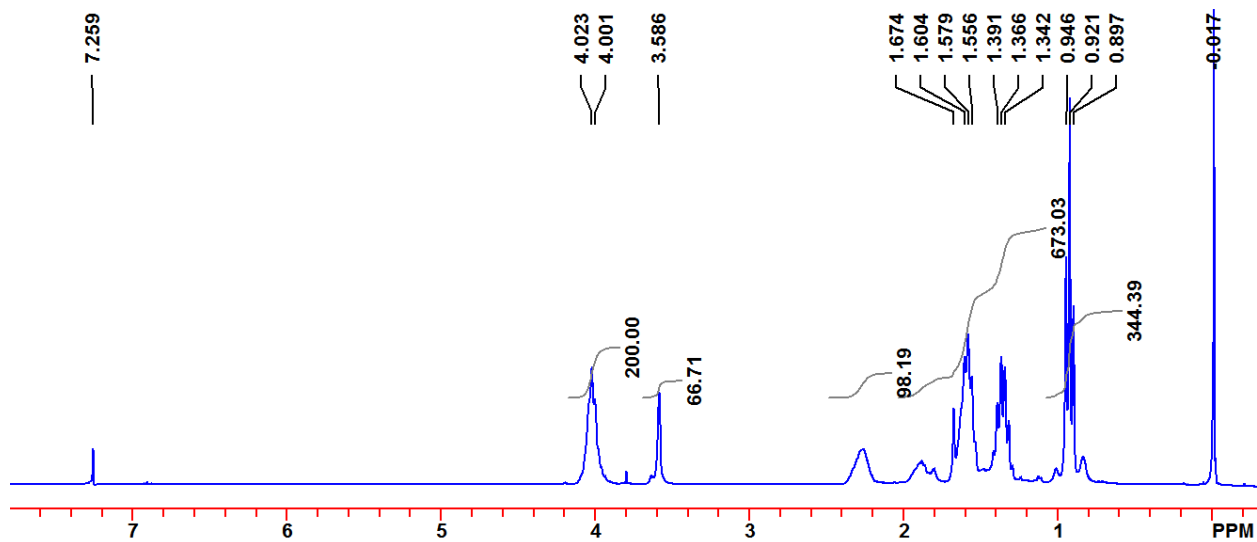


Figure A.8. NMR of $p(\text{MMA}_{50}\text{-co-}n\text{BA}_4\text{-}b\text{-}n\text{BA}_{310}\text{-}b\text{-MMA}_{50}\text{-co-}n\text{BA}_4)$, Polymer 8

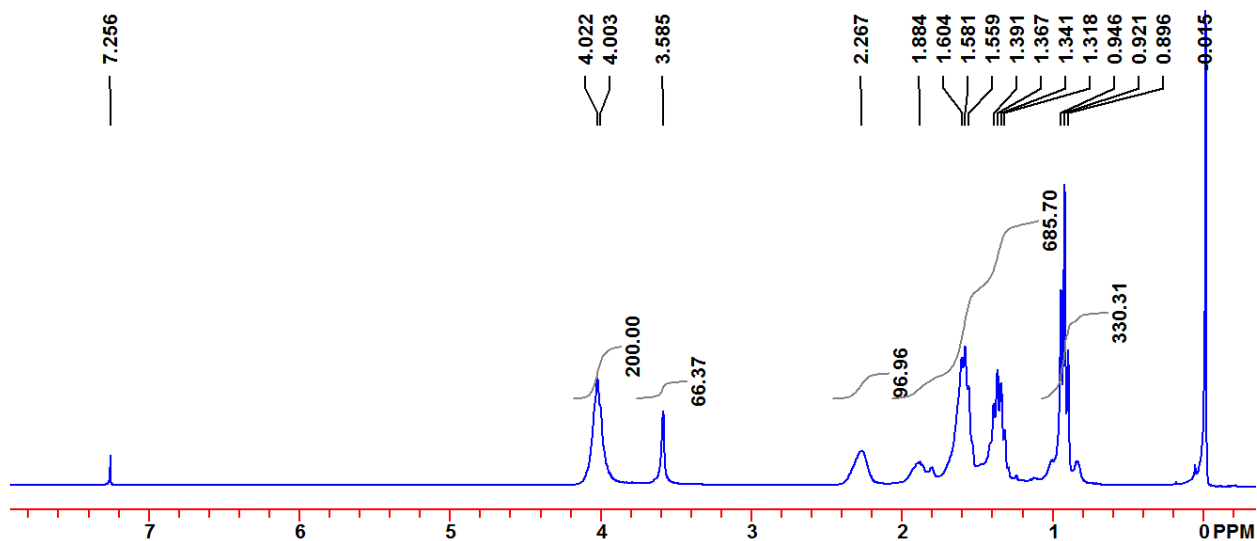


Figure A.9. NMR of $p(\text{MMA}_{22}\text{-}b\text{-}n\text{BA}_{261}\text{-}b\text{-MMA}_{22})$, Polymer 9

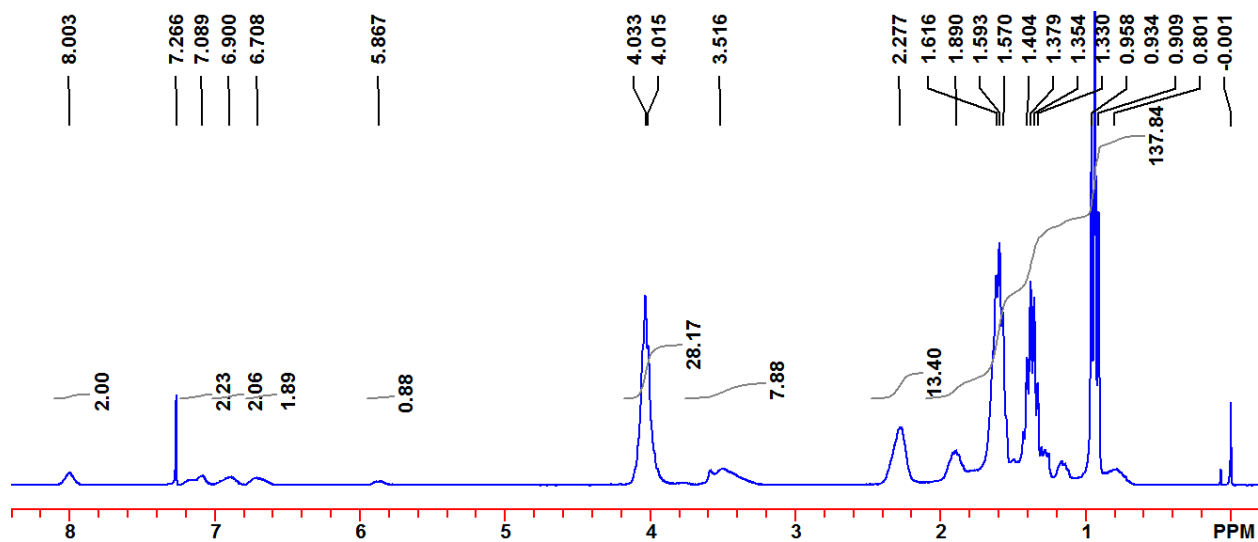


Figure A.10. NMR of $p(\text{MMA}_{30}\text{-co-SPMA}_{15}\text{-}b\text{-nBA}_{261}\text{-}b\text{-MMA}_{30}\text{-co-SPMA}_{15})$, Polymer 10

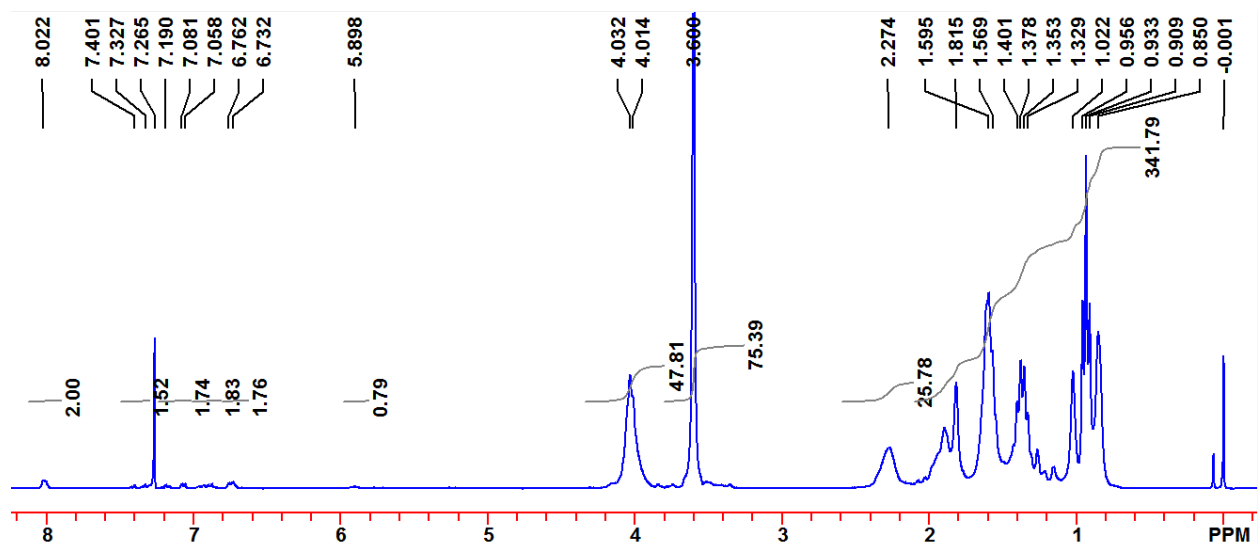


Figure A.11. NMR of $p(\text{nBA}_{68}\text{-co-SPA}_3\text{-}b\text{-MMA}_{75}\text{-}b\text{-nBA}_{68}\text{-co-SPA}_3)$, Polymer 11

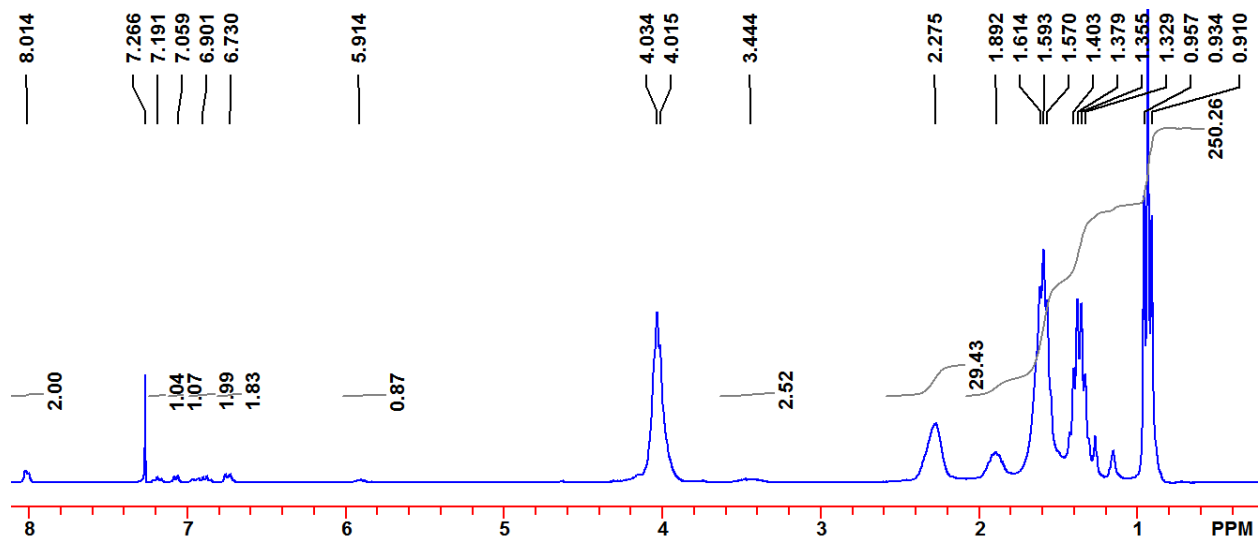


Figure A.13. NMR of $p(nBA-co-SPA)$, Polymer 12

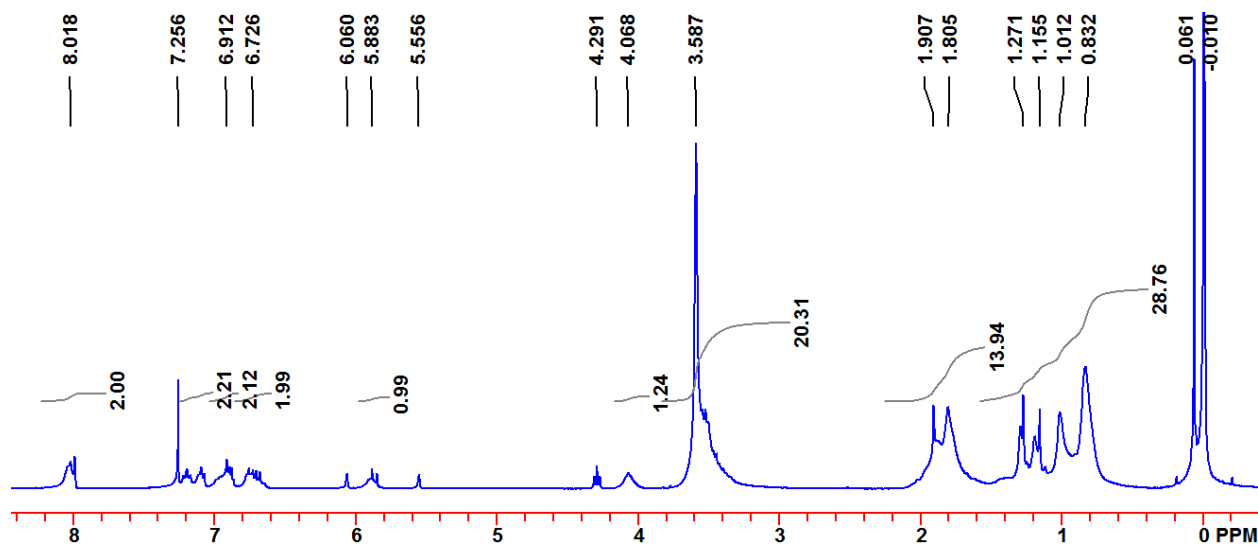


Figure A.13. NMR of $p(MMA-co-SPMA)$, Polymer 13

APPENDIX B

Calculations for the Hansen solubility parameter by group contribution

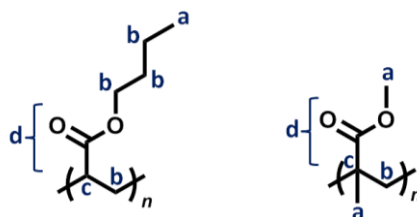


Figure B.1. First-order group assignments, blue, for p(nBA) and p(MMA).

Table B.1. The Hansen partial and total solubility parameters of p(nBA). The values were determined from the group contribution method and reference values found in the literature.¹

Group Contributions: p(nBA)				
1st-Order Groups	δ_D Contributions, C_i	δ_P Contributions, C_i	δ_H Contributions, C_i	Occurrences, N_i
a -CH ₃	-0.9714	-1.6448	-0.7813	1
b -CH ₂	-0.0269	-0.3045	-0.4119	4
c -CH<	0.645	0.6491	-0.2018	1
d -COO-	0.2039	3.4637	1.1389	1
Mpa^{1/2}				
$\delta_d = \sum N_i C_i + \sum M_j D_j + C =$	17.093			
$\delta_p = \sum N_i C_i + \sum M_j D_j + C =$	8.6084			
$\delta_h = \sum N_i C_i + \sum M_j D_j + C =$	6.4875			
δ_t	20.208		ρ (g·cm ⁻³)	1.087
			MW (g·mol⁻¹)	128.17

Table B.2. The Hansen partial and total solubility parameters of p(MMA). The values were determined from the group contribution method and reference values found in the literature.¹

Group Contributions: p(MMA)				
1st-Order Groups	δ_D Contributions, C_i	δ_P Contributions, C_i	δ_H Contributions, C_i	Occurrences, N_i
a -CH ₃	-0.9714	-1.6448	-0.7813	2
b -CH ₂	-0.0269	-0.3045	-0.4119	1
c >C<	1.2686	2.0838	0.0866	1

d	-COO-	0.2039	3.4637	1.1389	1
		Mpa^{1/2}			
$\delta_d = \sum N_i C_i + \sum M_j D_j + C =$		16.826			
$\delta_p = \sum N_i C_i + \sum M_j D_j + C =$		9.3118			
$\delta_h = \sum N_i C_i + \sum M_j D_j + C =$		7.2303			
δ_t		20.545		ρ (g·cm⁻³)	1.185
				MW (g·mol⁻¹)	100.121

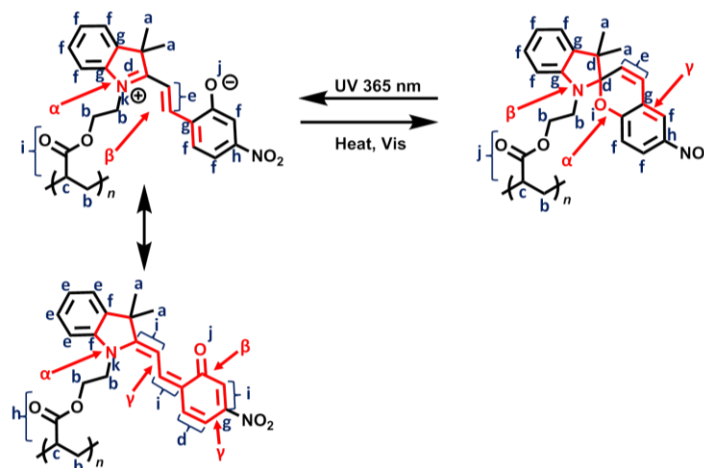


Figure B.2. First-order group assignment, blue, and second order group contributions, red, for p(SPA) – low δ_h , p(MCA) – low δ_h , and p(QA) – low δ .

Table B.3. The Hansen partial and total solubility parameters of p(SPA). The values were determined from the group contribution method and reference values found in the literature.¹

Group Contributions: p(SPA) – low δ_h					
	Ist-Order Groups	δ_D Contributions, C_i	δ_P Contributions, C_i	δ_H Contributions, C_i	Occurrences, N_i
a	-CH ₃	-0.9714	-0.72412	0.29901	2
b	-CH ₂	-0.0269	-0.1403	-0.1161	3
c	-CH<	0.645	0.58978	0.1386	1
d	>C<	1.2686	2.0838	0.0866	2
e	-CH=CH-	0.0048	-0.22864	0.48189	1
f	ArCH	0.1105	-0.19313	0.13532	7
g	ArC	0.8446	0.16369	-0.17405	4
h	ArCNO ₂	1.4195	4.4838	-0.7167	1
i	-O-	0.0472	-0.48942	0.0256	1
j	-COO-	0.2039	1.60913	0.37204	1
2nd-Order Groups					

α	ArC-O-C-	0.2568	0.8153	0.6092	1
β	>N-C _{cycle}	0.2218	-2.2018	-0.0452	1
	-C=C-C=C-	-0.1355	-3.5085	-1.0795	0
γ	AC(ACH _m) ₂ AC (ACH _h) ₂	-0.3751	-1.298	0.6844	1
		Mpa^{1/2}			
$\delta_d = \sum N_i C_i + \sum M_j D_j + C =$		24.6522			
$\delta_p = \sum N_i C_i + \sum M_j D_j + C =$		10.0294			
$\delta_h = \sum N_i C_i + \sum M_j D_j + C =$		8.4392		ρ (g·cm⁻³)	1.087
δ_t		27.9202		MW (g·mol⁻¹)	406.42

Table B.4. The Hansen partial and total solubility parameters of p(QA). The values were determined from the group contribution method and reference values found in the literature.¹

Group Contributions: p(QA) – low δ_h					
	1st-Order Groups	δ_D Contributions, C_i	δ_P Contributions, C_i	δ_H Contributions, C_i	Occurrences, N_i
a	-CH ₃	-0.9714	-0.72412	0.29901	2
b	-CH ₂	-0.0269	-0.1403	-0.1161	3
c	-CH<	0.645	0.58978	0.1386	1
	>C<	1.2686	2.0838	0.0866	0
d	-CH=CH-	0.0048	-0.22864	0.48189	1
d	ArCH	0.1105	-0.19313	0.13532	4
f	ArC	0.8446	0.16369	-0.17405	2
g	ArCNO ₂	1.4195	4.4838	-0.7167	1
	-O-	0.0472	-0.48942	0.0256	0
h	-COO-	0.2039	1.60913	0.37204	1
i	>C=CH	0.5372	1.22566	-0.030606	3
j	>C=O	-0.4343	0.7905	-0.05529	1
2nd-Order Groups					
	ArC-O-C-	0.2568	0.8153	0.6092	0
α	>N-C _{cycle}	0.2218	-2.2018	-0.0452	1
β	C _{cycle} =O	-0.2981	0.4497	-0.4794	1
γ	-C=C-C=C-	-0.1355	0.648793	-1.0795	2
		Mpa^{1/2}			
$\delta_d = \sum N_i C_i + \sum M_j D_j + C =$		20.5340			
$\delta_p = \sum N_i C_i + \sum M_j D_j + C =$		15.5112			
$\delta_h = \sum N_i C_i + \sum M_j D_j + C =$		5.8673		ρ (g·cm⁻³)	1.087
δ_t		26.3944		MW (g·mol⁻¹)	406.42

Table B.5. The Hansen partial and total solubility parameters of p(MCA). The values were determined from the group contribution method and reference values found in the literature.¹

Group Contributions: p(MCA - zwitterion) – low δ_h					
	1st-Order Groups	δ_D Contributions, C_i	δ_P Contributions, C_i	δ_H Contributions, C_i	Occurrences, N_i
a	-CH ₃	-0.9714	-0.72412	0.29901	2
b	-CH ₂	-0.0269	-0.1403	-0.1161	3
c	-CH<	0.645	0.58978	0.1386	1
d	>C=N-	-0.3074	-0.0012	-5.3956	1
e	-CH=CH-	0.0048	-0.22864	0.48189	1
f	ArCH	0.1105	-0.19313	0.13532	7
g	ArC	0.8446	0.16369	-0.17405	4
h	ArCNO ₂	1.4195	4.4838	-0.7167	1
	-O-	0.0472	-0.48942	0.0256	0
i	-COO-	0.2039	1.60913	0.37204	1
	>C=CH	0.5372	1.22566	-0.030606	0
	>C=O	-0.4343	0.7905	-0.05529	0
j	"-OH" (for phenolate)	-0.3462	1.83013	7.1908	1
k	"CH ₂ N" (for ammonium)	1.4681	0.65229	-1.03686	1
2nd-Order Groups					
	ArC-O-C-	0.2568	0.8153	0.6092	0
α	>N-C _{cycle}	0.2218	-2.2018	-0.0452	1
	C _{cycle} =O	-0.2981	0.4497	-0.4794	0
β	-C=C-C=C-	-0.1355	0.648793	-1.0795	1
		Mpa^{1/2}			
	$\delta_d = \sum N_i C_i + \sum M_j D_j + C =$	22.6255			
	$\delta_p = \sum N_i C_i + \sum M_j D_j + C =$	12.1744			
	$\delta_h = \sum N_i C_i + \sum M_j D_j + C =$	8.3895		ρ (g·cm ⁻³)	1.087
	δ_t	27.0208		MW (g·mol ⁻¹)	406.42

Table B.6. The Hansen partial and total solubility parameters of p(SPMA). The values were determined from the group contribution method and reference values found in the literature.¹

Group Contributions: p(SPMA) – low δ_h					
	1st-Order Groups	δ_D Contributions, C_i	δ_P Contributions, C_i	δ_H Contributions, C_i	Occurrences, N_i
a	-CH ₃	-0.9714	-0.72412	0.29901	3
b	-CH ₂	-0.0269	-0.1403	-0.1161	3
	-CH<	0.645	0.58978	0.1386	0
c	>C<	1.2686	2.0838	0.0866	2
d	-CH=CH-	0.0048	-0.22864	0.48189	1

e	ArCH	0.1105	-0.19313	0.13532	7
f	ArC	0.8446	0.16369	-0.17405	4
g	ArCNO ₂	1.4195	4.4838	-0.7167	1
h	-O-	0.0472	-0.48942	0.0256	1
i	-COO-	0.2039	1.60913	0.37204	1
2nd-Order Groups					
α	ArC-O-C-	0.2568	0.8153	0.6092	1
β	>N-C _{cycle}	0.2218	-2.2018	-0.0452	1
	-C=C-C=C-	-0.1355	-3.5085	-1.0795	0
γ	AC(ACH _m) ₂ AC (ACH _n) ₂	-0.3751	-1.298	0.6844	1
			Mpa^{1/2}		
		$\delta_d = \sum N_i C_i + \sum M_j D_j + C =$	22.7962		
		$\delta_p = \sum N_i C_i + \sum M_j D_j + C =$	10.9260		
		$\delta_h = \sum N_i C_i + \sum M_j D_j + C =$	10.3635	ρ (g·cm⁻³)	1.185
		δ_i	27.3212	MW (g·mol⁻¹)	420.45

Table B.7. The Hansen partial and total solubility parameters of p(QMA). The values were determined from the group contribution method and reference values found in the literature.¹

Group Contributions: p(QMA) – low δ_h					
	1st-Order Groups	δ_D Contributions, C_i	δ_P Contributions, C_i	δ_H Contributions, C_i	Occurrences, N_i
a	-CH ₃	-0.9714	-0.72412	0.29901	3
b	-CH ₂	-0.0269	-0.1403	-0.1161	3
	-CH<	0.645	0.58978	0.1386	0
	>C<	1.2686	2.0838	0.0866	0
c	-CH=CH-	0.0048	-0.22864	0.48189	1
d	ArCH	0.1105	-0.19313	0.13532	4
e	ArC	0.8446	0.16369	-0.17405	2
8	ArCNO ₂	1.4195	4.4838	-0.7167	1
	-O-	0.0472	-0.48942	0.0256	0
f	-COO-	0.2039	1.60913	0.37204	1
g	>C=CH	0.5372	1.22566	-0.030606	3
h	>C=O	-0.4343	0.7905	-0.05529	1
2nd-Order Groups					
	ArC-O-C-	0.2568	0.8153	0.6092	0
α	>N-C _{cycle}	0.2218	-2.2018	-0.0452	1
β	C _{cycle} =O	-0.2981	0.4497	-0.4794	1
γ	-C=C-C=C-	-0.1355	0.648793	-1.0795	2
			Mpa^{1/2}		
		$\delta_d = \sum N_i C_i + \sum M_j D_j + C =$	18.9176		
		$\delta_p = \sum N_i C_i + \sum M_j D_j + C =$	14.1973		

$\delta_h = \sum N_i C_i + \sum M_j D_j + C =$	6.0277	ρ (g·cm ⁻³)	1.185
δ_t	24.4084	MW (g·mol ⁻¹)	420.45

Table B.8. The Hansen partial and total solubility parameters of p(MCA). The values were determined from the group contribution method and reference values found in the literature.¹

Group Contributions: p(MCMA - zwitterion) – low δ_h					
	1st-Order Groups	δ_D Contributions, C _i	δ_P Contributions, C _i	δ_H Contributions, C _i	Occurrences, N _i
a	-CH ₃	-0.9714	-1.6448	-0.7813	3
b	-CH ₂	-0.0269	-0.3045	-0.4119	3
	-CH<	0.645	0.6491	-0.2018	0
c	>C=N-	-0.3074	-0.0012	-5.3956	1
d	-CH=CH-	0.0048	-0.2984	-0.04	1
e	ArCH	0.1105	-0.5303	-0.4305	7
f	ArC	0.8446	0.6187	0.0084	4
g	ArCNO ₂	1.4195	4.4838	-0.7167	1
	-O-	0.0472	3.3432	0.0256	0
h	-COO-	0.2039	3.4637	1.1389	1
	>C=CH	0.5372	-0.9024	-1.8872	0
	>C=O	-0.4343	0.7905	1.8147	0
i	"-OH" (for phenolate)	-0.3462	1.1404	7.1908	1
j	"CH ₂ N" (for ammonium)	1.4681	2.8345	1.2505	1
2nd-Order Groups					
	ArC-O-C-	0.2568	0.8153	0.6092	0
α	>N-C _{cycle}	0.2218	-2.2018	-0.0452	1
	C _{cycle} =O	-0.2981	0.4497	-0.4794	0
β	-C=C-C=C-	-0.1355	-3.5085	-1.0795	1
		Mpa^{1/2}			
	$\delta_d = \sum N_i C_i + \sum M_j D_j + C =$	20.0091			
	$\delta_p = \sum N_i C_i + \sum M_j D_j + C =$	10.8605			
	$\delta_h = \sum N_i C_i + \sum M_j D_j + C =$	8.5499			
	δ_t	25.1482			
				ρ (g·cm ⁻³)	1.185
				MW (g·mol ⁻¹)	420.45

Table B.9. Example Hansen partial and total solubility parameters of the mixed block of Polymer 11. The average dispersion, polar, and hydrogen bonding parameters were determined by Equation 2.3 for this polymer, p(nBA₆₈-co-SPA₃-b-MMA₇₅-b-nBA₆₈-co-SPA₃). The values were determined from the group contribution method and reference values found in the literature.¹

pMMA		pnBA		p(MCA-zwitterion)		Mixed Block	
	Mpa ^{1/2}		Mpa ^{1/2}		Mpa ^{1/2}		δ_{average} Mpa ^{1/2}
δ_d	16.825	δ_d	17.093	δ_d	22.294	δ_d	17.493
δ_p	9.3118	δ_p	8.6084	δ_p	12.754	δ_p	8.9276
δ_h	7.2303	δ_h	6.4875	δ_h	7.9836	δ_h	6.6027
δ_t	20.545	δ_t	20.208	δ_t	26.897	δ_t	20.720
ρ (g·cm ⁻³)	1.185	ρ (g·cm ⁻³)	1.087	ρ (g·cm ⁻³)	1.087	ρ (g·cm ⁻³)	1.087
MW (g·mol ⁻¹)	100.121	MW (g·mol ⁻¹)	128.17	MW (g·mol ⁻¹)	406.42	MW (g·mol ⁻¹)	149.5926
$\Phi_{\text{B (MMA)}}$	0.4238	$\Phi_{\text{b, nBA}}$	0.923	$\Phi_{\text{a, SPA}}$	0.077	$\Phi_{\text{A (nBA-co-SPA)}}$	0.5762

Table B.10. First-order group contributions for δ_D , δ_P , and δ_H . Data provided by Stefanis and Panayiotou.¹ Reprinted with permission from *International Journal of Thermophysics* **2008**, 29, 568-585. Copyright 2014 Clearance Center, Inc.

First-order groups	δ_d	δ_p	δ_{hb}	Examples (Occurrences)
-CH ₃	-0.9714	-1.6448	-0.7813	Propane (2)
-CH ₂	-0.0269	-0.3045	-0.4119	Butane (2)
-CH<	0.6450	0.6491	-0.2018	Isobutane (1)
>C<	1.2686	2.0838	0.0866	Neopentane (1)
CH ₂ =CH-	-1.0585	-2.0035	-1.2985	Propylene (1)
-CH=CH-	0.0048	-0.2984	-0.0400	cis-2-Butene (1)
CH ₂ =C<	-0.4829	-0.7794	-0.8260	Isobutene (1)
-CH=C<	0.5372	-0.9024	-1.8872	2-Methyl-2-butene (1)
>C=C<	0.3592	1.0526	-15.4659	2,3-Dimethyl-2-butene (1)
CH ₂ =C=CH-	-1.6518	***	-0.9980	1,2-Butadiene (1)
CH≡C-	0.2320	-1.3294	1.0736	Propyne (1)
C≡C	-0.2028	-0.7598	-1.1083	2-Butyne (1)
ACH	0.1105	-0.5303	-0.4305	Benzene (6)
AC	0.8446	0.6187	0.0084	Naphthalene (2)
ACCH ₃	0.2174	-0.5705	-1.1473	Toluene (1)
ACCH ₂ -	0.6933	0.6517	-0.1375	m-Ethyltoluene (1)
CH ₃ CO	-0.3551	2.3192	-1.3078	Methyl ethyl ketone (1)
CH ₂ CO	0.6527	3.7328	-0.5344	Cyclopentanone (1)
CHO (aldehydes)	-0.4030	3.4734	0.1687	1-Butanal (1)
COOH	-0.2910	0.9042	3.7391	Vinyl acid (1)
CH ₃ COO	-0.5401	-0.3970	1.5826	Ethyl acetate (1)
CH ₂ COO	0.2913	3.6462	1.2523	Methyl propionate (1)
HCOO	***	1.9308	2.1202	n-Propyl formate (1)
COO	0.2039	3.4637	1.1389	Ethyl acrylate (1)
OH	-0.3462	1.1404	7.1908	Isopropanol (1)
ACOH	0.5288	1.1010	6.9580	Phenol (1)
CH ₃ O	-0.5828	0.1764	0.1460	Methyl ethyl ether (1)
CH ₂ O	0.0310	0.8826	-0.1528	Ethyl vinyl ether (1)
CHO (ethers)	0.8833	1.6853	0.4470	Diisopropyl ether (1)
C ₂ H ₅ O ₂	-0.1249	3.6422	8.3579	2-Methoxy-ethanol (1)
CH ₂ O (cyclic)	0.2753	0.1994	-0.1610	1,4-Dioxane (2)
CH ₂ NH ₂	-0.5828	1.4084	2.5920	1-Amino-2-propanol (1)
CHNH ₂	0.0112	-1.1989	0.3818	Isopropylamine (1)
CH ₃ NH	***	0.6777	5.6646	n-Methylaniline (1)
CH ₂ NH	0.8116	0.9412	1.3400	di-n-Propylamine (1)
CH ₃ N	0.8769	1.2046	1.6062	Trimethylamine (1)
CH ₂ N	1.4681	2.8345	1.2505	Triethylamine (1)
ACNH ₂	1.6987	1.6761	4.5274	Aniline (1)
CONH ₂	-0.0689	6.0694	5.2280	2-Methacrylamide (1)
CON(CH ₃) ₂	0.4482	5.7899	3.0020	n,n-Dimethylacetamide (1)
CH ₂ SH	1.2797	-0.8223	4.4646	n-Butyl mercaptan (1)
CH ₃ S	***	0.4944	-1.4861	Methyl ethyl sulfide (1)
CH ₂ S	1.0595	0.7530	-0.2287	Diethyl sulfide (1)
I	0.7797	0.6777	0.2646	Isopropyl iodide (1)
Br	0.5717	0.6997	-1.0722	2-Bromopropane (1)
CH ₂ Cl	0.2623	0.5970	-0.5364	n-Butyl chloride (1)
CHCl	0.4462	2.8060	-1.4125	Isopropyl chloride (1)
CCl	2.7576	2.0406	0.1101	t-Butyl chloride (1)
CHCl ₂	1.1797	1.8361	-3.2861	1,1-Dichloropropane (1)
CCl ₂	0.3653	0.1696	-1.4334	Pentachlorocyclopropane (2)
CCl ₃	***	1.2777	-2.6354	Benzotrichloride (1)
ACCl	0.8475	-0.0339	-0.7840	m-Dichlorobenzene (2)
ACF	0.1170	0.1856	-0.7182	Fluorobenzene (1)

First-order groups	δ_d	δ_p	δ_{hb}	Examples (Occurrences)
Cl-(C=C)	0.2289	2.3444	3.8893	2,3-Dichloropropene (1)
CF ₃	-0.2293	-1.9735	-1.4665	Perfluorohexane (2)
CH ₂ NO ₂	***	6.8944	-1.2861	1-Nitropropane (1)
CHNO ₂	***	8.0347	-2.3167	2-Nitropropane (1)
ACNO ₂	1.4195	4.4838	-0.7167	Nitrobenzene (1)
CH ₂ CN	-0.3392	6.5341	-0.8892	<i>n</i> -Butyronitrile (1)
CF ₂	-0.9729	***	***	Perfluoromethylcyclohexane (5)
CF	0.1707	***	***	Perfluoromethylcyclohexane (1)
F (except as above)	-0.7069	***	***	2-Fluoropropane (1)
CH ₂ =C=C<	-0.2804	***	-1.9167	3-Methyl-1,2-butadiene (1)
O (except as above)	0.0472	3.3432	0.0256	Divinyl ether (1)
Cl (except as above)	0.2256	1.8711	-0.3295	Hexachlorocyclopentadiene (2)
>C=N-	-0.3074	-0.0012	-5.3956	2,4,6-Trimethylpyridine (1)
-CH=N-	0.9672	1.9728	0.7668	Isoquinoline (1)
NH (except as above)	***	0.0103	2.2086	Dibenzopyrrole (1)
CN (except as above)	0.0861	6.5331	-0.6849	<i>cis</i> -Crotonitrile (1)
O=C=N-	-0.1306	1.6102	4.0461	<i>n</i> -Butyl isocyanate (1)
SH (except as above)	1.0427	1.9813	4.8181	2-Mercaptobenzothiazole (1)
S (except as above)	1.4899	9.2072	-0.6250	Thiophene (1)
SO ₂	1.5502	11.1758	0.1055	Sulfolene (1)
>C=S	0.7747	0.0683	3.4080	<i>n</i> -Methylthiopyrrolidone (1)
>C=O (except as above)	-0.4343	0.7905	1.8147	Anthraquinone (2)
N (except as above)	1.5438	2.5780	1.1189	Triphenylamine (1)

*** The specific group contributions to this delta parameter are not available

Table B.11. Second-order group contributions for δ_D , δ_P , and δ_H . Data provided by Stefanis and Panayiotou.¹ Reprinted with permission from *International Journal of Thermophysics* **2008**, 29, 568-585. Copyright 2014 Clearance Center, Inc..

Second-order groups	δ_d	δ_p	δ_{hb}	Examples (Occurrences)
(CH ₃) ₂ -CH-	0.0460	0.0019	0.3149	Isobutane (1)
(CH ₃) ₃ -C-	-0.0738	1.1881	-0.2966	Neopentane (1)
ring of 5 carbons	-0.6681	-2.3430	-0.3079	Cyclopentane (1)
ring of 6 carbons	-0.3874	-3.6432	***	Cyclohexane (1)
-C=C-C=C-	-0.1355	-3.5085	-1.0795	1,3-Butadiene (1)
CH ₃ -C=	-0.0785	0.3316	0.3875	Isobutene (2)
-CH ₂ -C=	-0.3236	-2.3179	-0.5836	1-Butene (1)
>C(H or C)-C=	-0.2798	***	-1.1164	3-Methyl-1-butene (1)
string in cyclic	-0.1945	***	***	Ethylcyclohexane (1)
CH ₃ (CO)CH ₂ -	-0.0451	-0.3383	-0.4083	Methyl ethyl ketone (1)
C _{cyclic} =O	-0.2981	0.4497	-0.4794	Cyclopentanone (1)
ACCOOH	-0.2293	-0.6349	-0.9030	Benzoic acid (1)
>C(H or C)-COOH	***	-0.2187	1.1460	Isobutyric acid (1)
CH ₃ (CO)OC(H or C) <	-0.5220	-0.0652	0.3085	Isopropyl acetate (1)
(CO)C(H ₂)COO	***	-2.3792	0.8412	Ethyl acetoacetate (1)
(CO)O(CO)	-0.2707	-1.0562	1.6335	Acetic anhydride (1)
ACHO	0.3772	-1.8110	-1.0096	Benzaldehyde (1)
>CHOH	0.1123	0.2564	-0.1928	2-Propanol (1)
>C<OH	-0.0680	0.1075	1.2931	Tert-Butanol (1)
-C(OH)C(OH)-	***	0.6419	0.3870	1,2-Propanediol (1)
-C(OH)C(N)	-0.0809	0.5683	-0.6326	1-Amino-2-propanol (1)
C _{cyclic} -OH	-0.0876	-3.5220	0.5914	Cyclohexanol (1)
C-O-C=C	0.2063	0.6080	1.1344	Ethyl vinyl ether (1)
AC-O-C	0.2568	0.8153	0.6092	Methyl phenyl ether (1)
>N(H or C)(in cyclic)	0.2218	-2.2018	-0.0452	Cyclopentimine (1)
-S-(in cyclic)	0.4892	0.3040	0.2297	Tetrahydrothiophene (1)
ACBr	0.1234	-0.4495	0.3397	Bromobenzene (1)
(C=C)-Br	-0.4059	-0.0024	-1.1304	2-Bromopropene (1)
ring of 3 carbons	0.0200	1.8288	-0.8073	Cyclopropane (1)
ACCOO	-0.1847	0.4059	-0.1921	Methyl benzoate (1)
AC(ACH _m) ₂ AC(ACH _n) ₂	-0.3751	-1.2980	0.6844	Naphthalene (1)
O _{cyclic} -C _{cyclic} =O	0.2468	2.7501	0.1220	Diketene (1)
AC-O-AC	-0.5646	-3.4329	2.0830	Diphenyl ether (1)
C _{cyclic} H _m =N _{cyclic} -C _{cyclic} H _n =C _{cyclic} H _p	0.7002	0.0691	-2.7661	2,6-Dimethylpyridine (1)
N _{cyclic} H _m -C _{cyclic} =O	0.2956	2.8958	1.3125	2-Pyrrolidone (1)
-O-CH _m -O-CH _n -	0.0839	0.3451	0.3767	Methylal (1)
C(=O)-C-C(=O)	-0.4862	-0.4888	1.2482	2,4-Pentanedione (1)

*** The specific group contributions to this delta parameter are not available

Table B.12. First-order group contributions for δ_D , δ_P , and δ_H .- low δ_P . For low δ_P , ($\delta_P < 3$ MPa^{1/2}), and the hydrogen-bonding partial solubility parameter, δ_{hb} ($\delta_{hb} < 3$ MPa^{1/2}). Reprinted with permission from *International Journal of Thermophysics* **2008**, 29, 568-585. Copyright 2014 Clearance Center, Inc.

First-order groups	Low δ_P	Low δ_{hb}
-CH ₃	-0.72412	0.29901
-CH ₂	-0.14030	-0.11610
-CH<	0.58978	0.1386
CH ₂ =CH-	-0.29774	1.35521
-CH=CH-	-0.22864	0.48189
CH ₂ =C<	0.64816	0.11148
-CH=C<	1.22566	-0.03066
>C=C<	***	-0.12117
CH ₂ =C=CH-	-0.32258	***
CH≡C-	-0.74895	0.43846
C≡C	***	-0.35107
ACH	-0.19313	0.13532
AC	0.16369	-0.17405
ACCH ₃	-0.47724	-0.28733
ACCH ₂ -	-0.33086	-0.88084
ACCH<	0.86718	-1.44666
CH ₃ COO	1.71923	***
CH ₂ COO	2.16274	***
COO	1.60913	0.37204
OH	1.84013	***
CH ₃ O	-0.40320	***
CH ₂ O	***	***
CHO	***	-0.40667
CH ₂ O (cyclic)	-0.33305	***
CH ₂ NH ₂	***	***
CH ₂ NH	0.83214	***
CHNH	1.25999	***
CH ₃ N	***	-0.17004
CH ₂ N	0.65229	-1.03686
CH ₂ S	***	0.14606
CH ₂ Cl	***	0.48952
CHCl	***	0.12996
CHCl ₂	***	0.52541
ACCl	-0.10778	0.44238
CCl ₂ F	***	***
ACF	***	-0.37183
Cl-(C=C)	***	0.66062
CF ₃	***	-0.08871
CH ₂ =C=C<	1.20154	***
O (except as above)	-0.48942	***
Cl (except as above)	***	1.12515
S (except as above)	0.11058	***
>C=O (except as above)	***	-0.05529

Table B.13. Second-order group contributions for δ_D , δ_P , and δ_H - low δ_P . For low δ_p , ($\delta_p < 3$ MPa^{1/2}), and the hydrogen-bonding partial solubility parameter, δ_{hb} ($\delta_{hb} < 3$ MPa^{1/2}). Reprinted with permission from *International Journal of Thermophysics* **2008**, 29, 568-585. Copyright 2014 Clearance Center, Inc.

Second-order groups	Low δ_p	Low δ_{hb}
(CH ₃) ₂ -CH-	0.200694	10 ⁻⁸
Ring of 5 carbons	-0.897912	0.19438
Ring of 6 carbons	-0.956852	2 10 ⁻⁸
-C=C-C=C-	0.648793	***
CH ₃ -C=	-0.008375	-0.061370
-CH ₂ -C=	0.011009	0.06599
>C(H or C)-C=	-0.39720	0.342229
String in cyclic	***	-0.280859
ACCOO	0.491153	10 ⁻⁸
AC(ACH _m) ₂ AC(ACH _n) ₂	0.013012	0.086424
-O-CH _m -O-CH _n -	0	***

References

1. Stefanis, E.; Panayiotou, C. *International Journal of Thermophysics* **2008**, 29, 568-585.

APPENDIX C

Supporting Information for pDMA Hydrogels

Materials

Water (18 M Ω), dichloromethane, chloroform, hexane, and 2-propanol were degassed with argon or nitrogen sparging prior to use. Toluene and dimethyl sulfoxide were used as received (Fisher). *N*-isopropylacrylamide was recrystallized from 60:40 toluene:hexane. 2,2'-Azobis(isobutyronitrile) (AIBN, Sigma-Aldrich), acrylamide (AcAm, EMD), dopamine hydrochloride (Alfa Aesar), Iron(III) chloride hexahydrate (J.T.Baker), diphenyliodonium chloride (Alfa Aesar), and sodium bicarbonate (Fisher) were used as received. Quartz slides (25 X 75 X 1 mm) were washed and sonicated with acetone, water, and 2-propanol and dried under a stream of nitrogen prior to use.

Synthesis of N-(3,4-dihydroxyphenethyl)methacrylamide monomer modified from Langmuir, 2009, 25, 6607-6612,

10.0 g of NaB₄O₇ (26.22 mmol) and 4.0 g of NaHCO₃ (47.61 mmol) were first dissolved in 100 mL of 18 M Ω water, displaying some insolubility. This solution was degassed for 45 minutes with nitrogen, after which 5.0 g (32.64 mmol) of dopamine HCl was added to the mixture and allowed to stir under nitrogen atmosphere. A separate a solution of 4.7 mL (31.71 mmol) of methacrylic anhydride in 25 mL of degassed THF was prepared and added dropwise. The pH of the reaction mixture was monitored periodically with pH paper and maintained slightly basic (pH 8-9) by addition of degassed 1.0 M NaOH. Once all the methacrylic anhydride

solution was added, the solution was allowed to stir for 17 hours at room temperature, resulting in a light brown solution. This solution was washed with two 50 mL portions of ethyl acetate and the resulting aqueous layer was filtered. The filtrate was acidified to pH 2 with 6M HCl. This mixture was extracted three times with 50 mL of ethyl acetate, dried with MgSO₄, condensed down to approximately 20 mL under reduced pressure, and precipitated into 0°C hexane. The white precipitate was collected and recrystallized from boiling ethyl acetate to afford white crystals collected by vacuum filtration and dried under vacuum in 53% isolatable yield. ¹H NMR (300 MHz, DMSO-d₆, δ): 8.740 (s, 1H, ArOH), 8.625 (s, 1H, ArOH), 7.927 (t, *J* = 5.4, 1H, NH), 6.630 (d, *J* = 7.9, 1H, ArH), 6.578 (d, *J* = 2.0, 1H, ArH), 6.439 (dd, *J*₁ = 7.9, *J*₂ = 2.0, 1H), 5.616 (t, *J* = 1.5, 1H, CH₂), 5.304 (t, *J* = 1.5, 1H,), 3.230 (q, *J* = 6.0, 2H, CH₂), 2.554 (t, *J* = 7.5, 2H, CH₂), 1.840 (s, 3H, CH₃)

Synthesis of poly(dopamine methacrylamide-co-N-isopropylacrylamide-co-acrylamide).

Acrylamide (1.479 g, 20.81 mmol), *N*-isopropylacrylamide (2.355 g, 20.81 mmol), *N*-(3,4-dihydroxyphenethyl) methacrylamide (0.252 g, 1.138 mmol), and azobisisobutyronitrile (0.043 g, 0.263 mmol) were dissolved in a Schlenk flask with 10 mL DMSO and degassed for 2 hours with argon sparging at room temperature. The solution was then placed in an oil bath thermostated to 60°C for 25 minutes, at which point the solution reaches the gel point. The solution was then quenched by cooling to 0 °C and addition of 40 mL air-free H₂O. This mixture was sonicated and stirred vigorously under nitrogen to re-dissolve the gel. In a nitrogen glove box, this solution was then washed thrice with 50 mL of degassed dichloromethane and washed once with 50 mL of chloroform. The resulting aqueous layer was precipitated into 50:50 2-propanol:hexane mixture with vigorous stirring resulting in a white, tough, and sticky solid. The

polymer was collected and dried under reduced pressure overnight with an isolatable yield of 82%. The weight average molecular weight (M_w) was determined to be 904 kg/mol by dynamic light scattering (DLS) as shown in ESI Figure S2.

It is important to note that the catechol moiety is not stable in oxygen-rich aqueous media for storage and will slowly oxidize to the quinone via irreversible cross-links over several days (ESI Figure S8). For this reason, all polymer solutions were prepared using air-free H₂O prior to all analysis and gels were allowed to cure for only 10 minutes prior to mechanical analysis. The iron (III) chloride solution was prepared fresh daily to reduce the formation of insoluble iron hydroxides.

Characterization Disclaimer

Certain commercial equipment, instruments, or materials are identified in this paper in order to specify the experimental procedure adequately. Such identification is not intended to imply recommendation or endorsement by the National Institute of Standards and Technology, nor is it intended to imply that the materials or equipment identified are necessarily the best available for the purpose. The error bars represent one standard deviation of the data, which is taken as the uncertainty of the measurement.

UV-vis spectroscopy was performed on a Cary 50 spectrophotometer (Varian). The weight-average molecular weight of the copolymer was estimated using dynamic light scattering (Malvern Zetasizer Nano). FTIR measurements were taken with a Nicolet Model 6700 with a grazing angle attenuated total reflectance accessory (GATR) at 64 scans with a 4 cm⁻¹ resolution. Tensile testing was performed on an Instron tensile tester. A bench top compact UV lamp

equipped with a 254 nm wavelength source (4-watt, 152.4 mm) was used as the UV light source. The substrates were held 2 cm from the source for hydrogels prepared as films and 6 cm for UV-vis and titration experiments and irradiated at a power of 1.20 and 0.22 mW cm⁻² respectively.

Rheological measurements were performed on a TA Instruments ARES-G2 strain-controlled rheometer with 50-mm 0.04-rad cone upper (0.05 mm truncation gap) and Peltier plate lower geometry. A solvent trap was used to prevent evaporation. Reported strain sweeps were acquired at 22 °C and 10 rad/s. From the strain sweeps the linear region was determined to end ~10 % strain for pre-UV samples and ~100 % strain for post-UV samples. Reported frequency sweeps were acquired at 22 °C and 10 % or 100 % strain for pre-UV and post-UV samples, respectively.

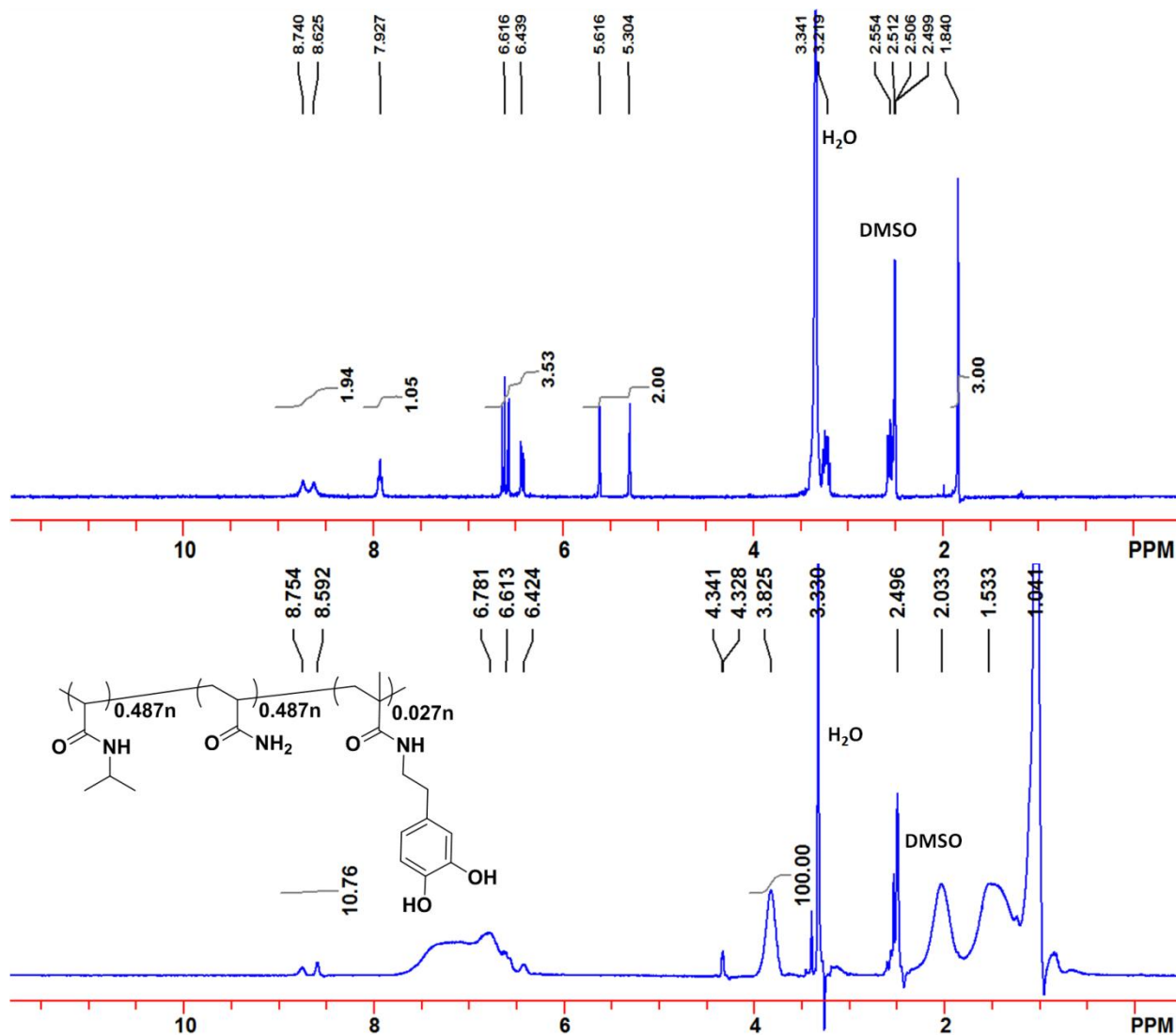


Figure C.1. Catechol preservation in pDMA determined by ^1H NMR. Spectra of DMA monomer (top) and p(DMA-co-NIPAM-co-AcAm) copolymer (bottom). Presence of two phenolic peaks at 8.760 and 8.598 ppm in the polymer demonstrates preservation of catechol pendant group. Integration of pNIPAM isopropyl peak (1H) at 3.825 ppm relative to the catechol peaks (2H) at 8.754 and 8.592 ppm show at least 97% catechol preservation.

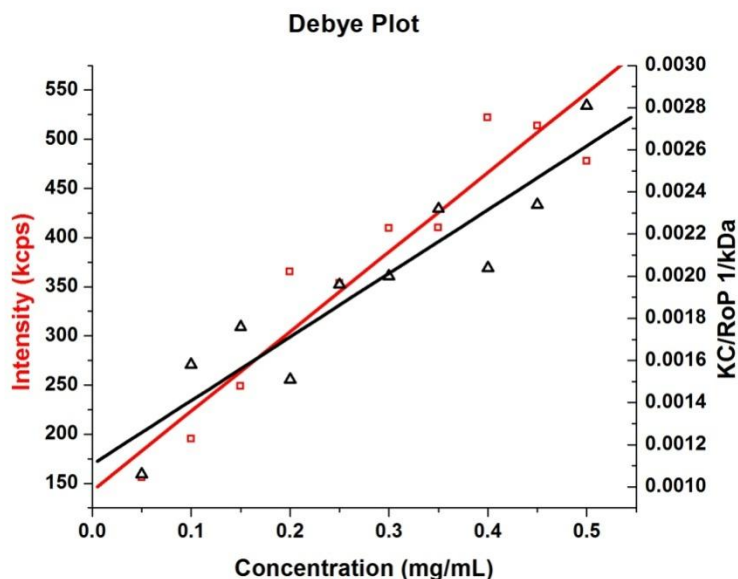


Figure C.2. Dynamic light scattering Debye plot for molecular weight determination. In lieu of aqueous phase GPC, we used light scattering to indirectly measure molecular weight based on the polymer's hydrodynamic radius in pure, air-free water. The molecular weight was determined to be 904 kDa and the hydrodynamic radius was determined to be 30.90 nm.

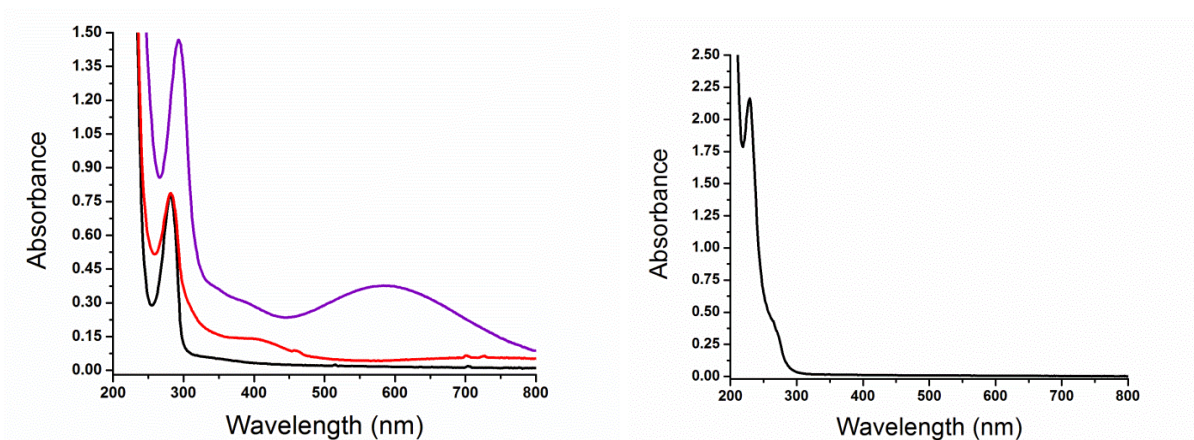


Figure C.3. UV-vis absorbance spectra for p(DMA-co-NIPAM-co-AcAm) in H₂O. Left: UV-vis absorbance spectra for native p(DMA-co-NIPAM-co-AcAm) in H₂O (black), the mono-complexed iron-catechol polymer (red), and fully titrated bis-complexed iron-catechol polymer (purple). Right: UV-vis spectrum of diphenyliodonium chloride at 0.331 mM in H₂O. The UV

absorbance of the native polymer and polymer-iron complexes show a relative minimum centered near 250 nm while the spectrum of the photoacid generator shows a higher absorbance at 250 nm.

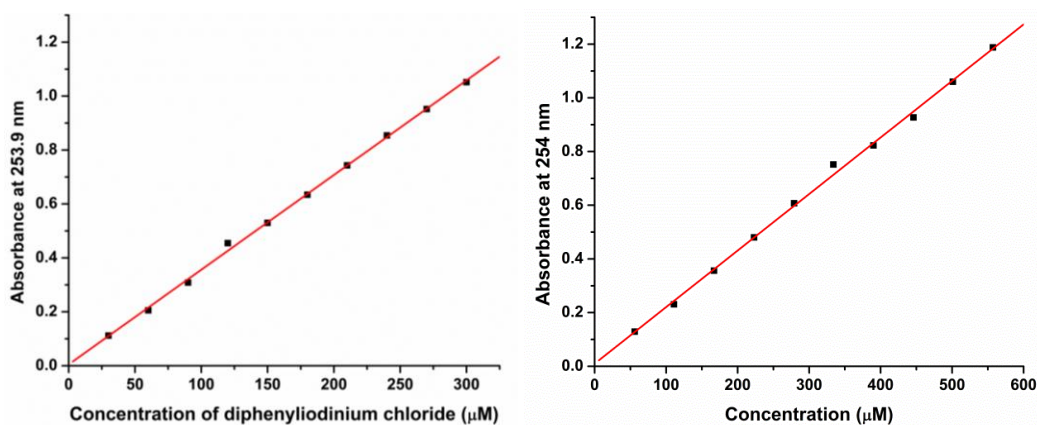


Figure C.4. Extinction coefficients for diphenyliodonium chloride and the bis-complex. Monitored at 253.9 nm, the molar extinction coefficient of diphenyliodonium chloride and the bis-complex were determined to be $5160 \text{ M}^{-1}\text{cm}^{-1}$ and $2110 \text{ M}^{-1}\text{cm}^{-1}$ respectively.

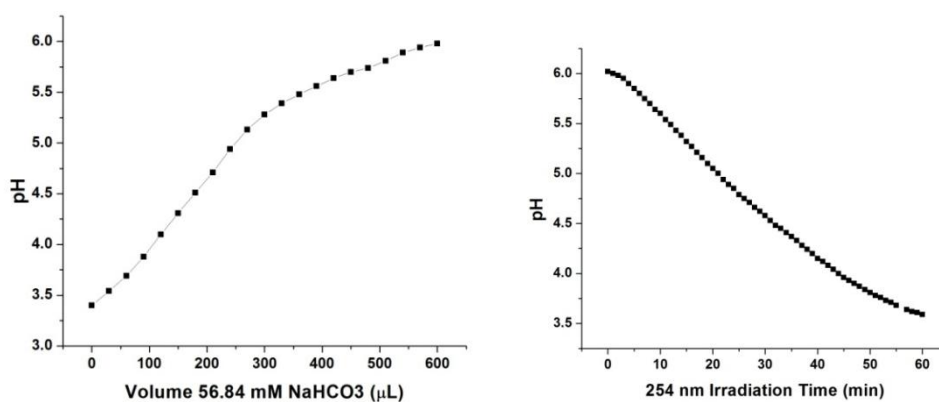


Figure C.5. NaHCO_3 titration plot of p(DMA-co-NIPAM-co-AcAm). A solution of p(DMA-co-NIPAM-co-AcAm) at 0.56 mM DMA content, 2 mg mL^{-1} , is shown left, and subsequent phototitration with 254 nm UV light at 0.22 mW cm^{-2} is shown right. An equivalence point is observed at pH 4.5 (1.5 EQ of base added) according to the basic titration.

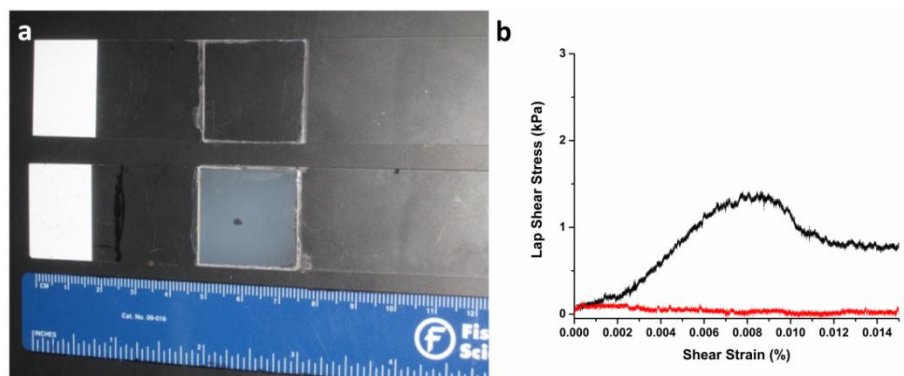


Figure C.6. Lap-Shear analysis before and after irradiation. a) Comparison of gels prepared for Lap-Shear analysis before irradiation with 254 nm light (top) and after irradiation (bottom) for 60 seconds and b) example stress-strain curve of gels before UV exposure (black) and after UV exposure (red).

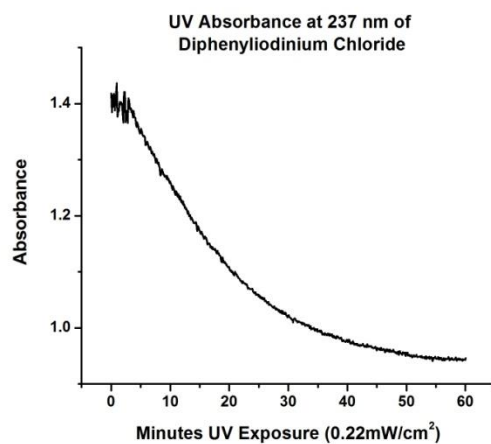


Figure C.7. Kinetic plot of UV-induced conversion of diphenyliodonium chloride. A 0.331 mM aqueous solution of diphenyliodonium chloride was irradiated with 0.22 mW cm⁻² of 254 nm light and monitored at 237 nm. The reaction is completed after approximately 60 min UV exposure.

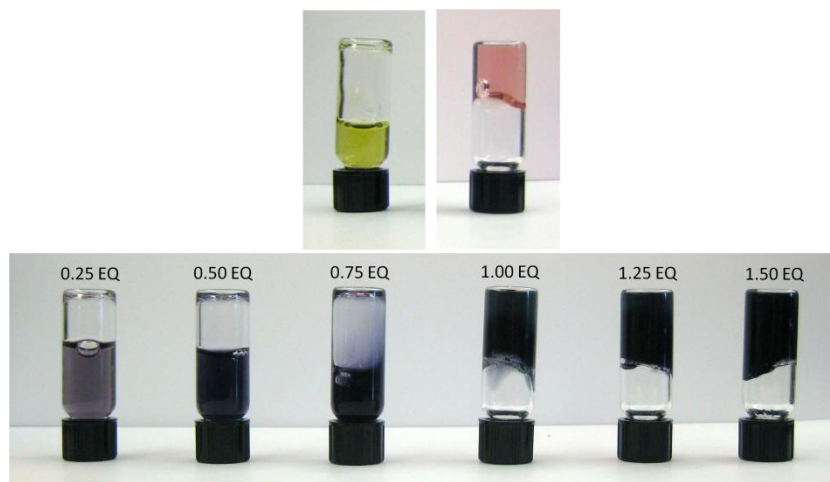


Figure C.8. Varying the Fe^{3+} concentration relative to catechol. Top: Photographs of a 1.9 wt. % prepolymer solution of mono-complexed p(DMA-co-NIPAM-co-AcAm) before titration (left), and a 2.0 wt. % hydrogel after 24 days areal oxidation (right). Bottom: Varying the Fe^{3+} concentration relative to catechol from 0.25:3 to 1.50:3.

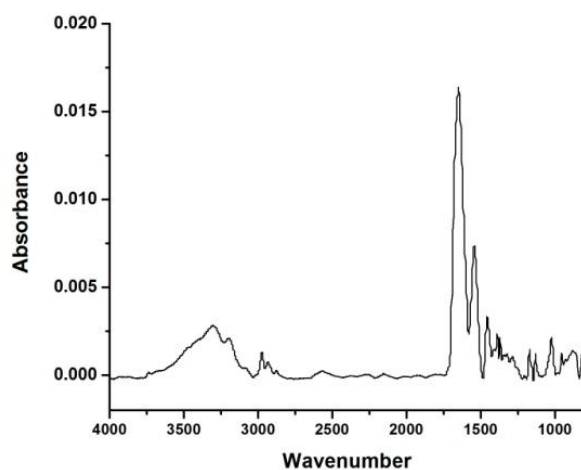


Figure C.9. GATR-FTIR of dry native p(DMA-co-NIPAM-co-AcAm).

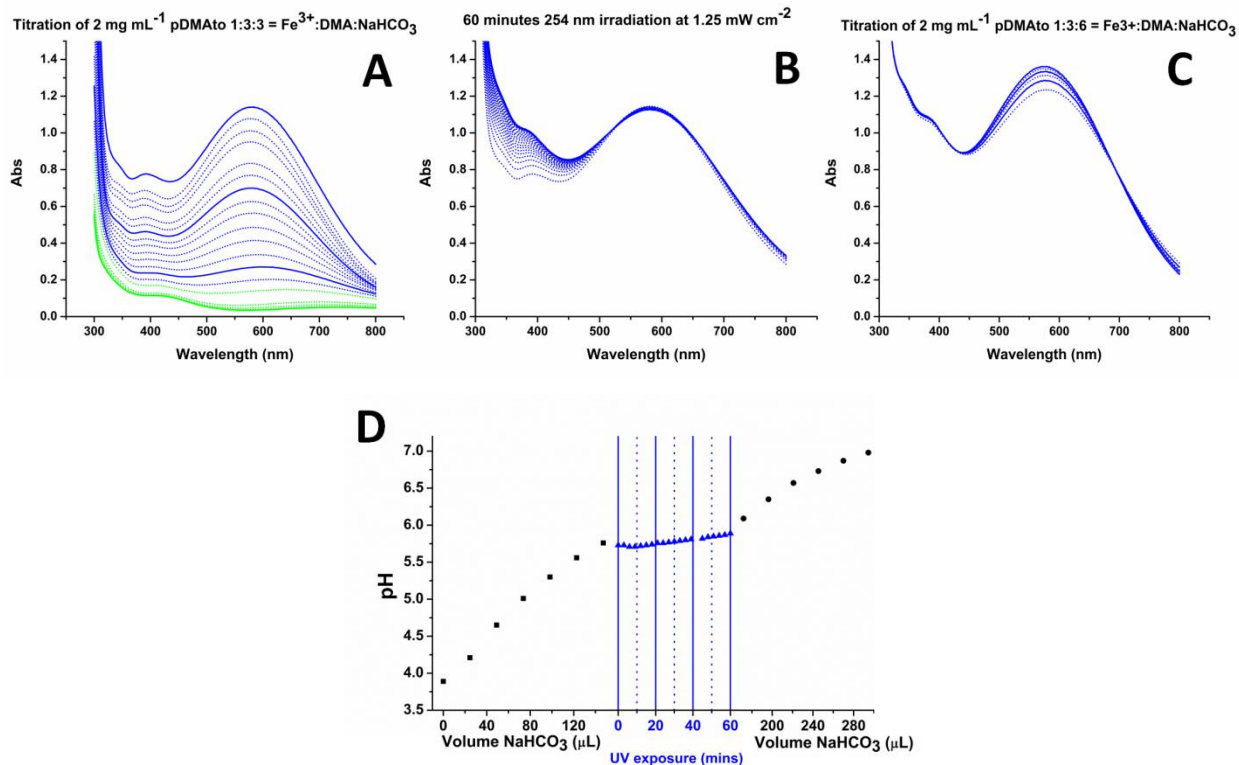


Figure C.10. Control study on a 2 mg mL⁻¹ solution of p(DMA-co-NIPAM-co-AcAm). **A.** The monocomplex (solid green line, pH = 3.89), is titrated with 1 to 3 equivalents of NaHCO₃ (solid blue lines, pH = 4.65 - 5.76). **B.** Irradiation of the sample with 254 nm light for 60 minutes, during which time the pH fluctuations are small, pH = 5.63 - 5.79 over 60 minutes. **C.** Continuation of titration of the sample with 4-6 equivalents of NaHCO₃ (solid blue lines, pH = 5.79 - 6.98). **D.** Corresponding titration data for control study.

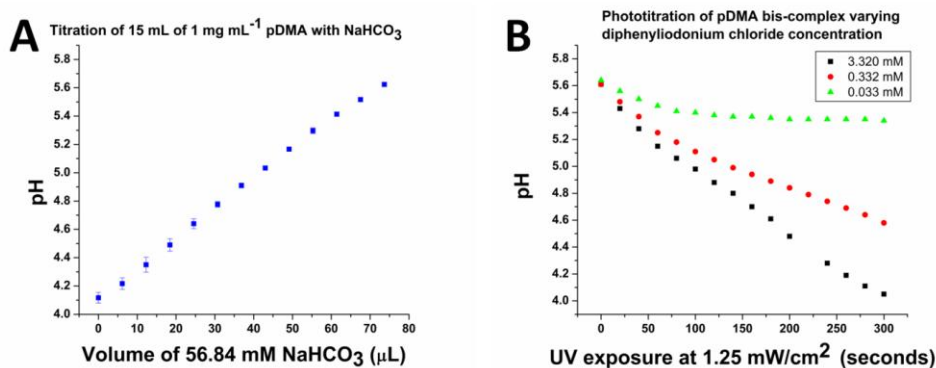


Figure C.11. **A.** Titrations for pDMA gels varying PAG content. The solution is first titrated with 3 equivalents of NaHCO₃ (pH 3.89 - 5.60); error bars represent one standard deviation from

the average. **B.** The polymer was prepared at 1 mg/mL concentrations with 3.32 mM, 0.332 mM, and 0.033 mM diphenyliodonium chloride (35.7EQ, 3.57 EQ and 0.36 EQ respectively) for UV exposure studies.

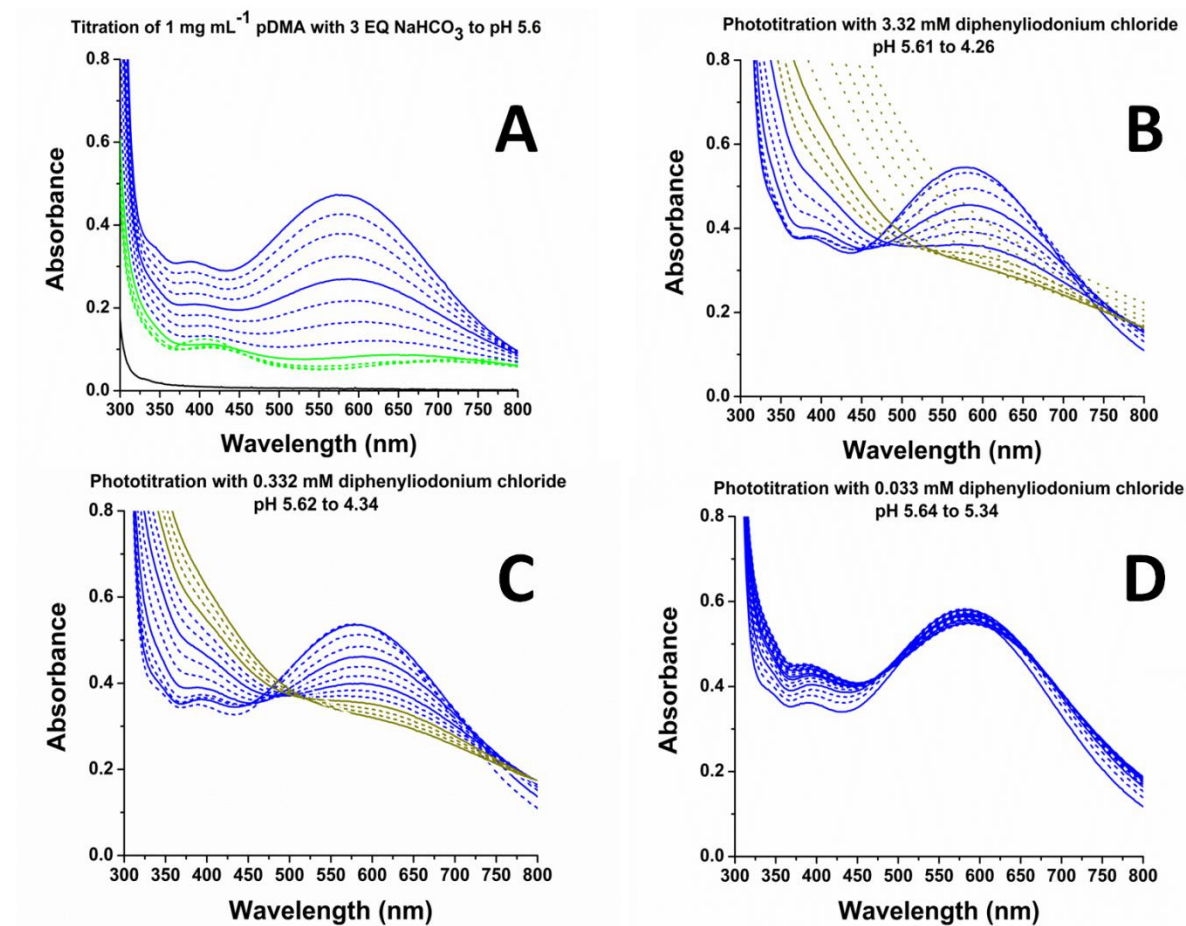


Figure C.12 *In situ* UV-vis titration of pDMA gels varying PAG content. **A.** Titration of p(DMA-co-NIPAM-co-AcAm) to pH 5.6 with the addition of 3 equivalents of NaHCO₃. **B. – D.** Corresponding UV-vis spectra for Figure S11.B. UV exposures at varying concentrations of photoacid generator.

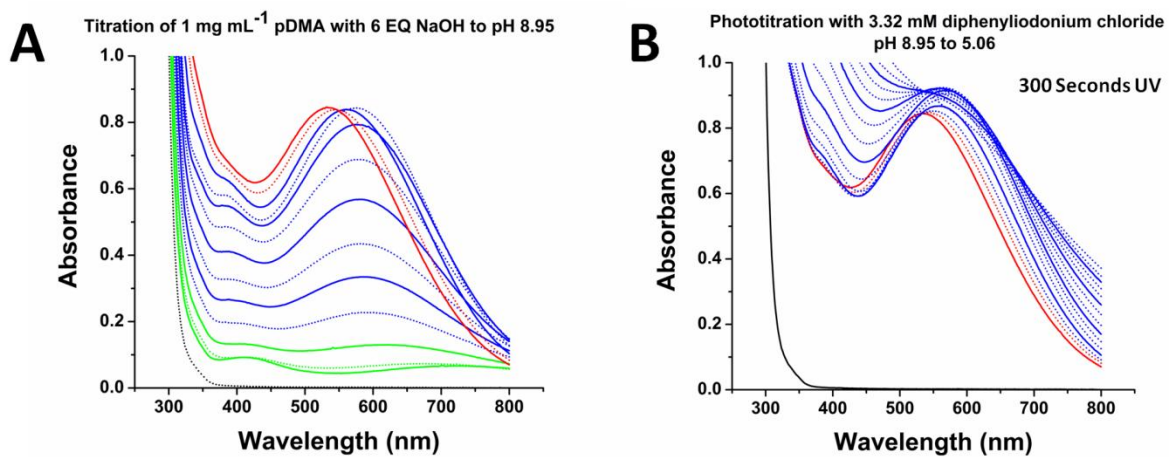


Figure C.13. Titration of p(DMA-co-NIPAM-co-AcAm) with excess base. **A.** Titration of p(DMA-co-NIPAM-co-AcAm) to pH 8.95 with the addition of 6 equivalents of NaHCO₃. **B.** Corresponding UV-vis spectra for UV exposure for 300 seconds at 20 second intervals.